Advances in GEOPHYSICS

VOLUME 58

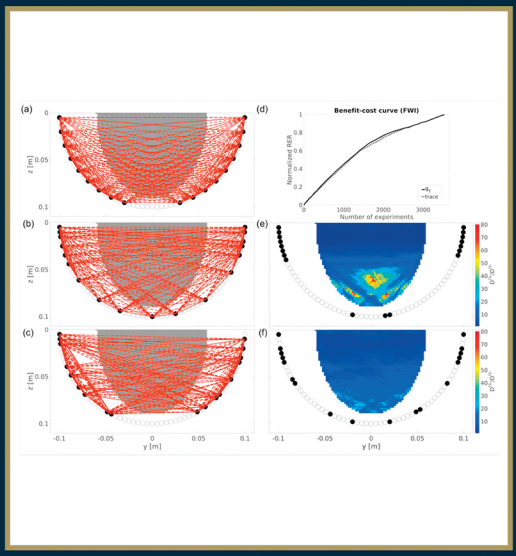

VOLUME FIFTY EIGHT

ADVANCES IN
GEOPHYSICS

This page intentionally left blank

VOLUME FIFTY EIGHT

ADVANCES IN GEOPHYSICS

Series Editor

LARS NIELSEN
Department of Geosciences and Natural Resource Management, University of Copenhagen, Copenhagen, Denmark

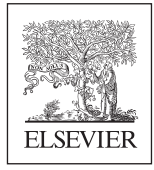

ACADEMIC PRESS
An imprint of Elsevier

Academic Press is an imprint of Elsevier
50 Hampshire Street, 5th Floor, Cambridge, MA 02139, United States
525 B Street, Suite 1800, San Diego, CA 92101–4495, United States
The Boulevard, Langford Lane, Kidlington, Oxford OX5 1GB, United Kingdom
125 London Wall, London, EC2Y 5AS, United Kingdom

First edition 2017

Notices
Knowledge and best practice in this field are constantly changing. As new research and experience broaden our understanding, changes in research methods, professional practices, or medical treatment may become necessary.

Practitioners and researchers must always rely on their own experience and knowledge in evaluating and using any information, methods, compounds, or experiments described herein. In using such information or methods they should be mindful of their own safety and the safety of others, including parties for whom they have a professional responsibility.

To the fullest extent of the law, neither the Publisher nor the authors, contributors, or editors, assume any liability for any injury and/or damage to persons or property as a matter of products liability, negligence or otherwise, or from any use or operation of any methods, products, instructions, or ideas contained in the material herein.

ISBN: 978-0-12-812413-0
ISSN: 0065-2687

Publisher: Zoe Kruze
Acquisition Editor: Jason Mitchell
Editorial Project Manager: Joanna Collett
Production Project Manager: Vignesh Tamil
Cover Designer: Greg Harris

Typeset by SPi Global, India

CONTENTS

This page intentionally left blank

CONTRIBUTORS

Esben Auken
Department of Geoscience, Aarhus University, Aarhus, Denmark

Christian Boehm
Institute of Geophysics, ETH Zurich, Zurich, Switzerland

Tue Boesen
Department of Geoscience, Aarhus University, Aarhus, Denmark

Anders V. Christiansen
Department of Geoscience, Aarhus University, Aarhus, Denmark

Andreas Fichtner
Institute of Geophysics, ETH Zurich, Zurich, Switzerland

Edgar Manukyan
Institute of Geophysics, ETH Zurich, Zurich, Switzerland

Naiara Korta Martiartu
Institute of Geophysics, ETH Zurich, Zurich, Switzerland

Hansruedi Maurer
Institute of Geophysics, ETH Zurich, Zurich, Switzerland

André Nuber
Institute of Geophysics, ETH Zurich, Zurich, Switzerland

Fabienne Reiser
Institute of Geophysics, ETH Zurich, Zurich, Switzerland

Cédric Schmelzbach
Institute of Geophysics, ETH Zurich, Zurich, Switzerland

This page intentionally left blank

PREFACE

This volume of Advances in Geophysics is dedicated to two reviews, which are both focused on experimental design as well as development and application of data acquisition and modeling/interpretation algorithms.

The first review focuses on optimization of experimental design in relation to seismic full waveform inversion and imaging. This contribution is by Maurer, Nuber, Martiartu, Reiser, Boehm, Manukyan, Schmelzbach, and Fichtner. For several decades much geophysical research has been focused on retrieving as much information as possible from seismic data, which arguably constitute the most important geophysical source of information about the distribution of geological structures and features in the subsurface. Thus, much effort has been (and is, of course, still) directed toward development of new data acquisition strategies and new methods for optimized subsurface imaging based on the acquired seismic data (numerous references in the chapter by Maurer et al.). In more recent years, development and application of full waveform inversion methods have shown that such techniques may provide improved information of subsurface rock physics parameters at high resolution. Computational power now has reached a sufficiently high level, so that it is now also possible to apply such methods in practice in some cases. In this volume of Advances in Geophysics, Maurer et al. focus on the importance of designing optimal source-receiver geometries for use in full waveform inversion studies. Maurer et al. base their findings on widely different examples and give directions for how optimal source-receiver distributions may be identified/chosen.

The second review, which is authored by Auken, Boesen, and Christiansen, has its focus on developments of airborne electromagnetic methods. In recent years, the geophysical community has experienced much new development in electromagnetic methods, and, in particular, airborne approaches to data acquisition have been subject to many new applications. The increasing demands for, for example, groundwater mapping and exploration and the search for mineral resources have been among the factors that have triggered the recent advances and developments. These factors have in turn triggered development of new instrumentation, strategies for data collection as well as optimized and improved processing and interpretation tools (see references and discussion in the chapter by Auken et al.). Here, in volume 58 of Advances in Geophysics, Auken et al. outline the most

central developments in airborne electromagnetic methods during the past 10 years (from 2007 to 2017) with focus on groundwater and geotechnical applications. They describe the recent developments related to instrument production and design, new applications and they outline major advances related to data processing and interpretation that have gone hand-in-hand with the technological advances and new applications.

Enjoy your reading of volume 58 of Advances in Geophysics!

Lars Nielsen, Editor

CHAPTER ONE

Optimized Experimental Design in the Context of Seismic Full Waveform Inversion and Seismic Waveform Imaging

Hansruedi Maurer[1], André Nuber, Naiara Korta Martiartu, Fabienne Reiser, Christian Boehm, Edgar Manukyan, Cédric Schmelzbach, Andreas Fichtner

Institute of Geophysics, ETH Zurich, Zurich, Switzerland
[1]Corresponding author: e-mail address: hansruedi.maurer@erdw.ethz.ch

Contents

Abstract

During the past few years, significant improvements have been achieved in high-resolution imaging with seismic data. In particular, seismic full waveform inversion (FWI) has been proven to be a very promising tool. However, this technique requires high-quality data, whose acquisition can be very expensive. Furthermore, FWI is

Advances in Geophysics, Volume 58
ISSN 0065-2687
https://doi.org/10.1016/bs.agph.2017.10.001

computationally extremely demanding, which currently limits its application to large-scale data sets. Both problems can be alleviated with optimized experimental design (OED) techniques. Using tools from the linearized inversion theory, we outline how source–receiver patterns can be identified that are most suitable for FWI experiments. This is demonstrated by reviewing a laboratory-scale experiment devoted to breast cancer detection with ultrasound data, and with a surface seismic survey study that is concerned with elastic FWI for shallow subsurface structures. By means of a vertical seismic profiling design example, we also show that the OED technology can be adapted to wavefield imaging techniques. Besides identifying optimized source–receiver patterns, OED can be employed for extracting the most useful attributes from a seismic data set, which can reduce the computational costs. For that purpose, we discuss a frequency-domain crosshole FWI experiment, where we quantify the information content of different data representations and identify suitable spatial and temporal sampling strategies. In a second crosshole study, it is inspected that source and receiver components allow the relevant elastic subsurface properties to be resolved. Finally, we outline a more general framework of seismic observables, with which the sensitivity of selected model parameters can be maximized. This is demonstrated with an example of regional earth mantle tomography.

1. INTRODUCTION

The main task of any (geo)physical method is to extract information from measured data on either material properties or physical processes. Evidently, it is therefore essential that the corresponding experiment is designed, such that as much information as possible can be retrieved. Experimental design is typically governed by experiences from the past and the theoretical relationship between data and model parameters. There are numerous evidences that indicate that the former often prevails. A nongeophysical, but revealing, example includes the design of keyboard layouts. They were originally designed for mechanical typewriters, where it had to be made sure that potential tangling of the typing arms was minimized. This resulted in keyboard layouts, where the most often used characters were located at rather inconvenient positions. Although the problem of typing arms tangling is no longer an issue with modern computers, the use of the original layouts has continued.

A more geophysical example includes geoelectrical survey configurations. Most of the actual geoelectrical surveys include either dipole–dipole, Wenner, or Schlumberger configurations (e.g., Reynolds, 2011). These configurations were originally invented to ease the data acquisition with four-electrode systems (two electrodes for current injections and two

electrodes for measuring the resulting potential difference). Modern multi-electrode systems allow measurements with arbitrary electrode configurations that might be much more suitable in terms of information content, but the traditional electrode configurations continue to be used predominantly.

There are undoubtedly valid reasons for continuing the usage of traditional technology (e.g., using well-established keyboard layouts), but for the design of (geo)physical experiments, this may be very inefficient and uneconomical. This has been recognized by several researchers and has led to the concept of optimized experimental design (OED). Here, the experimental design process is formulated as an optimization problem, where the information content offered by a particular data set is maximized.

An obvious option for maximizing the data information content is to acquire as much data as possible. This may not only result in substantial experimental costs but may also introduce considerable redundancies. While the latter is sometimes a desired feature for minimizing the effects of noise, the costs associated with such an extensive surveying approach usually preclude this strategy to be chosen. Therefore, the experimental design process must be reformulated, such that the benefit–cost ratio is maximized.

This raises the question on how to define *benefit* and *cost*. It is a relatively trivial matter to specify a quantitative measure of cost. Typically, it is proportional to the amount of data to be acquired, but it is also possible to include costs in terms of a monetary value for renting equipment, for hiring a field crew, and for other expenses associated with an experiment. A suitable quantification of benefit is more complicated. This is very much dependent on the survey objectives. For example, is it anticipated to obtain a complete subsurface image, or is it sufficient to illuminate only a restricted region of particular interest? As it will be outlined later in more detail, the term benefit is also tightly coupled with the data analysis method, that is, to what extend is a particular method capable to extract information from the data?

Cox (1958) formulated some of the first ideas about experimental design, and Fedorov (1972) was one of the first, who published an experimental design study. The method found quickly applications in the industrial design. In particular, Taguchi (1987) developed a number of techniques that helped improving Japanese industrial processes. This contributed significantly to the success of the Japanese industry toward the end of the last century.

Initially, applications of OED in geophysics were devoted to the design of earthquake observation networks (Hardt & Scherbaum, 1994;

Kijko, 1977; Rabinowitz & Steinberg, 1990). Later, similar techniques were applied to ocean tomography (Barth & Wunsch, 1990) and geoelectrical sounding (Glenn & Ward, 1976). Inspired by the work of Curtis and Snieder (1997) and Maurer and Boerner (1998), OED gained considerable popularity and was applied to geoelectrical tomography problems (e.g., Stummer, Maurer, & Green, 2004; Wilkinson, Meldrum, Chambers, Kuras, & Ogilvy, 2006) and seismic investigations (e.g., Curtis, 1999). A more extensive overview of OED can be found in Maurer, Curtis, and Boerner (2010).

Optimizing the setup of an experiment, as performed with OED, is one option of improving the benefits of a geophysical survey. Alternatively, one may optimize the data analysis method, such that the information content offered by an existing data set is better exploited. For wavefield radiation methods (i.e., seismics and ground-penetrating radar), this has led to the development of full waveform inversion (FWI) techniques. Instead of analyzing only certain portions or attributes of the recordings, such as first breaks for travel time tomography (e.g., Lanz, Maurer, & Green, 1998), reflected phases for seismic imaging (e.g., Yilmaz & Doherty, 2001), or surface waves (e.g., Socco & Strobbia, 2004), FWI attempts to find a subsurface model that is capable to predict the entire wavefield.

Inspired by the pioneering work of Tarantola (1984), Mora (1987), and Pratt (1999), FWI experienced a rapid development during the past 15 years and was applied to a broad scale of problems ranging from mantle tomography (e.g., Fichtner, 2010) to crustal studies (e.g., Dessa et al., 2004), exploration problems (e.g., Virieux & Operto, 2009), shallow seismic and ground-penetrating radar applications (e.g., Butzer, Kurzmann, & Bohlen, 2013; Ernst, Maurer, Green, & Holliger, 2007) to laboratory-scale applications (e.g., Bretaudeau, Brossier, Leparoux, Abraham, & Virieux, 2013).

Compared with more traditional techniques, FWI conceptually offers tremendous improvements, but there are also numerous problems that are still subject of actual research efforts. Examples include the pronounced nonlinearity of FWI that requires a substantial amount of a priori information for constructing suitable initial models, and effects of anisotropy and anelastic attenuation that require a large number of model parameters to be considered. The probably most severe problem is still imposed by the extremely large computational costs associated with realistic FWI problems. Even with the seemingly ever-increasing computer power available, it is still very challenging, or even impossible, to apply the method to larger scale 3D problems.

Combining OED with FWI is expected to be most beneficial, because it will allow both setting up appropriate experiments and fully exploiting the data information content. The literature on this topic is still sparse, but during the past years, several papers have been published that highlight the benefits of combining OED and FWI. The topics discussed can be broadly subdivided into two categories:

1. What is a suitable data acquisition geometry? The deployment of sources of and receivers for FWI is often governed by concepts adopted from reflection seismics or travel time tomography. These choices may be not optimal for FWI experiments.
2. Which data attributes, respectively, which combination of attributes provide most information? Although FWI is designed to consider the entire waveforms, limited data acquisition budgets and/or limited computational resources, the strong nonlinearity of the FWI problem, and noise considerations often require to focus on a limited selection of data attributes (e.g., limited frequency band or only single components of the 3D wavefields).

In this paper we review both aspects. After a brief introduction to the theory of OED and FWI, we present several case studies, where either the data acquisition geometry or the optimal choice of data attributes is discussed. The applications range from small-scale laboratory experiments to large-scale regional FWI studies, thereby indicating not only the versatility of OED and FWI but also the combined application thereof. Although the case studies presented in this contribution originate solely from research groups at ETH Zurich, we would like to emphasize that there are several other workgroups worldwide being active in the field of optimized survey design. We provide a review of all the corresponding literature that we are aware of. However, it should be noted that we focus our discussions on OED applied to FWI and closely related techniques. For a more general review of OED in geophysics, the reader is referred to Maurer et al. (2010). The paper is concluded by discussing alternative options of optimizing FWI experiments and outlining fruitful avenues of future research.

2. THEORY

2.1 Inverse Theory

Although the strong nonlinearity of the FWI problem should be tackled with truly nonlinear inversion algorithms, such as global optimizers (e.g., Sen & Stoffa, 2013), the tremendous computational costs associated with

these algorithms currently preclude their application to realistic problems. Instead, it is common practice to solve a linearized least-squares inversion problem iteratively. This can be written as

$$\mathbf{m}^{i+1} = \mathbf{m}^{i} + \alpha \nabla \mathbf{E}, \tag{1}$$

where $\mathbf{m}$ represents the model parameters and the superscript i the iteration number with $i = 0$ being the initial model that is established from all a priori information available. E denotes the misfit function

$$E = \frac{1}{2} \sum_{k=1}^{k=K} \left(\frac{d_k^{obs} - g_k(\mathbf{m}^i)}{\varepsilon_k} \right)^2, \tag{2}$$

where d^{obs} denote the observed data, ε the data errors, K the number of data points, and $g_k(\mathbf{m}^i)$ is the solution of the (truly nonlinear) forward problem, that is predicting the data using the actual set of model parameters $\mathbf{m}^i$. The gradient $\nabla \mathbf{E}$ can be written as

$$\nabla \mathbf{E} = \frac{\partial E}{\partial \mathbf{m}} = \frac{\partial g_k}{\partial \mathbf{m}_j^i} \frac{d_k^{obs} - g_k(\mathbf{m}^i)}{\varepsilon_k} = -\mathbf{J}^{\mathbf{T}} \Delta d, \tag{3}$$

where the partial derivatives $\partial g_k / \partial \mathbf{m}_j^i$ ($j = 1 \ldots$ number of model parameters) are contained in the Jacobian matrix $\mathbf{J}$ and Δd includes the weighted data residuals $\frac{d_k^{obs} - g_k(\mathbf{m}^i)}{\varepsilon_k}$. The term α in Eq. (1) is either a scaling factor for the steepest descent and conjugate gradient methods, the inverse of the approximate Hessian matrix ($\mathbf{J}^{\mathbf{T}} \mathbf{C}_{\mathbf{D}}^{-1} \mathbf{J}$) ($\mathbf{C_D}$ is the a priori data covariance matrix including ε^2 in its diagonal), when using the Gauss–Newton method, or the inverse of the full Hessian matrix $\mathbf{H} = \frac{\partial^2 E}{\partial (\mathbf{m}^i)^2}$ when using the full Newton method (Pratt, Shin, & Hicks, 1998). For large-scale inversion problems, it is common practice to use the adjoint state method for computing $\nabla \mathbf{E}$, which does not require the partial derivatives $\frac{\partial g}{\partial \mathbf{m}^i}$ to be computed explicitly (e.g., Fichtner, 2010), but in this contribution, we will focus primarily on the Gauss–Newton method, because the information contained in the Jacobian matrix $\mathbf{J}$ will be essential for OED purposes.

Typical geophysical inversion problems do not include sufficient data constraints for finding a unique solution. Therefore, regularization constraints need to be added. This is typically supplied in form of damping and smoothing constraints (e.g., Maurer, Holliger, & Boerner, 1998).

The regularized Gauss–Newton solution (corresponding to Eq. (1)) can be written as

$$\mathbf{m}^{i+1} = \mathbf{m}^{i} + \left(\mathbf{J}^{\mathbf{T}}\mathbf{C}_{\mathbf{D}}^{-1}\mathbf{J} + w_d^2\mathbf{I} + w_s^2\mathbf{L}\right)^{-1}\mathbf{J}^{\mathbf{T}}\mathbf{C}_{\mathbf{D}}^{-1}\boldsymbol{\Delta}\mathbf{d}, \tag{4}$$

where w_d and w_s define the contributions of damping and smoothing, respectively, $\mathbf{I}$ is the identity, and $\mathbf{L}$ is a smoothing matrix.

2.2 Optimized Experimental Design

OED, often also referred as statistical experimental design, can be considered as the optimization of an inversion problem. Eqs. (1)–(4) indicate that the inverse problem estimates an optimal set of model parameters using data constraints. In contrast, OED seeks an optimized experimental layout (i.e., data set) that constrains the model parameter in an optimal fashion.

As already outlined in Section 1, an optimized experimental layout has a favorable benefit/cost ratio. In the context of FWI, costs can be a measure of the number of sources and/or receivers involved, the number of frequencies considered, or the portions of the seismograms to be analyzed. A measure of benefit can be derived from quantities associated with the corresponding inversion problem to be solved. An extensive discussion on possible measures can be found in Curtis (1999). Here, we focus primarily on the eigenvalue spectrum of the approximate Hessian matrix $(\mathbf{J}^{\mathbf{T}}\mathbf{C}_{\mathbf{D}}^{-1}\mathbf{J})$. As indicated in Eq. (4), the solution of the inverse problem involves the computation of $(\mathbf{J}^{\mathbf{T}}\mathbf{C}_{\mathbf{D}}^{-1}\mathbf{J} + w_d^2\mathbf{I} + w_s^2\mathbf{L})^{-1}$. The data constraints are included in $(\mathbf{J}^{\mathbf{T}}\mathbf{C}_{\mathbf{D}}^{-1}\mathbf{J})$, and the regularization term $(w_d^2\mathbf{I} + w_s^2\mathbf{L})$ is only required to make the matrix $(\mathbf{J}^{\mathbf{T}}\mathbf{C}_{\mathbf{D}}^{-1}\mathbf{J} + w_d^2\mathbf{I} + w_s^2\mathbf{L})$ invertible. Ideally, our ability to invert this matrix should be governed by data and not by regularization constraints. Therefore, we seek an experimental setup that leads to an approximate Hessian $(\mathbf{J}^{\mathbf{T}}\mathbf{C}_{\mathbf{D}}^{-1}\mathbf{J})$ that is well invertible, and the effects of regularization can be minimized. This can be quantified by the eigenvalue spectrum of $(\mathbf{J}^{\mathbf{T}}\mathbf{C}_{\mathbf{D}}^{-1}\mathbf{J})$ as shown in Fig. 1. If all eigenvalues would be nonzero, the approximate Hessian could be inverted without any regularization constraints. Unfortunately, this is rarely the case. Furthermore, very small eigenvalues indicate that the inverse problem is potentially ill-conditioned, and may lead to unreliable results, particularly in the presence of noise. Therefore, it is useful to define a threshold value for the eigenvalues, below which they must be considered to be insignificant. This threshold value is typically of the order of

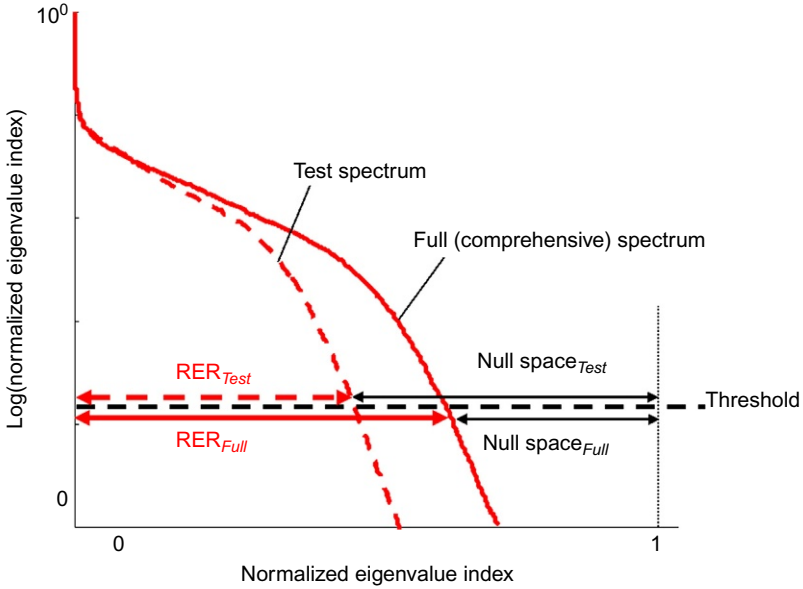

Fig. 1 Normalized eigenvalue for a comprehensive data set (*solid red line*) and a test data set (*dashed red line*). The corresponding RER values are indicated with *solid* and *dashed red double arrows*.

10^{-8}–10^{-12} of the largest eigenvalue. As indicated in Fig. 1, the intersection of an eigenvalue spectrum with such a threshold line specifies the size of the resolved model space and the unresolved model space (Null space). Maurer, Greenhalgh, and Latzel (2009) specified the intersection point as the relative eigenvalue range (RER).

The goal of OED is to find an experimental layout that maximizes the resolved model space, respectively, minimizes the Null space. First, the size of the Null space (i.e., the RER) needs to be determined, supposed that all feasible experimental configurations would have been considered. Such a data set is subsequently referred as a *comprehensive data set* $\boldsymbol{\Omega}_M$. Once the RER of $\boldsymbol{\Omega}_M$ is available, subsets thereof can be computed, subsequently referred as test data sets $\boldsymbol{\Omega}_T$, whereby the RER values of $\boldsymbol{\Omega}_T$ should be as close as possible to those of $\boldsymbol{\Omega}_M$. Nuber, Maurer, and Manukyan (2017) introduced the term *normalized RER* (nRER), which represents the RER ratio of a test data set $\boldsymbol{\Omega}_T$ and the comprehensive data set $\boldsymbol{\Omega}_M$:

$$\mathrm{nRER} = \frac{\mathrm{RER}^{\boldsymbol{\Omega}_T}}{\mathrm{RER}^{\boldsymbol{\Omega}_M}} \quad (0 < \mathrm{nRER} < 1). \tag{5}$$

Computing the nRER values for a large number of test data sets can be computationally expensive, particularly, when a large number of model parameters are involved. Therefore, it may be necessary to consider an approximate measure of nRER. The diagonal elements of $\mathbf{J^T J}$ include the squared column sums of $\mathbf{J}$. Meles, Greenhalgh, Green, Maurer, and Van der Kruk (2012) showed that the (absolute) column sums of $\mathbf{J}$ are a good proxy for the diagonal elements of the model resolution matrix (e.g., Menke, 2012), which is also a measure of the goodness of a particular survey layout. Therefore, we can define a new measure g_T that offers similar information as the nRER, but is much cheaper to compute

$$g_T = \sum_{i=1}^{N} \frac{D_i^{\Omega_M}}{D_i^{\Omega_T} + \delta} \tag{6}$$

with $D^{\Omega_{M,T}} = \mathrm{diag}(\mathbf{J^T J})$ and N is the data set size. The parameter δ is a small positive number that stabilizes the procedure in the presence of very small $D_i^{\Omega_T}$ values.

OED can now be performed by simultaneously maximizing nRER (or minimizing g_T) and minimizing experimental costs. There are conceptually two different strategies possible. The first strategy, subsequently referred as *global experimental design (GOED)*, either tries to maximize the nRER using a prescribed test data set size or solves an optimization problem of the form

$$\max\left\{\mathrm{nRER}\cdot\beta^{-\gamma N}\right\} \text{resp. } \min\left\{g_T\cdot\beta^{\gamma N}\right\}, \tag{7}$$

where β and γ are suitably chosen constants ($\beta > 1$). Such problems can be solved with global optimizers, such as genetic algorithms (e.g., Maurer & Boerner, 1998) or simulated annealing (e.g., Hardt & Scherbaum, 1994). The problem associated with GOED is that it reaches quickly computational limitations for larger scale problems, even when the approximate measure g_T in Eq. (6) is considered. Furthermore, the prescribed test data set size, respectively, the choice of β and γ introduces a subjectivity to the problem, because it is unclear which amount of data offers the best benefit/cost ratio (unless the test data set size is dictated by instrumental constraints).

These problems can be addressed with *sequential experimental design* (SOED). Here, the initial test data set $\boldsymbol{\Omega}_T$ is very small and may include only a single data point. Subsequently, additional data points are added, such that the resulting nRER or g_T values are optimized. Fig. 2 shows the development of the benefit as a function of cost. During the early stages of the sequential design process, the benefit is increasing rapidly, but with the

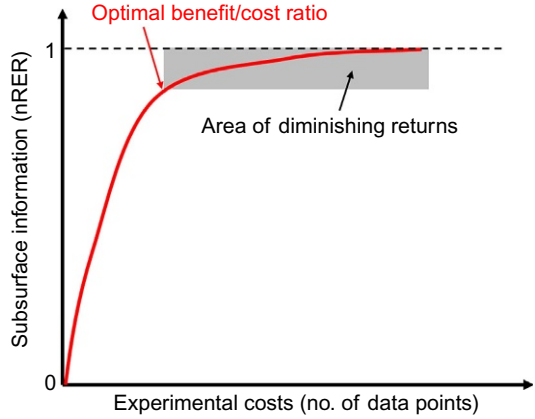

Fig. 2 Concept of sequential experimental design.

increase of data points the benefit–cost curve flattens out (area of diminishing returns), before it reaches the maximum benefit that can be obtained with the comprehensive data set $\boldsymbol{\Omega}_M$. It is now up to the analyst to decide which benefit level is required or desired for reaching the survey objectives. Ideally, one would choose a data set near where the benefit–cost curves attain maximum curvature, that is, where it enters into the area of diminishing returns.

An alternative strategy of SOED is to start with the comprehensive data set $\boldsymbol{\Omega}_M$. Subsequently, those data points that contribute least to the benefit are removed. Although such an approach is computationally more expensive, it can offer interesting insights on the properties of an experimental layout.

The possibility of choosing a data set size on the basis of the benefit–cost curve is a compelling advantage of SOED compared with GOED. A potential disadvantage is some loss of flexibility concerning the combination of data points—once a data point has been selected, it cannot be removed anymore.

A seemingly critical aspect of OED is the choice of the model parameter values, with which the Jacobian matrix $\mathbf{J}$, required for computing potential benefits, is computed. Due to the nonlinearity of FWI (and most other geophysical inversion problems), $\mathbf{J}$ is strongly model dependent. Ideally, one would perform OED on the basis of the true model parameters $\mathbf{m}^{true}$, but this is obviously not possible for realistic problems. Therefore, one needs to perform the design process on the basis of the initial model $\mathbf{m}^0$, which includes all a priori information. It is also possible to repeat OED with a variety of likely model scenarios. Although FWI is a strongly nonlinear problem,

OED is surprisingly insensitive against incorrect design models, even when $\mathbf{m}^0$ mimics $\mathbf{m}^{true}$ only approximately. This has been demonstrated by Nuber et al. (2017). Similar conclusions were drawn by Stummer et al. (2004), who studied geoelectrical tomography problems that are also known to be strongly nonlinear.

2.3 Full Waveform Inversion

There are excellent text books on the theoretical basis of FWI (e.g., Fichtner, 2010; Tarantola, 2005), and a good overview of actual techniques and problems can be found in Virieux and Operto (2009). Therefore, only a very brief overview is presented here. We consider only discrete problems, where the subsurface is parameterized in the form of a stack of layers (1D), cells (2D), or blocks (3D) with piecewise constant material properties. Depending on the problem to be solved, this may include P-wave velocity V_p and density ρ for acoustic problems, additionally the S-wave velocity V_s for elastic problems, plus more material properties that characterize attenuation and/or anisotropy.

The forward problem involves the solution of a set of partial differential equations. Nihei et al. (2012) include a good overview on the current state of the art. In brief, regional and global FWI problems predominantly employ spectral element techniques, whereas exploration-scale problems are mostly tackled with a finite difference algorithm. Most algorithms consider time-domain solvers, but frequency-domain algorithms can be employed as well (e.g., Pratt, 1999).

The inverse problem can be solved in either the time domain (e.g., Tarantola, 1984) or the frequency domain (e.g., Pratt, 1999). To date, both options have a similar popularity. Frequency-domain methods allow the selection of only a few frequencies, which can reduce the amount of data points considerably without substantial information losses, but they have limitations with regard to time windowing (i.e., when only selected portions of the seismograms should be analyzed). Time-domain inversion schemes offer more flexibility for preprocessing the data (e.g., time windowing), but they may be more prone to nonlinear effects, because all frequencies are contained in time-domain data.

The sensitivities contained in Jacobian matrix $\mathbf{J}$ can be computed either with the adjoint state method (e.g., Fichtner, 2010) or using explicit expressions, as introduced by Zhou and Greenhalgh (2009). As outlined in Section 2.1, conjugate gradient, Gauss–Newton, or full Newton methods

can be employed for solving the linearized inversion problems. Most studies published so far use either conjugate gradients or Gauss–Newton algorithms.

3. OPTIMIZATION OF FWI AND WAVEFORM IMAGING EXPERIMENTS

A survey design is a critical task for any seismic campaign. Principles for designing seismic reflection surveys are provided in the textbook of Vermeer (2002) and concepts to formulate this task as an optimization problem were discussed in Liner, Underwood, and Gobeli (1999), Vermeer (2003), Gibson and Tzimeas (2002), and Guest and Curtis (2011).

Fundamental contributions to OED applied to seismic surveying were made by several authors. A good introduction to the topic can be found in Curtis (2004). Haber, Horesh, and Tenorio (2008) provided a general framework for experimental design studies of large-scale regularized inversion problems. Khodja, Prange, and Djikpesse (2010) embedded OED in a Bayesian framework, and Djikpesse, Khodja, Prange, Duchenne, and Menkiti (2012) demonstrated how this technology can be applied to FWI. Applications to vertical seismic profiling (VSP) surveys are reported in Coles and Prange (2012) and Coles, Yang, Djikpesse, Prange, and Osypov (2013). Ajo-Franklin (2009) published an application of OED to time-lapse travel time tomography. Finally, Coles, Prange, and Djikpesse (2015) outline a methodology of how OED can be applied to very large surveys.

In the following, we illustrate aspects of OED applied to FWI and waveform imaging using a selection of studies that the author team has conducted during the past few years. These examples are by no means exhaustive, but they highlight the versatility of OED.

3.1 Travel Time and Acoustic FWI Applied to Medical Tomography

In recent years, FWI has attracted much interest from emerging domains outside of geophysics. In particular, this includes medical imaging for breast cancer detection using ultrasound computed tomography (USCT). In most USCT scanning systems, the patient submerges the breast into a water tank. The sidewalls of the water tank are equipped with ultrasound transducers that can act as sources and receivers, and emit or record ultrasonic waves propagating through the water tank and the human breast. Different prototypes are currently being developed (Ruiter, Göbel, Berger, Zapf, & Gemmeke, 2011; Ruiter et al., 2012; Sandhu, Li, Roy, Schmidt, & Duric, 2015;

Wiskin et al., 2013) and tested in clinical studies (Duric et al., 2014; Huang et al., 2015; Zografos et al., 2013). These studies show the great potential of FWI for breast cancer detection. However, developing a cost-effective and accurate USCT system remains challenging. Thus, there is a great potential for applying techniques from the optimal experimental design.

Despite the vastly different scale, the design of a USCT scanning device shares remarkable similarities with geophysical surveys. The propagation of ultrasonic waves through water and human tissue can be modeled by the (visco)acoustic wave equation, and the number of propagated wavelengths is comparable to studies on the exploration scale (Pratt, Huang, Duric, & Littrup, 2007).

Hence, we can apply the theory and methods developed in the previous section to determine the optimal locations of ultrasound transducers in a USCT system. To this end, we extend previous results obtained by Korta Martiartu, Boehm, Vinard, Jovanović Balic, and Fichtner (2017) and consider a hemispherically shaped water tank with a radius of 10 cm. We study a full 3D setup and two different 2D setups to image slices of the human breast in coronal and sagittal planes, respectively. Because the temperature of the surrounding water can be controlled and, thus, its acoustic properties are known, the model space is restricted to the subregion that encloses the breast including a small threshold to account for an inaccurate positioning or patient movement. This defines the region of interest and allows us to eliminate all columns of $\mathbf{J}$ corresponding to model parameters $\mathbf{m}$ that are outside of this region. In all numerical examples, every transducer acts in sending and receiving mode; that is, sequentially each transducer is emitting, while all other transducers are recording the signal. Hence, the total number of experiments grows quadratically with the number of transducers.

The goal of this section is (1) to compare GOED with SOED, (2) to analyze the differences when modeling with straight rays instead of the wave equation, and (3) to study the influence of the reference model on the transducer configuration.

In a first step, we consider a straight ray approximation in a 3D setup with 256 transducers, as shown in Fig. 3, and compute an optimized design by maximizing the trace of $\mathbf{J}^{\mathbf{T}}\mathbf{J}$ normalized by the largest eigenvalue (Curtis, 2004). Fig. 3 compares a reference configuration consisting of uniformly distributed transducers with optimized designs obtained with GOED and SOED, respectively. We observe that although GOED and SOED yield slightly different results, they both have similar patterns that include a ring of transducers close to the chest wall (i.e., near the equator of the

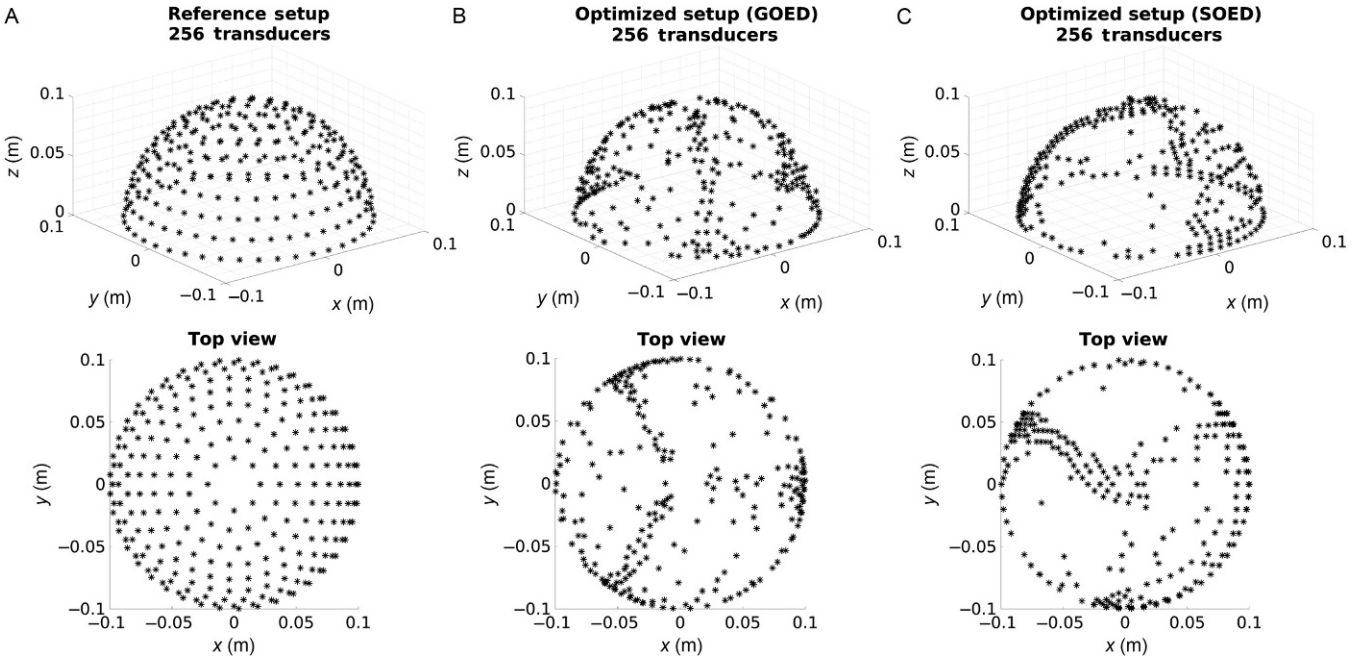

Fig. 3 (A) Reference experimental design with 256 uniformly distributed transducers. (B) Experimental design computed with GOED. (C) Experimental design obtained with SOED.

hemisphere) and at least one arc of densely clustered transducers. The majority of the remaining transducers have an angular distance of at least 120° from the main arc. Fig. 4 shows the normalized eigenvalue spectra of the three different configurations. The optimized designs obtained from GOED and SOED improve the relative magnitudes of the eigenvalues, which translates into a higher resolution. In addition, they also increase the number of significant eigenvalues, which allows us to collect information about the model that is missing in the reference configuration.

As pointed out in the previous section, a possible limitation of SOED is that it is a so-called greedy algorithm, which—by construction—always selects the next best location, but does not necessarily yield the globally best design for a given number of sensors. Fig. 4 shows that GOED indeed improves the spectrum for small eigenvalues compared to SOED, but the differences are marginal. Furthermore, SOED has two important advantages over GOED. On the one hand, the computational costs of SOED are significantly smaller, and on the other hand, SOED enables us to analyze the benefit–cost curve to determine a suitable number of transducers, whereas this number has to be fixed a priori for GOED to make it computationally tractable.

In the next step, we consider a sagittal slice through the center of the hemisphere and compare the optimized transducer configurations for straight rays and FWI. Here, we use the trace of the approximate Hessian and g_T as a quality measure. We apply SOED to iteratively remove transducers from a comprehensive data set consisting of a dense transducer grid with an equiangular spacing of 3°. The transducers sequentially emit a pressure pulse, which is modeled by a Ricker wavelet with a dominant frequency of 200 kHz. The results for straight rays and 18 transducers are shown in the left column of Fig. 5. The optimized designs significantly increase the

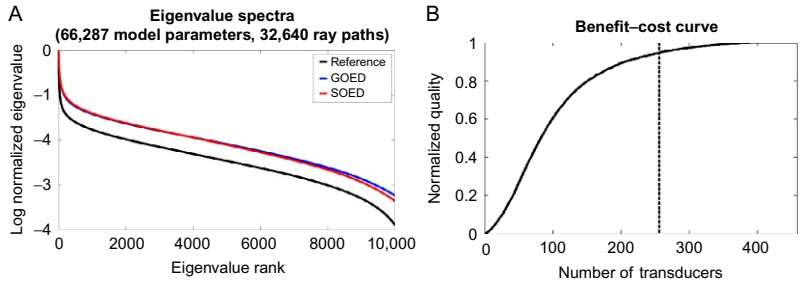

Fig. 4 (A) Log-normalized eigenvalue spectra of the three different configurations shown in Fig. 3. (B) Benefit–cost curve obtained from SOED showing how the quality measure increases with the number of transducers. The *dashed line* indicates the number of transducers selected in this study.

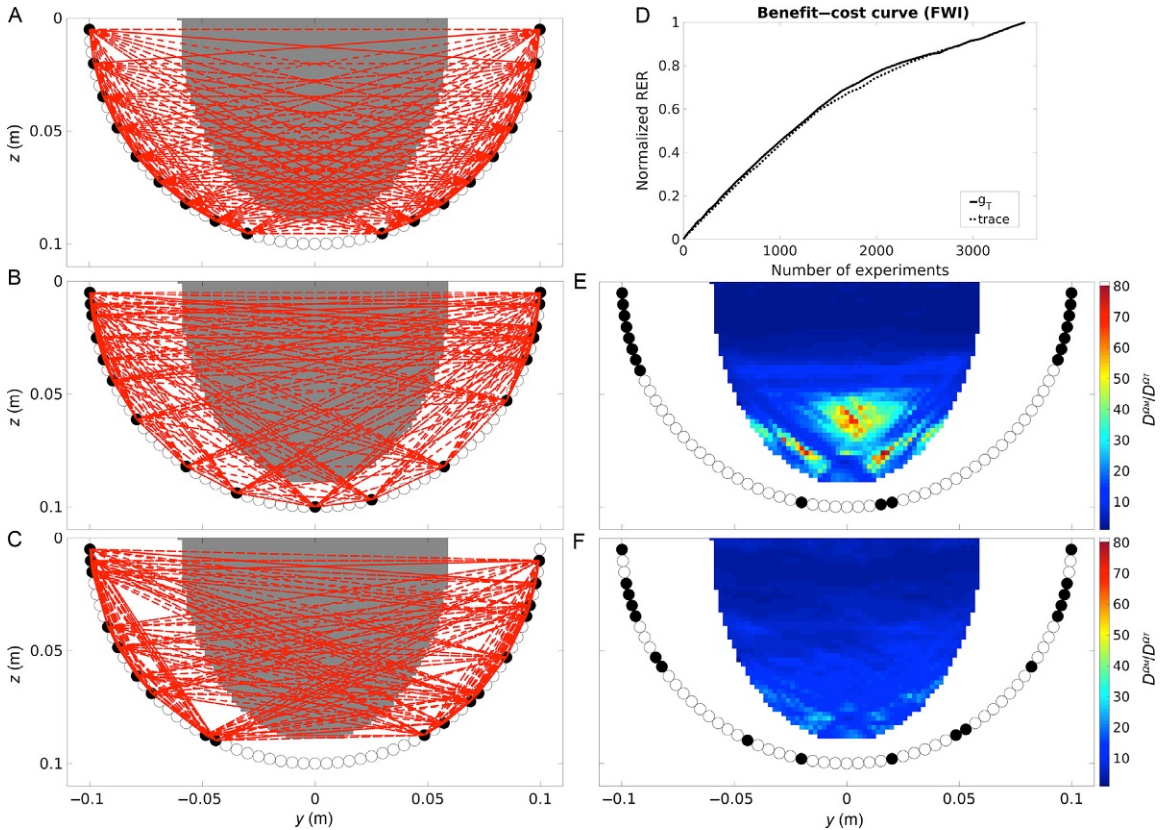

Fig. 5 Results of SOED for sagittal slices using either a straight ray approximation (*left column*) or FWI (*right column*). *Black circles* indicate the selected transducer positions. (A) Reference configuration using 18 equiangular spaced transducers. The *gray-shaded area* indicates the region of interest. (B, C) Optimized configurations using straight rays and either the normalized trace (B) or g_T (C), respectively, as a design criterion. (D) Benefit–cost curves for FWI. (E, F) Optimized configurations using FWI and the trace (E) or g_T (F), respectively. The *color-coded area* indicates the space-dependent ratios $D^{\Omega_M}/D^{\Omega_T}$.

ray density within the region of interest. This compensates for the poor ray coverage in the upper part of the breast close to the chest wall, which we observe for uniformly spaced transducers, and yields a more balanced coverage in the whole region of interest. The results for FWI are shown in the right column of Fig. 5. The trace of the approximate Hessian as a quality criterion gives a poor configuration focusing only on the upper half of the region of interest. Using g_T as a design criterion yields a more even distribution of transducers. This leads to a better coverage in the lower half while maintaining a good coverage in the upper half and a steeper benefit–cost curve.

Fig. 6 shows the optimized configurations for a coronal slice in the upper part of the breast close to the chest wall, where the region of interest is restricted to a central disk with a radius of 6 cm. The initial model is a

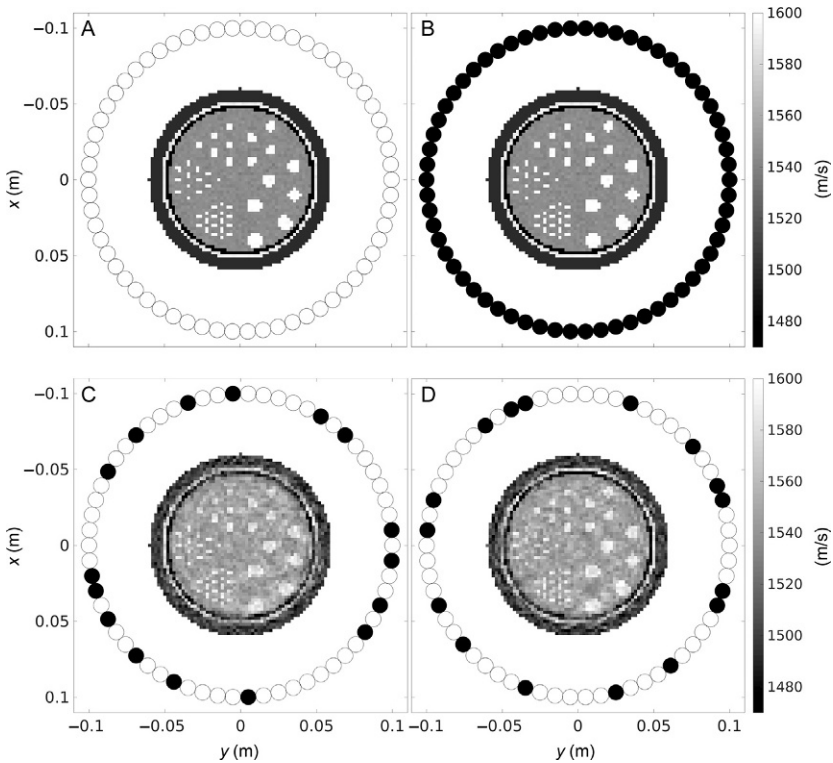

Fig. 6 SOED with FWI for coronal slices. (A) True model and possible transducer locations. (B) Reconstruction using the comprehensive data set with all 62 transducers. (C) Reconstruction using the configuration computed with the homogeneous reference model. (D) Reconstruction using the configuration computed with measurements of the true phantom.

homogeneous breast phantom centered within the region of interest. This example considers a small modification to the design criterion g_T, where the sum in Eq. (6) is replaced by the maximum over all indices. This does not generate any additional cost. The optimized design places the transducers quite evenly along the ring providing a good coverage in the whole region of interest.

The FWI reconstruction obtained from using only 16 transducers already contains most of the anomalies that are detected when using the comprehensive data set. This reduces the costs in terms of acquisition and computation by a factor of 4.

Because USCT scanners can obtain a huge number of scans in a short amount of time and at low costs, the optimal design for FWI can often be determined *postacquisition* with the goal of selecting a subset of sources to reduce the computational cost of FWI. Therefore, we recomputed the optimized design using data generated by the true phantom. This gives qualitatively similar configuration and reconstruction, which confirms that the model has a minor influence on the optimal design in this application.

In summary, we make several simplifying assumptions and approximations in the course of computing the optimized design. First, we linearize the inverse problem and work only with a Gauss–Newton approximation of the Hessian evaluated at the initial model parameters $\mathbf{m}$. Second, we approximate the information content based on the properties of the trace of the approximate Hessian, which neglects interparameter correlations and higher moments. Finally, we do not solve the experimental design problem exactly but with the help of SOED. However, the results of this section confirm that these simplifications still capture the main characteristics of the design. Furthermore, it is important to note that there is, in general, no need to actually determine the global optimum, because any improvement of the initial configuration is already helpful to either improve the reconstruction or reduce the cost of data acquisition. Hence, it is important to find a good trade-off between the computational cost of solving the design problem and the expected accuracy of the results. For the design of USCT scanning systems, linearization using the Gauss–Newton approximation is a valid approach, because the anomalies between the true and the initial sound speed model differ only by a few percent. Moreover, a straight ray approximation provides already some preliminary insights without the need to simulate the wave equation. The same methodology can be used to extend the analysis to other design parameters, in particular in combination with source-encoding strategies (Haber, van den Doel, & Horesh, 2015; see also Section 5.1).

3.2 Elastic FWI of Shallow Surface Seismic Data

FWI applications on the exploration scale are primarily employed for reverse-time migration (e.g., Rønholt et al., 2014), and the experimental setup has to be chosen to meet the requirements of the migration algorithm (e.g., Yilmaz & Doherty, 2001). In contrast, for imaging shallow structures the FWI tomograms are typically the final product. Therefore, it is not necessarily required to meet the spatial sampling criteria associated with seismic reflection processing. Nevertheless, it is common practice to acquire such data sets, as one would use them for reflection processing. Nuber et al. (2017) have performed an in-depth study on this issue using tools from SOED. Here, we report on key results of their investigations.

The test model is shown in Fig. 7. For the elastic case, V_s is obtained from V_p by applying a constant Poisson's ratio of 0.29, and the density ρ is obtained from V_p using Gardner's relation (Gardner, Gardner, & Gregory, 1974). A 24-Hz Ricker wavelet was used for producing the synthetic data set. Seven inversion frequencies were considered accordingly: 6.4, 9.6, 12.8, 19.2, 25.6, 36.8, and 48.0 Hz, in order to cover the full wavenumber domain (Sirgue & Pratt, 2004).

In a first step, it was made use of the acoustic approximation, and 62 equally spaced sources (10 m spacing) and 31 receivers (20 m spacing) were considered in the experiment interval shown in Fig. 7. It was assumed that the receivers remain fixed, and only the number and position of sources will be optimized. The SOED algorithm was initialized by determining the shot position with the largest nRER value. Its location is displayed in Fig. 8B. As shown in the benefit–cost curve in Fig. 8A, a single shot offers

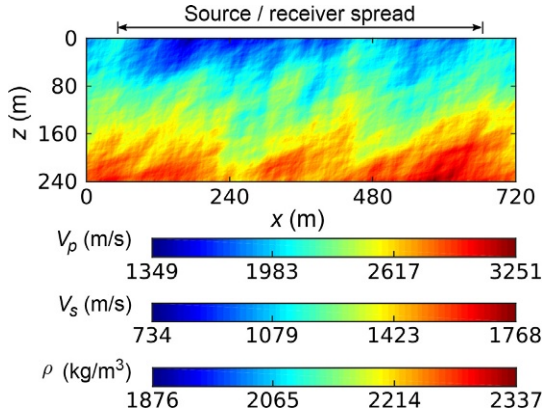

Fig. 7 Test model considered for shallow seismic surveying.

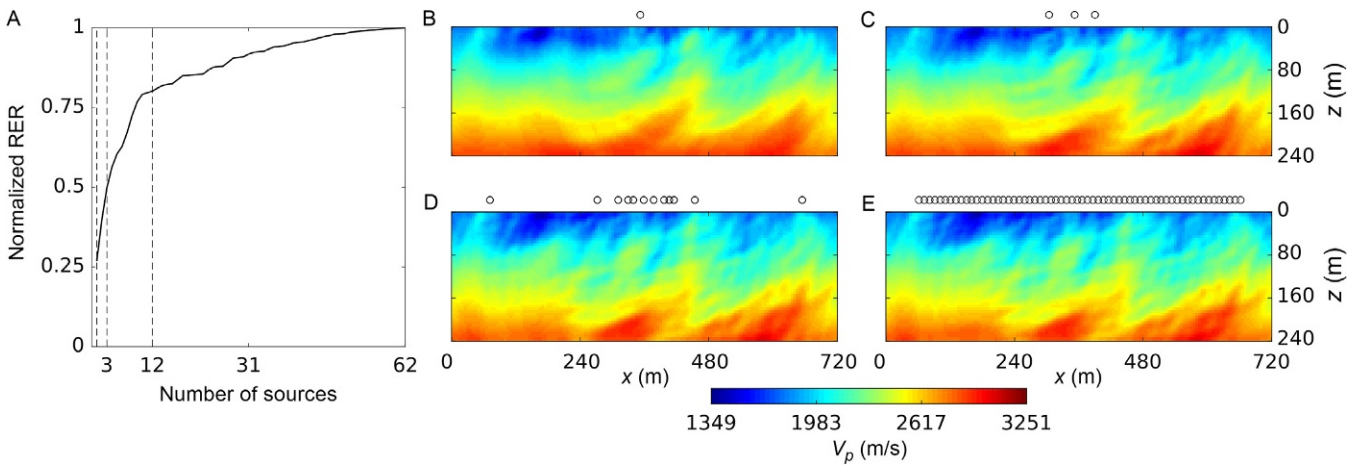

Fig. 8 Results from acoustic SOED. (A) Benefit–cost curve for the sequential design. (B) Position of the first shot (largest nRER) and the corresponding FWI tomogram. (C)–(E) Corresponding results for 3, 12, and 62 (i.e., all) shots.

already ~25% of the information content of the comprehensive data set using all 62 sources. In fact, the corresponding tomogram in Fig. 8B includes most of the primary subsurface features.

Following the recipe outlined in Section 2.2 further shots can be selected. With mere three shots, about 50% of the information content (nRER = 0.5) can be achieved, and the corresponding tomogram, shown in Fig. 8C, is already quite comparable to that obtained with comprehensive data set (Fig. 8E). As shown in Fig. 8A, at about 12 shots the benefit–cost curve enters into the realm of diminishing returns (nRER ~ 0.8), and the corresponding tomogram (Fig. 8D) is hardly distinguishable from those in Fig. 8E.

Results in Fig. 8 suggest amazingly good results using only a single shot, and it seems that with only a few shots, results can be achieved that are comparable to those of the comprehensive data set. However, it needs to be taken into account that these inversions were based on noise-free acoustic data. More realistic scenarios include an elastic subsurface and the presence of noise. The experimental design procedure assumes noise-free data (i.e., only the Jacobian matrix $\mathbf{J}$ and not the data vector d^{obs} is involved). However, noise will have an effect on the tomographic inversions, and it needs to be checked, if a survey layout designed for noise-free data is also suitable in the presence of noise.

To address these two issues, a second design study was performed using all the elastic properties shown in Fig. 7. For that purpose, we have considered x- and z-directed sources and multicomponent receivers. In the following, we denote a particular source–receiver configuration as "*src_type-rec_type*," where *src_type* and *rec_type* can be either x, z, or xz. For example, x-directed sources and multicomponent receivers with x- and z-components are denoted as "x–xz." As for the acoustic experiment, 62 possible source positions and 31 receiver positions were considered, and it was assumed that the receiver spread was kept fixed during the optimization process. All data were contaminated with 30% white noise.

Results for various configurations are shown in Fig. 9. The comprehensive xz–xz configuration (black curve in Fig. 9A) yields excellent results. The corresponding V_s tomogram, obtained with all source components, is shown in Fig. 9E. Since acquiring data with x- and z-directed sources can be very laborious, only x-directed sources and multicomponent geophones were considered in the next simulation. The benefit–cost curve in Fig. 9A is almost identical with those of the comprehensive data set. For the test inversion, a data set containing 80% of the information of all

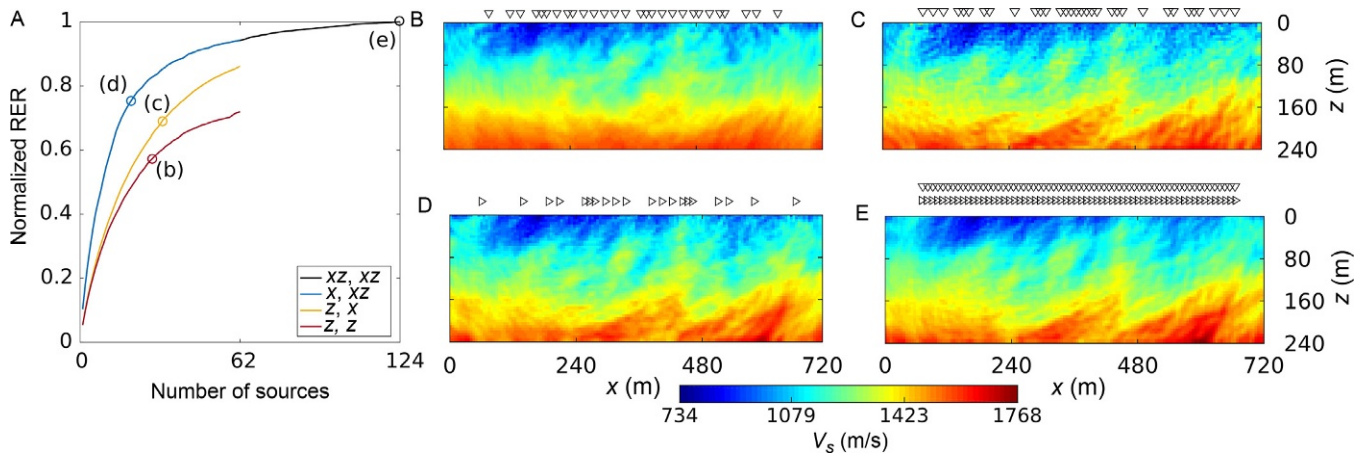

Fig. 9 Results from elastic SOED in the presence of noise. (A) Benefit–cost curve for the individual sequential designs (note that the horizontal axis denotes source components and not source positions). Therefore, the *xz*–*xz* configuration includes 124 sources. (B) Source positions and tomogram determined for the *z*–*z* experiment at the nRER = 0.8 level (*open dot* labeled (B) in (A)). (C) and (D) Source positions and tomograms for the *z*–*x* and *x*–*xz* experiments. As for (A), the tomograms were computed with data sets at the nRER = 0.8 level (*open dot* labeled (C) and (D) in (A)). (E) The solution of the comprehensive data set using all *xz*–*xz* configurations.

x–xz configurations was selected (20 sources, labeled (d) in Fig. 9A). The resulting V_s tomogram is shown in Fig. 9D. As predicted by the benefit–cost curve, it is of comparable quality compared with the tomogram in Fig. 9E. For comparison, we repeated the corresponding computations with the popular z–z configuration, and with the z–x configuration. The benefit–cost curves in Fig. 9A indicate that z–z configurations are expected to offer considerably less information. If a single-component source and a single-component receiver experiment should be devised, it is rather advisable to consider either z–x (or the reciprocal x–z) configurations. According to the corresponding benefit–cost curves in Fig. 9A, x–z or z–x configurations should yield better results (black curve in Fig. 9A). Indeed, this is confirmed by the quality of the tomograms shown in Fig. 9B and C. Here, we only show V_s tomograms, but similar conclusions can be drawn from the V_p and ρ tomograms (see Nuber et al., 2017 for more details).

These examples from the Nuber et al. (2017) study demonstrate clearly the benefits of SOED applied to shallow seismic data. However, we also see substantial benefits for exploration-scale applications. Although a dense and regular spatial sampling is required for the migration of such data, it may be not necessary to include all data acquired for the FWI processing step. 3D elastic FWI of large-scale comprehensive data sets is still pushing the limits of available computing resources, and this will likely persists in a foreseeable future. Therefore, it could be advantageous to employ SOED for selecting small subsets out of a large-scale 3D volume, with which FWI could be performed in a more efficient manner without degrading the quality of the results significantly.

3.3 Elastic FWI of Crosshole Data

Results provided in Section 3.2 demonstrated that both the number of sources (and receivers) and the choice of the recording components are important for designing appropriate elastic FWI surface experiments. A similar study was performed by Manukyan, Latzel, Maurer, Marelli, and Greenhalgh (2012). Here, it was focused on elastic FWI applied to crosshole tomography problems.

The experimental setup and the modeling scenario are shown in Fig. 10A–C. It comprises 41 source positions in the left borehole and 41 receiver positions in the right borehole. 9 frequencies in the range of 300–1500 Hz were considered. Following the typical strategy of frequency-domain inversions, only 300 Hz frequency was considered during the first

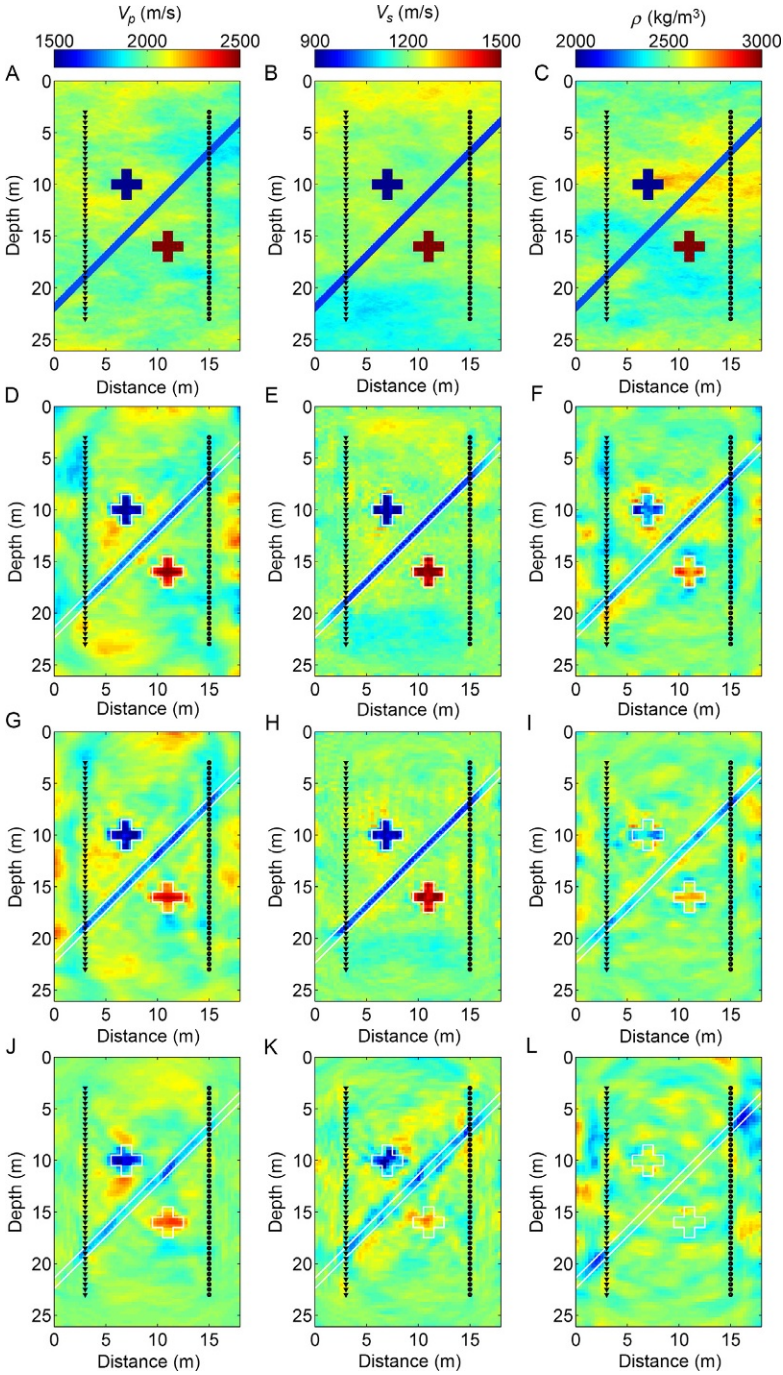

Fig. 10 Elastic FWI results using various source–receiver types. Sources are placed in the left hole (*crosses*), and receivers are placed in the right hole (*dots*). *Left column* shows V_p tomograms, *middle column* shows V_s tomograms, and *right column* shows density tomograms. (A)–(C) True model structures and (D)–(F) tomograms obtained with horizontally (x) directed sources and x- and z (depth)-directed receivers. (G)–(I) Tomograms obtained with pressure sources and x- and z-directed receivers. (J)–(L) Tomograms obtained with pressure sources and pressure receivers.

few iterations, and higher frequencies were subsequently added. Convergence of the full data set was typically achieved after 45 iterations.

It is very difficult to employ vertically oriented directional sources, but it is very common to either use horizontally oriented sources (i.e., perpendicular to the borehole wall) or isotropic pressure sources. For a 2D setup, as considered in this modeling study, it is possible to either record the vertical and/or horizontal displacement field, or sense the pressure field in the receiver borehole.

Since pressure sources and receivers are primarily sensitive to P waves, one would expect that directional sources and receivers would offer the best results for elastic FWI. Therefore, we considered as a realistic *comprehensive data set* a scenario, where horizontal (x-directed) sources and multicomponent (x- and z-directed) receivers were considered. Inversion results for such a data set are shown in Fig. 10D–F. There is an excellent reconstruction of the S-wave velocity structure (Fig. 10E). Due to the longer wavelengths, the P-wave tomogram has a somewhat degraded quality (Fig. 10D), but it still can be considered to be acceptably good. The notorious difficulty to resolve density is shown in Fig. 10F. The reconstruction quality is poor, but the main features are still recognizable.

Implementing a directed source can be a difficult task, particularly when the borehole wall exhibits a certain roughness. In such situations the seismic waves must be generated by a pressure source, either with a borehole sparker or with a borehole air gun. Pressure sources do not radiate S waves, and the S-wave tomograms are thus based entirely on the information contained in P-to-S converted phases. The tomograms obtained with a pressure source and multicomponent receivers are shown in Fig. 10G–I. The P- and S-wave tomograms exhibit a comparable quality as those for the directed sources, but there is virtually no information available on the density.

Multicomponent borehole recordings can be typically performed with strings of only a few geophones. This makes the data acquisition laborious. In contrast, hydrophone streamers (i.e., pressure receivers) allow a large amount of receivers to be operated simultaneously. However, the recording capability of S waves with pressure receivers is limited. The tomograms obtained with pressure sources and pressure receivers are shown in Fig. 10J–L. The quality of the P-wave tomogram (Fig. 10J) is comparable to those in Fig. 10A and D, but, not surprisingly, there is a substantial loss of quality in the S-wave tomogram (Fig. 10K), and the density tomogram (Fig. 10L) is dominated by artifacts.

This synthetic study revealed that a combination of pressure sources and pressure receivers is clearly inadequate for elastic FWI of crosshole experiments, unless one is interested only in the P-wave velocity structure. In contrast, a combination of pressure sources and multicomponent receivers offers only a slightly poorer information content as a data set acquired with directional sources and multicomponent geophones. This conclusion has important consequences for the design of crosshole experiments, where elastic FWI should be applied.

3.4 VSP Imaging

The studies presented in Sections 3.1–3.3 highlighted the potential of OED for FWI applications. As discussed in Maurer et al. (2010), OED is a versatile method that can be applied to any geophysical survey design problem. It is even applicable, when the data analysis is not based on tools from the inversion theory.

This is demonstrated with a design study devoted to the characterization of deep geothermal reservoirs (Reiser, Schmelzbach, Maurer, Greenhalgh, & Hellwig, 2017). A particular challenge of such a task is the need to image small-scale features with sizes in the tens of meters range at great depths of a few kilometers. Often, there is only one borehole available that allows placing receivers and in rare cases sources at depth making VSP a popular subsurface imaging option (e.g., Hardage, 2000). The positioning of the receivers in the borehole is often limited by the small number of sensors of common VSP tools. In contrast, the surface source positions can be chosen more freely. Based on a simple 2D acoustic example, it is shown how optimal source positions can be determined with SOED.

The situation is illustrated in Fig. 11. Four different fracture configurations with dips of either 30° or 70°, and either intersecting or not intersecting the borehole are considered. Sixty-one receivers were placed at 20 m intervals between 3700 and 4900 m depth. The comprehensive data set includes recordings from 91 source positions equally spaced between 0 and 9000 m distance at the surface. Synthetic data were computed using a 40-Hz Ricker wavelet and the SOFI2D software (Bohlen, 2002). VSP data processing included geometrical spreading correction, tau-p filtering for the wavefield separation (separating upgoing (signal) and downgoing (coherent noise) wavefield), first-arrival muting, and Kirchhoff-depth migration. The fracture images using the comprehensive data set are shown in Fig. 11C–F.

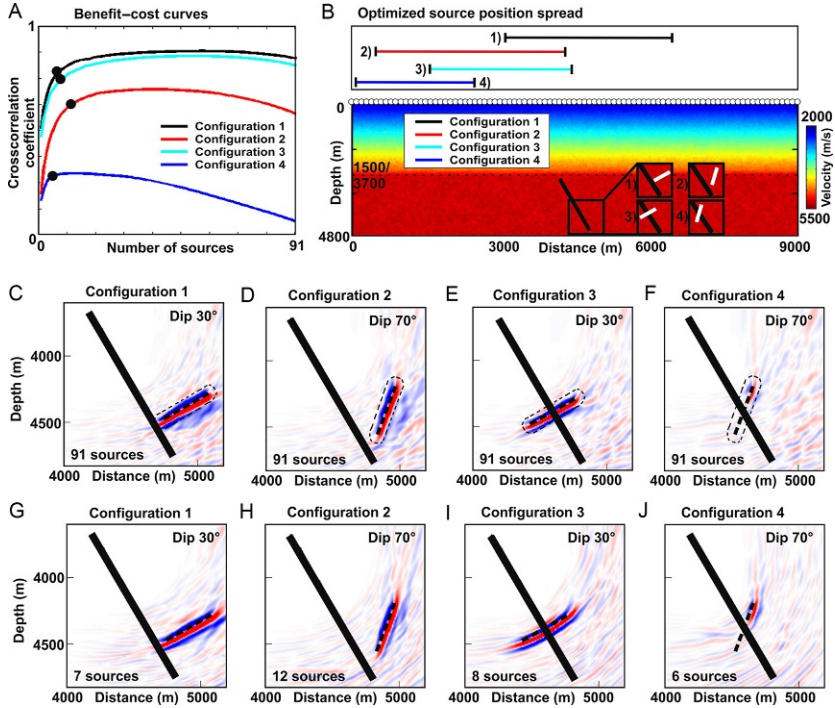

Fig. 11 Survey design for VSP imaging. (A) Benefit–cost curves for four different fracture orientations and positions, as shown in (B). The *black dots* indicate the number of shots with an optimal benefit/cost ratio. (B) Experimental setup showing possible source positions (*white dots*), the subsurface velocity model (note that the depth range between 1500 and 3700 m is not shown), the receiver spread (*solid thick line* between 3800 and 4700 m depth), and the position and orientation of the four fracture configurations (fractures are shown as *white lines*). On top of (B) the optimized distance range for the individual fracture configurations is shown. (C)–(F) VSP images of the fracture using the comprehensive data set. (G)–(J) VSP images of the fractures using the optimized data sets.

For determining an optimal subset of sources, a measure of goodness, comparable to the nRER, had to be established. Since the images in Fig. 11C–F still contain minor artifacts that could not be removed by the processing, a tapered window was applied and only that part of the migrated image was extracted as the reference solution, such that only the desired features remained in the target image (see a dashed black line in Fig. 11C–F enclosing the target). The goodness of any subsequently derived test image (migration result obtained from subsets of the comprehensive data set) was quantified by the zero-lag 2D crosscorrelation coefficient of the test image with the target image.

When optimizing the survey geometry for a particular fracture zone orientation, 91 test images corresponding to 91 migrated single-source images were produced. These test images were then individually crosscorrelated with the target image, and the single-source image with the largest crosscorrelation coefficient was selected. Then, the most suitable add-on single-source image was determined by computing all possible stacks of two single-source images. Following this sequential experimental design strategy allowed benefit–cost curves (benefit corresponding to the crosscorrelation coefficient, cost corresponding to the number of single-source images) to be constructed (Fig. 11A). Note that. the benefit–cost curve does not reach a value of 1 for the complete data set since it is crosscorrelated with the tapered full survey image.

The benefit–cost curve strongly increases when combining only a small number of sources, but flattens out with an increasing number of stacked single-source images. When the increase of the crosscorrelation coefficient from one stack to the next became smaller than 1%, the resulting stacked images were deemed to no longer improve significantly. Hence, this point of diminishing returns defines the optimal selection of single-source images and corresponding source positions (black dots in Fig. 11A).

As shown in Fig. 11G–J, the images based on the optimized data sets are of comparable quality to those obtained with the comprehensive data sets. It is also noteworthy that the benefit–cost curves in Fig. 11A start decreasing toward larger number of sources. This is particularly pronounced for configuration 4 and indicates that some single-source images in the comprehensive data set contain no significant signal, but only noise such as migration artifacts. The diffraction artifacts not only deteriorate the quality of the images but also affect the resulting crosscorrelation with the target image, where tapering removed all artifacts outside of true location of the fracture. In other words, more data do not necessarily improve the image quality!

Extensive testing of the SOED procedure for VSP imaging revealed that the precise shot positions of the optimized data sets are not critical. It is rather relevant, in which distance range the shot positions are chosen predominantly. The optimal distance ranges for the individual configurations are displayed at the top of Fig. 11B. There are considerable differences for the individual configurations.

This (overly) simplistic simulation demonstrates the general applicability of SOED to imaging techniques. As outlined in Reiser et al. (2017), the methodology can be extended to more realistic 3D scenarios. Conceptually,

it is also possible to apply similar algorithms for surface-based seismic reflection processing.

4. EXPLOITING THE INFORMATION CONTENT OF SEISMIC DATA

The studies presented in Section 3 were devoted to find most suitable experimental layouts, which is clearly the main task of experimental design. Once the data are acquired, it is often necessary to make further selections. This can be due to the nonlinearity of the inversion problem to be solved, which is particularly severe for FWI problems. Furthermore, making appropriate choices of subsets can be beneficial for the sake of computational efficiency. Although FWI is designed to exploit the full information content offered by seismic data, it is common practice to invert only selected portions thereof. We review two studies that dealt with this task. First, we show how a sequential experimental design can be used for determining an optimized set of frequencies for performing frequency-domain FWI. Then, it is demonstrated how suitable time windows can be selected for time-domain inversion of regional seismic data.

4.1 Selection of Temporal Spatial Frequencies

For frequency-domain FWI, it is common practice to consider only a few frequencies. To account for the strong nonlinearities, one typically starts the first few iterations with low frequencies. Then, higher frequencies are added in the course of the iterations. There is a quite extensive literature on this topic (e.g., Mulder & Plessix, 2008). Sirgue and Pratt (2004) suggested an efficient strategy for selecting optimal frequencies for surface-based experiments, and Yokota and Matsushima (2003) devised a similar method for crosshole applications. These techniques make use of the maximum spatial wavenumbers connected with a particular survey design. Here, we review the work of Maurer et al. (2009), and we show how sequential experimental design can be employed to address this problem as well. Additionally, we explore to what extent temporal and spatial frequency sampling trades off, and we discuss the information content offered by different representations of frequency-domain seismic data.

For our simulations, we consider a small-scale crosshole experiment, as shown in Fig. 12. It comprises two anomalies embedded in medium with stochastic fluctuation. For the sake of simplicity, we consider an acoustic problem with constant density. As a comprehensive data set, we choose a

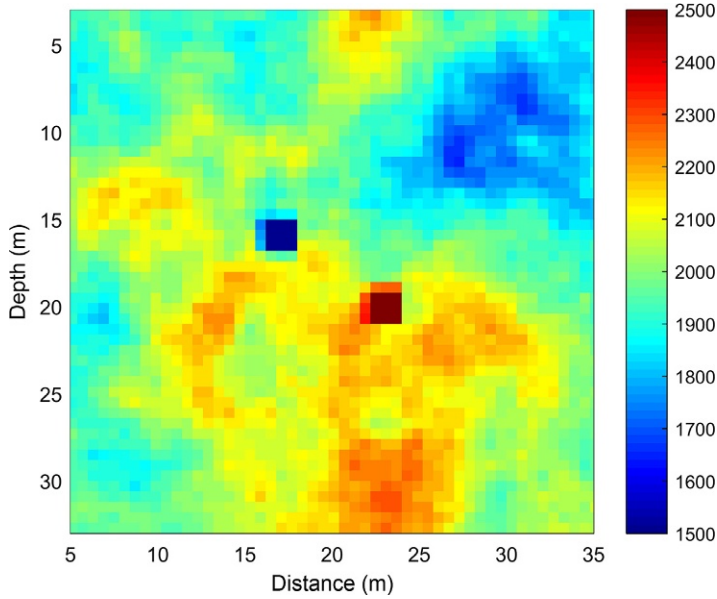

Fig. 12 True model structure for the frequency selection experiment. The sources are placed in a vertical borehole at $x = 5$ m and the receivers are placed in the borehole at $x = 35$ m.

dense source and a receiver deployment with 0.25 m spacing (sources in the left borehole and receivers in the right borehole). The source characteristics are mimicked by a pressure pulse using a Ricker wavelet with a dominant frequency of 700 Hz. The discretized "comprehensive" frequency spectrum includes 30 linearly spaced frequencies between 100 and 1500 Hz.

Frequency-domain waveform data include complex-valued data points of the form $d(\omega, s, r) = d^{real} + id^{imag}$ with ω representing frequency, s the source position, r the receiver position, and i the imaginary unit. Instead of using the full complex data representation, one may consider (i) only the real part d^{real}, (ii) the imaginary part d^{imag}, (iii) the amplitude $|d^{real} + id^{imag}|$, (iv) the phase $\arg(d^{real} + id^{imag})$, or (v) the Hartley spectrum $d^{real} - d^{imag}$. These real-valued data representations reduce the memory requirements for storing the Jacobian and/or approximate Hessian matrices. Furthermore, phase-only inversion may be advantageous, when the amplitudes are significantly affected by attenuation effects.

A critical issue with regard to these reduced data representations is their potential loss of information content. This can be quantified with the corresponding eigenvalue spectra of $\mathbf{J}^{\mathbf{T}}\mathbf{J}$. An example computed

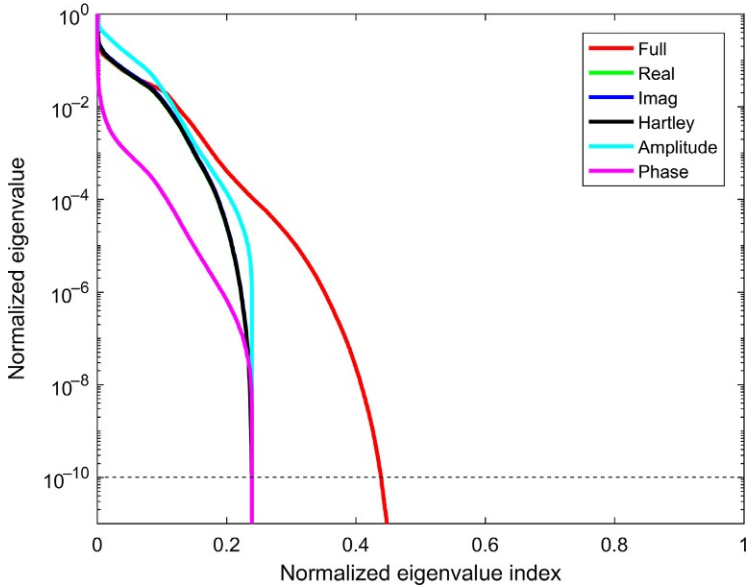

Fig. 13 Normalized eigenvalue spectra for different data representations computed with the experimental setup shown in Fig. 12 and a frequency of 750 Hz. Note that the spectra for real part only (*green*), imaginary part only (*blue*), and Hartley spectrum (*black*) are on top of each other. *Horizontal dashed line* indicates the threshold value, where the RER can be computed.

with the comprehensive source–receiver geometry and a single frequency of 750 Hz is shown in Fig. 13. The corresponding RER values (to be determined along the horizontal dashed line) indicate clearly that all the reduced data representations yield a considerable loss of information, and the full complex spectrum should be thus used, whenever possible. The results, shown in Fig. 13, were obtained using the true velocity model (Fig. 12), but further simulations with homogeneous velocity models and other frequencies and source–receiver configurations led to the same conclusions. Consequently, all the remaining computations were performed with the full complex data.

With SOED, as described in Section 2.2, it is possible to identify the most suitable combination of frequencies for the crosshole FWI problem depicted in Fig. 12. As an initial frequency, we have always chosen the lowest frequency, which is essential for not letting the FWI algorithm trapped in a local minimum. The design process was repeated for several source and receiver spacings ranging from 0.25 up to 4 m. Since we generally do not

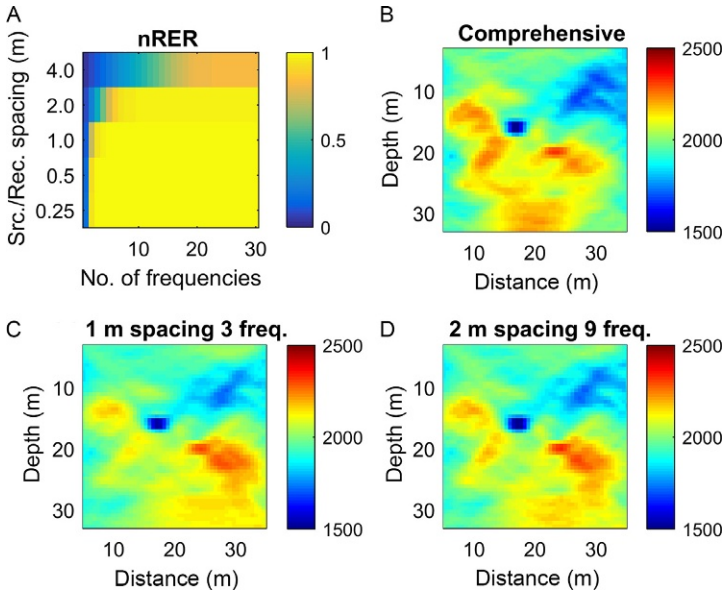

Fig. 14 (A) nRER values computed for different source and receiver spacings and optimally selected frequencies. (B) Tomogram obtained with the comprehensive data set (0.25 m source and receiver spacing all 30 frequencies). (C) Tomogram obtained with 1 m spacing and 3 frequencies and (D) 2 m spacing and 9 frequencies.

have advanced knowledge on the subsurface properties available during the design stage, we have computed the Jacobian matrix **J** on the basis of a homogeneous velocity model, but additional computations using the true subsurface model essentially led to the same results.

They are summarized in Fig. 14. Up to a spatial sampling of 1 m mere 3 frequencies are sufficient to reach a similar design goodness, as one would obtain with the comprehensive data set including all frequencies. With a spatial sampling of 2 m, up to 9 frequencies are required for achieving similarly good results, and with a 4 m spacing even including all frequencies does not yield the levels of the comprehensive data set. It is noteworthy that there are only marginal benefits expected, when choosing a spatial sampling smaller than 1 m. As discussed in more detail in Maurer et al. (2009), the sequence of the frequency choices is as follows. First, frequencies at the upper end of the frequency band are chosen. Then, the choice alternates by low and high frequencies. Interestingly, there is no preference for the frequencies near the dominant frequency of the Ricker wavelet, although these data would provide the largest amplitudes.

The results in Fig. 14A suggest that there is a trade-off between temporal and spatial sampling; that is, 3 frequencies and a spatial sampling of 1 m should provide similar results as 9 optimally selected frequencies and a spatial sampling of 2 m. The corresponding inversion results, shown in Fig. 14C and D, demonstrate that this is indeed the case. The two corresponding tomograms are very similar, and there is also a good match with the result obtained with the comprehensive data set and all frequencies (Fig. 14B), which must be expected on the basis of the nRER diagram shown in Fig. 14A.

4.2 Constructing Optimal Observables

The comprehensive characterization of the Earth's internal structure requires the estimation of more than one physical parameter class, that is, the solution of a multiparameter inverse problem. Typical parameter classes, denoted by $\mathbf{m}_i$, include P and S velocity, attenuation, and parameters describing anisotropy. In realistic, ill-posed inverse problems, different parameter classes cannot be resolved independently. Instead, they map into each other.

In addition to the optimization of the experimental configuration, such interparameter trade-offs can be minimized through the design of optimal observables—a concept introduced to geophysics by the seminal contributions of Backus and Gilbert (1968, 1970) and further popularized by the influential review of Parker (1977). Later work in the context of finite-frequency tomography and FWI (e.g., Bernauer, Fichtner, & Igel, 2014; Sieminski, Trampert, & Tromp, 2009) very much builds on this foundation. In the following paragraphs, we briefly review the theoretical background and provide an example on the optimization of regional-scale finite-frequency observables.

To set the stage, we consider a set of fundamental observables, d_i, that constitute a set of measurements that can be performed on the recorded data. These may be, for instance, the travel times and amplitudes of various wave packets at different frequencies. Our goal is to find a linear combination of the fundamental observables,

$$d = \sum_{i=1}^{n} w_i d_i, \tag{8}$$

such that the sensitivity of the combined observable d with respect to the parameter class of interest is maximized, while sensitivity to all other

parameter classes is minimized. This involves an optimization problem for the weights w_i in Eq. (8). To find optimal weights, we first notice that the variation of the fundamental observable d_i can be expressed in terms of variations $\delta\mathbf{m}_j$ of the jth parameter class, and the corresponding Jacobians or sensitivities $\mathbf{J}_{ij}$

$$\delta d_i = \sum_{j=1}^{p} \mathbf{J}_{ij}^{\mathrm{T}} \delta\mathbf{m}_j, \tag{9}$$

where p is the total number of parameter classes. It follows that the variation of the combined observable, d, is given by

$$\delta d = \sum_{i=1}^{n} \sum_{j=1}^{p} w_i \mathbf{J}_{ij}^{\mathrm{T}} \delta\mathbf{m}_j = \sum_{j=1}^{p} \mathbf{J}_j^{\mathrm{T}} \delta\mathbf{m}_j, \tag{10}$$

where $\mathbf{J}_i = \sum_{i=1}^{n} w_i \mathbf{J}_{ij}$ is the combined Jacobian for d with respect to parameter class $\mathbf{m}_j$. Without loss of generality, we assume that our parameter class of interest is $\mathbf{m}_1$, and we consider the sensitivity power (Sieminski et al., 2009)

$$P_j(\mathbf{w}) = \mathbf{J}_j^{\mathrm{T}} \mathbf{J}_j \tag{11}$$

as the quantity that we wish to maximize for $j=1$ and minimize for $j>1$ with respect to the vector $\mathbf{w}$ of weighting coefficients. This joint maximization and minimization problem can be recast into a single maximization problem for the objective functional

$$\chi(\mathbf{w}) = \sum_{j=1}^{p} b_j P_j(\mathbf{w}). \tag{12}$$

The balancing coefficients $b_1 > 0$ and $b_{j>1} < 0$ control the extent to which sensitivity power with respect to class $\mathbf{m}_1$ is maximized, while sensitivity power with respect to classes $\mathbf{m}_{j>1}$ is minimized. For fixed balancing coefficients, the maximization of χ constitutes a small least-squares problem that merely involves the solution of a small $n \times n$ linear system for the weights w_i. If needed, the result can be improved by a trial-and-error adjustment of the balancing coefficients.

We illustrate the concept of optimal observable design with an example from regional seismology, where we consider an earthquake recorded at the 20.98° epicentral distance (Fig. 15). Our goal is to construct an optimal

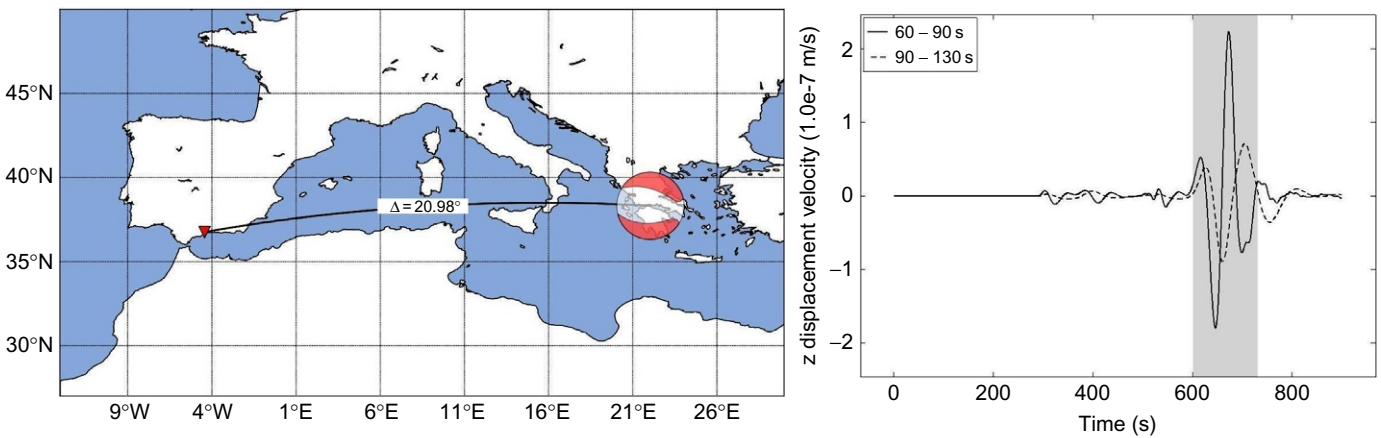

Fig. 15 (A) *Left*: Source–receiver geometry for an earthquake beneath southern Greece and a receiver in southern Spain, at 20.98° epicentral distance. The Earth model is the spherically symmetric AK135 (Kennett, Engdahl, & Buland, 1995). The source mechanism is indicated by the beach ball at the source location. *Right*: Vertical-component synthetic seismograms in the 60–90 and 90–130 s period bands. Finite-frequency travel time measurements (Luo & Schuster, 1991) are performed within the *gray-shaded* surface wave window. *Modified from Bernauer, M., Fichtner, A., & Igel, H. (2014). Optimal observables for multiparameter seismic tomography.* Geophysical Journal International, 198*(2), 1241–1254.*

observable that maximizes sensitivity with respect to the vertical density gradient, ρ', by combining surface wave travel time measurements (Luo & Schuster, 1991) in four different period bands, 30–40, 40–60, 60–90, and 90–130 s. Simultaneously, we wish to minimize sensitivity with respect to P and S velocity.

Within an individual period band, sensitivity with respect to P velocity is large near the surface. The sensitivities for S velocity and density gradient attain their maxima at greater depth and are geometrically nearly identical, apart from a sign flip. The optimization procedure outlined earlier constructs an optimal combined travel time measurement with weights of −0.11, 0.41, −0.73, and 0.54 for the travel time measurements at periods of 30–40, 40–60, 60–90, and 90–130 s, respectively. As illustrated in Fig. 16, the optimal measurement has negligible sensitivity with respect to P velocity, thereby reducing the original three-parameter problem into a simpler two-parameter problem. By construction, sensitivity to the density gradient is increased, while sensitivity to S velocity is reduced. Furthermore, the sensitivity distributions for the density gradient and S velocity are geometrically different, suggesting that they can be constrained more independently.

While the idea to construct optimal observables for linear inverse problems is as old as inverse theory itself (e.g., Backus & Gilbert, 1968), its application to nonlinear problems—including FWI—is still in its infancy. First results presented here are promising, as they indicate that notoriously poorly constrained parameters such as density may be better resolved. Yet, questions concerning the concrete optimization scheme, the choice of fundamental observables, and the optimal balancing between minimization and maximization of sensitivities remain to be addressed.

5. OTHER OED TECHNIQUES

5.1 Source Encoding

The tremendous costs of FWI applied to large-scale data sets motivated research efforts for reducing the computational burden. A key idea was to consider not the recordings from single sources but the superposition of multiple sources, which is often referred as supershots. This concept can be applied at the data processing stage, but it is also possible to acquire data using simultaneous sources (e.g., Beasley, 2008; Robertsson et al., 2016).

If this technique is applied at the processing stage, it is typically referred as *source encoding*. A fundamental contribution was made by Krebs et al. (2009). They distinguish between simply stacking the signals of several identical sources (coherent sums, e.g., Capdeville, Gung, & Romanowicz, 2005)

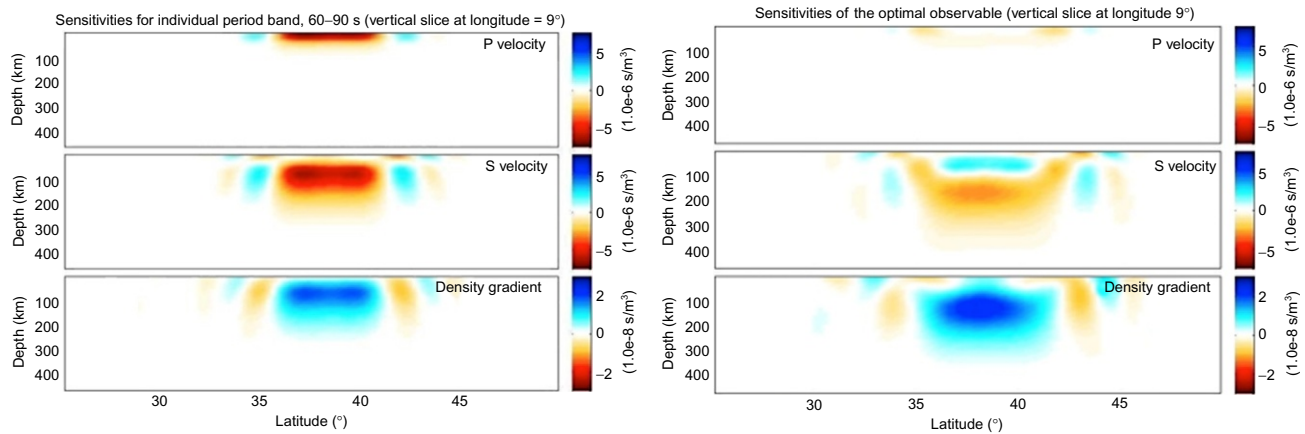

Fig. 16 *Left*: Travel time sensitivities computed via the adjoint method (Fichtner, Bunge, & Igel, 2006; Tarantola, 1988) with respect to P velocity, S velocity, and the density gradient for the individual period band (60–90 s) plotted at 9° longitude. *Right*: Sensitivities for the optimal observable, that is, the combined travel time measurement in four different period bands. *Modified from Bernauer, M., Fichtner, A., & Igel, H. (2014). Optimal observables for multiparameter seismic tomography.* Geophysical Journal International, 198*(2), 1241–1254.*

and stacking signals of sources with different source signatures (incoherent sums, e.g., Romero, Ghiglia, Ober, & Morton, 2000), whereby the (artificial) creation of different source signatures led to the term *source encoding*. Li, Aravkin, van Leeuwen, and Herrmann (2012) formulated this concept in the framework of compressive sensing (e.g., Donoho, 2006). In a more recent work, Haber et al. (2015) suggested a strategy for optimally combining different sources.

Although source encoding offers potentially considerable computational savings (up to a factor equal to the number of shots involved), it has been also realized that the superposition of sources leads to cross talk, and may make the inversion results unstable, particularly in the presence of significant noise (e.g., Ben-Hadj-Ali, Operto, & Virieux, 2011). Several techniques have been suggested to reduce this problem (e.g., Habashy, Abubakar, Pan, & Belani, 2011; Schiemenz & Igel, 2013). A different strategy was proposed by van Leeuwen and Herrmann (2013). They suggested to initially use only a few randomly selected (not superimposed) sources, and to add gradually more sources in the course of the iterations. This technique has some similarities with those presented in Sections 3 and 4.

5.2 Optimized Model Parameterization

All the OED techniques, discussed so far, operate in the data space, and the subsurface model parameterization is assumed to be given and fixed. However, the choice of the goodness of a particular experimental layout is also governed by the model parameterization; that is, a coarse model discretization may require a different source–receiver pattern compared with a very fine discretization.

There are a few papers that have dealt so far with model parameterization issues, primarily in the field of global seismic tomography (e.g., Curtis & Snieder, 1997; Nolet & Montelli, 2005; Simons et al., 2011; Spakman & Bijwaard, 2001). A particularly interesting option is to discretize the subsurface with wavelets (e.g., Foufoula-Georgiou & Kumar, 2014). Such an approach was employed, for example, by Simons et al. (2011) for global tomography and by Chiao and Liang (2003) for general geophysical inversion problems.

5.3 OED and Joint Inversions

Finally, we judge that there are also considerable benefits in combining OED with joint inversion techniques. Joint inversions have been established

for jointly analyzing different data types that are either sensitive to a common subsurface parameter (e.g., Vozoff & Jupp, 1975) or different parameters using cross-gradient constraints (Gallardo & Meju, 2007). It was shown by Shakas and Maurer (2015) that the experimental layout for a particular data type can be reduced considerably, when it is already known at the experimental design stage that a joint inversion with another data type will be performed. For FWI problems, one could, for example, assume that the seismic data will be jointly inverted with inductive electromagnetic data (e.g., Gao, Abubakar, & Habashy, 2012; Hu, Abubakar, & Habashy, 2009).

6. DISCUSSION AND OUTLOOK

In this contribution, we have reviewed a variety of OED techniques applied to FWI problems. It could be shown that a combination of OED and FWI has the potential to offer high-resolution images at affordable acquisition costs. Furthermore, it has been demonstrated that a combination of OED and FWI can reduce the computational costs substantially, which is currently one of the most severe bottlenecks of FWI applications. Despite the usefulness and versatility of actual OED techniques applicable to FWI, there are still several of open questions that require further research.

An important aspect concerns the strong nonlinearity of FWI. As discussed earlier, the OED procedures are surprisingly insensitive to nonlinear effects introduced by an incorrect design model. However, when the design model is substantially different from the true model, it may be necessary to consider nonlinear design methods. The literature already includes important contributions to this topic (e.g., Coles & Curtis, 2011; Guest & Curtis, 2009, 2010; van Den Berg, Curtis, & Trampert, 2003). It could be shown that such techniques are generally applicable to seismic surveys, but they are computationally very expensive.

Even with linear(ized) OED methods the computational costs can become quickly prohibitive, when dealing with experiments that involve a large number of sources and receivers. Coles et al. (2015) presented an algorithm that reduces the computational costs substantially. Based on these promising results, further attempts should be made for further reducing computational costs. Ideally, OED should be carried out almost in real time. This would offer new exciting opportunities for adaptively augmenting seismic surveys, while the field crews are still on site.

As discussed in this chapter, there are basically three options available for optimizing FWI experiments, namely, (i) selecting appropriate

source–receiver patterns (Section 3), (ii) extracting the most useful attributes of the seismic data (Section 4), and (iii) choosing an appropriate model parameterization (Section 5.2). To our knowledge, no attempts have been made so far to establish an OED procedure that combines these aspects. This could be a new and exciting avenue of future research.

Finally, it should be emphasized that seismic surveys include many more parameters that could be optimized with OED techniques. Examples include

- minimizing logistical costs (e.g., moving equipment around with trucks or helicopters for land surveys),
- optimizing source parameters (e.g., tuning vibroseis sweeps for land applications or optimizing air gun arrays for marine applications), and
- exploiting the information content offered by wavefield gradients and/or rotational sensors (e.g., Li & van der Baan, 2017).

REFERENCES

Ajo-Franklin, J. B. (2009). Optimal experiment design for time-lapse traveltime tomography. *Geophysics*, *74*, Q27–Q40.

Backus, G., & Gilbert, F. (1968). The resolving power of gross earth data. *Geophysical Journal International*, *16*(2), 169–205.

Backus, G., & Gilbert, F. (1970). Uniqueness in inversion of inaccurate gross earth data. *Philosophical Transactions of the Royal Society of London Series A-Mathematical and Physical Sciences*, *266*(1173), 123. https://doi.org/10.1098/rsta.1970.0005.

Barth, N., & Wunsch, C. (1990). Oceanographic experiment design by simulated annealing. *Journal of Physical Oceanography*, *20*(9), 1249–1263.

Beasley, C. J. (2008). A new look at marine simultaneous sources. *The Leading Edge*, *27*(7), 914–917. https://doi.org/10.1190/1.2954033.

Ben-Hadj-Ali, H., Operto, S., & Virieux, J. (2011). An efficient frequency-domain full waveform inversion method using simultaneous encoded sources. *Geophysics*, *76*(4), R109–R124.

Bernauer, M., Fichtner, A., & Igel, H. (2014). Optimal observables for multiparameter seismic tomography. *Geophysical Journal International*, *198*(2), 1241–1254.

Bohlen, T. (2002). Parallel 3-D viscoelastic finite difference seismic modelling. *Computers & Geosciences*, *28*(8), 887–899.

Bretaudeau, F., Brossier, R., Leparoux, D., Abraham, O., & Virieux, J. (2013). 2D elastic full-waveform imaging of the near-surface: Application to synthetic and physical modelling data sets. *Near Surface Geophysics*, *11*(3), 307–316. https://doi.org/10.3997/1873-0604.2012067.

Butzer, S., Kurzmann, A., & Bohlen, T. (2013). 3D elastic full-waveform inversion of small-scale heterogeneities in transmission geometry. *Geophysical Prospecting*, *61*(6), 1238–1251.

Capdeville, Y., Gung, Y., & Romanowicz, B. (2005). Towards global earth tomography using the spectral element method: A technique based on source stacking. *Geophysical Journal International*, *162*(2), 541–554.

Chiao, L.-Y., & Liang, W.-T. (2003). Multiresolution parameterization for geophysical inverse problems. *Geophysics*, *68*(1), 199–209.

Coles, D., & Curtis, A. (2011). Efficient nonlinear Bayesian survey design using DN optimization. *Geophysics*, *76*(2), Q1–Q8.

Coles, D., & Prange, M. (2012). Toward efficient computation of the expected relative entropy for nonlinear experimental design. *Inverse Problems*, *28*(5), 055019.

Coles, D., Prange, M., & Djikpesse, H. (2015). Optimal survey design for big data. *Geophysics*, *80*(3), P11–P22. https://doi.org/10.1190/Geo2014-0425.1.

Coles, D., Yang, Y., Djikpesse, H., Prange, M., & Osypov, K. (2013). Optimal nonlinear design of marine borehole seismic surveys. *Geophysics*, *78*(3), WB17–WB29.

Cox, D. R. (1958). *Planning of experiments*. New York: Wiley.

Curtis, A. (1999). Optimal experiment design: Cross-borehole tomographic examples. *Geophysical Journal International*, *136*(3), 637–650.

Curtis, A. (2004). Theory of model-based geophysical survey and experimental design: Part 1—Linear problems. *The Leading Edge*, *23*(10), 997–1004. https://doi.org/10.1190/1.1813346.

Curtis, A., & Snieder, R. (1997). Reconditioning inverse problems using the genetic algorithm and revised parameterization. *Geophysics*, *62*(5), 1524–1532.

Dessa, J. X., Operto, S., Kodaira, S., Nakanishi, A., Pascal, G., Virieux, J., et al. (2004). Multiscale seismic imaging of the eastern Nankai trough by full waveform inversion. *Geophysical Research Letters*, *31*(18), 1–4.

Djikpesse, H. A., Khodja, M. R., Prange, M. D., Duchenne, S., & Menkiti, H. (2012). Bayesian survey design to optimize resolution in waveform inversion. *Geophysics*, 77, R81–R93.

Donoho, D. L. (2006). Compressed sensing. *IEEE Transactions on Information Theory*, *52*(4), 1289–1306.

Duric, N., Littrup, P., Li, C., Roy, O., Schmidt, S., Cheng, X., et al. (2014). Breast imaging with SoftVue: Initial clinical evaluation. *Proceedings of SPIE*, *9040*, 90400V.

Ernst, J. R., Maurer, H., Green, A. G., & Holliger, K. (2007). Full-waveform inversion of crosshole radar data based on 2-D finite-difference time-domain solutions of Maxwell's equations. *IEEE Transactions on Geoscience and Remote Sensing*, *45*(9), 2807–2828. https://doi.org/10.1109/Tgrs.2007.901048.

Fedorov, V. V. (1972). *Theory of optimal experiments*. Elsevier.

Fichtner, A. (2010). *Full seismic waveform modelling and inversion*. Springer Science & Business Media.

Fichtner, A., Bunge, H.-P., & Igel, H. (2006). The adjoint method in seismology: II. Applications: Traveltimes and sensitivity functionals. *Physics of the Earth and Planetary Interiors*, *157*(1), 105–123.

Foufoula-Georgiou, E., & Kumar, P. (2014). Wavelets in geophysics (Vol. 4): Academic Press Cambridge, MA, USA.

Gallardo, L. A., & Meju, M. A. (2007). Joint two-dimensional cross-gradient imaging of magnetotelluric and seismic traveltime data for structural and lithological classification. *Geophysical Journal International*, *169*(3), 1261–1272. https://doi.org/10.1111/j.1365-246X.2007.03366.x.

Gao, G., Abubakar, A., & Habashy, T. M. (2012). Joint petrophysical inversion of electromagnetic and full-waveform seismic data. *Geophysics*, 77(3), WA3–WA18.

Gardner, G., Gardner, L., & Gregory, A. (1974). Formation velocity and density—The diagnostic basics for stratigraphic traps. *Geophysics*, *39*(6), 770–780.

Gibson, R. L., Jr., & Tzimeas, C. (2002). Quantitative measures of image resolution for seismic survey design. *Geophysics*, *67*(6), 1844–1852.

Glenn, W., & Ward, S. (1976). Statistical evaluation of electrical soundlng methods. Part I: Experiment design. *Geophysics*, *41*(6), 1207–1221.

Guest, T., & Curtis, A. (2009). Iteratively constructive sequential design of experiments and surveys with nonlinear parameter-data relationships. *Journal of Geophysical Research: Solid Earth*, *114*(B4). B04307.

Guest, T., & Curtis, A. (2010). Optimal trace selection for AVA processing of shale-sand reservoirs. *Geophysics*, *75*(4), C37–C47.

Guest, T., & Curtis, A. (2011). On standard and optimal designs of industrial-scale 2-D seismic surveys. *Geophysical Journal International*, *186*(2), 825–836.
Habashy, T., Abubakar, A., Pan, G., & Belani, A. (2011). Source-receiver compression scheme for full-waveform seismic inversion. *Geophysics*, *76*(4), R95–R108.
Haber, E., Horesh, L., & Tenorio, L. (2008). Numerical methods for experimental design of large-scale linear ill-posed inverse problems. *Inverse Problems*, *24*(5), 055012.
Haber, E., van den Doel, K., & Horesh, L. (2015). Optimal design of simultaneous source encoding. *Inverse Problems in Science and Engineering*, *23*(5), 780–797. https://doi.org/10.1080/17415977.2014.934821.
Hardage, B. A. (2000). *Vertical seismic profiling*. Oxford, UK: Pergamon.
Hardt, M., & Scherbaum, F. (1994). The design of optimum networks for aftershock recordings. *Geophysical Journal International*, *117*(3), 716–726.
Hu, W., Abubakar, A., & Habashy, T. M. (2009). Joint electromagnetic and seismic inversion using structural constraints. *Geophysics*, *74*(6), R99–R109.
Huang, L., Shin, J., Chen, T., Lin, Y., Intrator, M., Hanson, K., et al. (2015). Breast ultrasound tomography with two parallel transducer arrays: Preliminary clinical results. *Proceedings of SPIE*, *9419*, 941916.
Kennett, B., Engdahl, E., & Buland, R. (1995). Constraints on seismic velocities in the Earth from traveltimes. *Geophysical Journal International*, *122*(1), 108–124.
Khodja, M., Prange, M., & Djikpesse, H. (2010). Guided Bayesian optimal experimental design. *Inverse Problems*, *26*(5), 055008.
Kijko, A. (1977). An algorithm for the optimum distribution of a regional seismic network—I. *Pure and Applied Geophysics*, *115*(4), 999–1009.
Korta Martiartu, N., Boehm, C., Vinard, N., Jovanović Balic, I., & Fichtner, A. (2017). Optimal experimental design to position transducers in ultrasound breast imaging. *Proceedings of SPIE*, *10139*, 101390M.
Krebs, J. R., Anderson, J. E., Hinkley, D., Baumstein, A., Lee, S., Neelamani, R., et al. (2009). Fast full wave seismic inversion using source encoding. In *SEG technical program expanded abstracts 2009* (pp. 2273–2277): Society of Exploration Geophysicists.
Lanz, E., Maurer, H., & Green, A. G. (1998). Refraction tomography over a buried waste disposal site. *Geophysics*, *63*(4), 1414–1433.
Li, X., Aravkin, A. Y., van Leeuwen, T., & Herrmann, F. J. (2012). Fast randomized full-waveform inversion with compressive sensing. *Geophysics*, *77*(3), A13–A17.
Li, Z., & van der Baan, M. (2017). Tutorial on rotational seismology and its applications in exploration geophysics. *Geophysics*, *82*(5), 1–54.
Liner, C. L., Underwood, W. D., & Gobeli, R. (1999). 3-D seismic survey design as an optimization problem. *The Leading Edge*, *18*(9), 1054–1060.
Luo, Y., & Schuster, G. T. (1991). Wave-equation traveltime inversion. *Geophysics*, *56*(5), 645–653.
Manukyan, E., Latzel, S., Maurer, H., Marelli, S., & Greenhalgh, S. A. (2012). Exploitation of data-information content in elastic-waveform inversions. *Geophysics*, 77(2), R105–R115. https://doi.org/10.1190/Geo2011-0184.1.
Maurer, H., & Boerner, D. E. (1998). Optimized and robust experimental design: A non-linear application to EM sounding. *Geophysical Journal International*, *132*(2), 458–468.
Maurer, H., Curtis, A., & Boerner, D. E. (2010). Recent advances in optimized geophysical survey design. *Geophysics*, *75*(5), 75A177–175A194.
Maurer, H., Greenhalgh, S., & Latzel, S. (2009). Frequency and spatial sampling strategies for crosshole seismic waveform spectral inversion experiments. *Geophysics*, *74*(6), Wcc79–Wcc89.
Maurer, H., Holliger, K., & Boerner, D. E. (1998). Stochastic regularization: Smoothness or similarity? *Geophysical Research Letters*, *25*(15), 2889–2892.

Meles, G. A., Greenhalgh, S. A., Green, A. G., Maurer, H., & Van der Kruk, J. (2012). GPR full-waveform sensitivity and resolution analysis using an FDTD adjoint method. *IEEE Transactions on Geoscience and Remote Sensing*, *50*(5), 1881–1896. https://doi.org/10.1109/Tgrs.2011.2170078.

Menke, W. (2012). *Geophysical data analysis: Discrete inverse theory* (Matlab ed.). Waltham, MA: Academic Press.

Mora, P. (1987). Nonlinear two-dimensional elastic inversion of multioffset seismic data. *Geophysics*, *52*(9), 1211–1228.

Mulder, W. A., & Plessix, R.-E. (2008). Exploring some issues in acoustic full waveform inversion. *Geophysical Prospecting*, *56*(6), 827–841.

Nihei, K., Robertsson, J. O., Tromp, J., Blanch, J. O., Tsvankin, I., Grechka, V., et al. (2012). *Numerical modeling of seismic wave propagation*. Society of Exploration Geophysicists.

Nolet, G., & Montelli, R. (2005). Optimal parametrization of tomographic models. *Geophysical Journal International*, *161*(2), 365–372.

Nuber, A., Maurer, H., & Manukyan, E. (2017). Optimising measurement geometry for seismic near-surface full waveform inversion. *Geophysical Journal International*, *210*, 1909–1921.

Parker, R. L. (1977). Understanding inverse theory. *Annual Review of Earth and Planetary Sciences*, *5*(1), 35–64.

Pratt, R. G. (1999). Seismic waveform inversion in the frequency domain. Part 1: Theory and verification in a physical scale model. *Geophysics*, *64*(3), 888–901.

Pratt, R. G., Huang, L., Duric, N., & Littrup, P. (2007). Sound-speed and attenuation imaging of breast tissue using waveform tomography of transmission ultrasound data. *Proceedings of SPIE*, *6510*, 65104S.

Pratt, R. G., Shin, C., & Hicks, G. J. (1998). Gauss-Newton and full Newton methods in frequency-space seismic waveform inversion. *Geophysical Journal International*, *133*(2), 341–362.

Rabinowitz, N., & Steinberg, D. M. (1990). Optimal configuration of a seismographic network: A statistical approach. *Bulletin of the Seismological Society of America*, *80*(1), 187–196.

Reiser, F., Schmelzbach, C., Maurer, H., Greenhalgh, S., & Hellwig, O. (2017). Optimizing the design of vertical seismic profiling (VSP) for imaging fracture zones over hardrock basement geothermal environments. *Journal of Applied Geophysics*, *139*, 25–35.

Reynolds, J. M. (2011). *An introduction to applied and environmental geophysics* (2nd ed.). . Chichester, West Sussex; Malden, MA: Wiley-Blackwell.

Robertsson, J., Van Manen, D. J., Amundson, L., Landro, M., Robertsson, J. O. A., van Manen, D. J., et al. (2016). Codes and ciphers, part II: Simultaneous source separation. *GEO ExPro*, *13*, 74–77.

Romero, L. A., Ghiglia, D. C., Ober, C. C., & Morton, S. A. (2000). Phase encoding of shot records in prestack migration. *Geophysics*, *65*(2), 426–436. https://doi.org/10.1190/1.1444737.

Rønholt, G., Korsmo, Ø., Brown, S., Valenciano, A., Whitmore, D., Chemingui, N., et al. (2014). High-fidelity complete wavefield velocity model building and imaging in shallow water environments—A North Sea case study. *First Break*, *32*(6), 127–131.

Ruiter, N. V., Göbel, G., Berger, L., Zapf, M., & Gemmeke, H. (2011). Realization of an optimized 3D USCT. *Proceedings of SPIE*, *7968*, 796805.

Ruiter, N. V., Zapf, M., Hopp, T., Dapp, R., Kretzek, E., Birk, M., et al. (2012). 3D ultrasound computer tomography of the breast: A new era? *European Journal of Radiology*, *81*, S133–S134. https://doi.org/10.1016/S0720-048X(12)70055-4.

Sandhu, G., Li, C., Roy, O., Schmidt, S., & Duric, N. (2015). Frequency domain ultrasound waveform tomography: Breast imaging using a ring transducer. *Physics in Medicine and Biology*, *60*(14), 5381.

Schiemenz, A., & Igel, H. (2013). Accelerated 3-D full-waveform inversion using simultaneously encoded sources in the time domain: Application to Valhall ocean-bottom cable data. *Geophysical Journal International*, *95*(3), 1970–1988.

Sen, M. K., & Stoffa, P. L. (2013). *Global optimization methods in geophysical inversion*. Cambridge, UK: Cambridge University Press.

Shakas, A., & Maurer, H. (2015). In *Strategies for joint geophysical survey design Paper presented at the EGU general assembly conference abstracts*.

Sieminski, A., Trampert, J., & Tromp, J. (2009). Principal component analysis of anisotropic finite-frequency sensitivity kernels. *Geophysical Journal International*, *179*(2), 1186–1198.

Simons, F. J., Loris, I., Nolet, G., Daubechies, I. C., Voronin, S., Judd, J., et al. (2011). Solving or resolving global tomographic models with spherical wavelets, and the scale and sparsity of seismic heterogeneity. *Geophysical Journal International*, *187*(2), 969–988.

Sirgue, L., & Pratt, R. G. (2004). Efficient waveform inversion and imaging: A strategy for selecting temporal frequencies. *Geophysics*, *69*(1), 231–248. https://doi.org/10.1190/1.1649391.

Socco, L. V., & Strobbia, C. (2004). Surface-wave method for near-surface characterization: A tutorial. *Near Surface Geophysics*, *2*(4), 165–185.

Spakman, W., & Bijwaard, H. (2001). Optimization of cell parameterizations for tomographic inverse problems. *Pure and Applied Geophysics*, *158*(8), 1401–1423. https://doi.org/10.1007/Pl00001227.

Stummer, P., Maurer, H., & Green, A. G. (2004). Experimental design: Electrical resistivity data sets that provide optimum subsurface information. *Geophysics*, *69*(1), 120–139.

Taguchi, G. (1987). *System of experimental design: Engineering methods to optimize quality and minimize costs*. UNIPUB/Kraus International Publications.

Tarantola, A. (1984). Inversion of seismic-reflection data in the acoustic approximation. *Geophysics*, *49*(8), 1259–1266. https://doi.org/10.1190/1.1441754.

Tarantola, A. (1988). Theoretical background for the inversion of seismic waveforms including elasticity and attenuation. *Pure and Applied Geophysics*, *128*(1), 365–399.

Tarantola, A. (2005). *Inverse problem theory and methods for model parameter estimation*. Philadelphia, PA: Society for Industrial and Applied Mathematics.

van Den Berg, J., Curtis, A., & Trampert, J. (2003). Optimal nonlinear Bayesian experimental design: An application to amplitude versus offset experiments. *Geophysical Journal International*, *155*(2), 411–421.

van Leeuwen, T., & Herrmann, F. J. (2013). Fast waveform inversion without source-encoding. *Geophysical Prospecting*, *61*(s1), 10–19.

Vermeer, G. J. (2002). *3-D seismic survey design*. Society of Exploration Geophysicists.

Vermeer, G. J. (2003). 3D seismic survey design optimization. *The Leading Edge*, *22*(10), 934–941.

Virieux, J., & Operto, S. (2009). An overview of full-waveform inversion in exploration geophysics. *Geophysics*, *74*(6), WCC1–WCC26.

Vozoff, K., & Jupp, D. L. B. (1975). Joint inversion of geophysical data. *Geophysical Journal of the Royal Astronomical Society*, *42*(3), 977–991. https://doi.org/10.1111/j.1365-246X.1975.tb06462.x.

Wilkinson, P. B., Meldrum, P. I., Chambers, J. E., Kuras, O., & Ogilvy, R. D. (2006). Improved strategies for the automatic selection of optimized sets of electrical resistivity tomography measurement configurations. *Geophysical Journal International*, *167*(3), 1119–1126.

Wiskin, J., Borup, D., Johnson, S., Andre, M., Greenleaf, J., Parisky, Y., et al. (2013). Three-dimensional nonlinear inverse scattering: Quantitative transmission algorithms, refraction corrected reflection, scanner design and clinical results. *Proceedings of Meetings on Acoustics*, *19*(1). . 075001https://doi.org/10.1121/1.4800267.

Yilmaz, Ö., & Doherty, S. M. (2001). *Seismic data analysis: Processing, inversion, and interpretation of seismic data* (2nd ed.). . Tulsa, OK: Society of Exploration Geophysicists.

Yokota, T., & Matsushima, J. (2003). *Seismic waveform inversion in frequency-space domain: Strategy for the optimal inversion step selection*. *Environmental Rock Engineering* (pp. 299–304). Swets and Zeitlinger.

Zhou, B., & Greenhalgh, S. (2009). On the computation of the Frechet derivatives for seismic waveform inversion in 3D general anisotropic, heterogeneous media. *Geophysics*, *74*(5), Wb153–Wb163. https://doi.org/10.1190/1.3123766.

Zografos, G., Koulocheri, D., Liakou, P., Sofras, M., Hadjiagapis, S., Orme, M., et al. (2013). Novel technology of multimodal ultrasound tomography detects breast lesions. *European Radiology*, *23*(3), 673–683. https://doi.org/10.1007/s00330-012-2659-z.

This page intentionally left blank

CHAPTER TWO

A Review of Airborne Electromagnetic Methods With Focus on Geotechnical and Hydrological Applications From 2007 to 2017

Esben Auken[1], **Tue Boesen, Anders V. Christiansen**
Department of Geoscience, Aarhus University, Aarhus, Denmark
[1]Corresponding author: e-mail address: esben.auken@geo.au.dk

Contents

Abstract

The purpose of this review is to report the major advancements that have been made within the area of airborne electromagnetics (AEM) between 2007 and 2017, with a focus on geotechnical and hydrological applications. Older articles will be listed in order to provide context for recent advancement, or when describing the underlying methodology.

Advances in Geophysics, Volume 58
ISSN 0065-2687
https://doi.org/10.1016/bs.agph.2017.10.002

The review is structured such that each section can be read independently, and each section starts out with a brief introduction to establish a common ground.

References are inserted where relevant, and as such some articles are cited multiple times, since they are relevant in multiple sections.

1. INTRODUCTION

Electromagnetic (EM) methods are among the most important tools we have for exploring the subsurface. Among the geophysical EM methods, no area has seen more advancement within the last decade than airborne EM (AEM) systems and the accompanying interpretation software (interpretation software in this context includes numerical modeling codes). Applications are widespread and they range from regional-scale groundwater studies and mineral exploration to mapping of thin shallow layers or location of unexploded ordnance. AEM methods have been used for groundwater and geotechnical studies for several decades, but lately, worldwide recognition of the importance of the method has increased greatly. One reason for this is the maturity of hardware systems, which are now capable of providing accurate and low-bias data. This can be used in the increasingly sophisticated interpretation software solutions developed within the last decade, which, when combined with high-quality data, have been able to produce impressive results.

Now and in the future the world will face widespread freshwater scarcity, which is starting to be generally acknowledged, and currently AEM methods are the only viable approach to provide mapping solutions to address these problems on a global scale. In light of this, we believe AEM will be a crucial method in the future, and likely the most important investigative method for groundwater management.

The purpose of this review is to give the reader an overview of the AEM area, from a geotechnical and groundwater perspective. The technologies, both hardware and interpretive software, have developed so rapidly that even among scientists and professionals, very few have a complete overview of the state of AEM technologies and their areas of applicability.

Hardware and interpretive software developments are in a symbiotic relationship. However, very few people are experts in both areas and this knowledge gap gives disjointed development to the detriment of both areas, which is something we hope to help mend with this review. Hardware development is as important as software development, and both need to be understood in order to fully utilize the capabilities of the AEM method.

Hand in hand with the development in computer power and AEM hardware, operational 3D modeling and inversion codes for transient EM data now exist, and some even in open source. Thanks to local meshing technologies, 3D codes are capable of handling large surveys in principle. However, the computational demands for modeling a full AEM survey are still so large that only a few companies do this in practice.

2. AEM SYSTEMS—HARDWARE

AEM systems include any airborne system that uses inductive electromagnetics to measure the earth's resistivity. Examples of helicopter transient EM (HTEM) and helicopter frequency EM (HFEM) systems can be seen in Fig. 1. While the systems may look simple, successfully designing such systems has proven quite an engineering challenge.

AEM systems have seen important advancements within the last decade, and with these advancements, more applications have been unlocked. While software development is primarily driven by academics, hardware development is almost exclusively driven by private enterprises. This means that

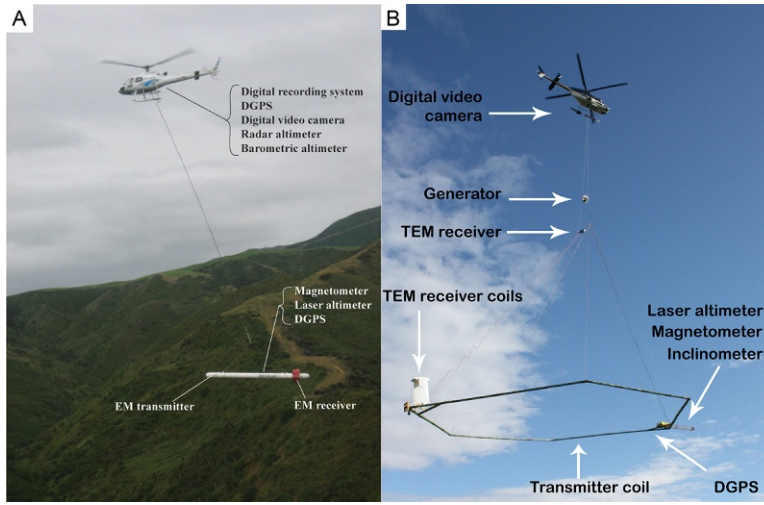

Fig. 1 Examples of helicopter AEM systems. (A) The RESOLVE frequency EM system. (B) A SkyTEM transient EM system. *Panel (A): Ball, L. B., Smith, B. D., Minsley, B. J., Abraham, J. D., Voss, C. I., Astley, B. N., et al. (2011).* Airborne electromagnetic and magnetic geophysical survey data of the Yukon Flats and Fort Wainwright areas, central Alaska, June 2010. *US Geological Survey, ISBN 2331-1258. Panel (B): courtesy of SkyTEM Surveys.*

hardware development is less transparent, and in many cases, information is not readily available in scientific publications, but has to be found on homepages or in conference proceedings.

Traditionally, AEM systems are first categorized as either frequency-domain (FEM) or time-domain systems (TEM), depending on whether they do constant measurements at a few select frequencies (see Fig. 2A), or they fire discrete electromagnetic pulses and measure their decay curves (see Fig. 2B). Historically, airborne FEM (AFEM) systems are considered to have a better resolution in the near surface, but a lower depth of investigation (DOI) compared to airborne TEM (ATEM) systems. Within the last decade, however, the heavy development in ATEM systems has made their near surface resolution sufficiently accurate such that modern ATEM systems are able to resolve the shallow surface as well as AFEM systems.

The last major historical categorization of AEM systems is whether the system is attached to an airplane, called a fixed-wing system, or whether it is attached underneath a helicopter. Fixed-wing systems need to fly fast in order to remain in the air, which can be both a blessing and a curse. High operational speeds are beneficial when the goal is to cover large areas fast and cheaply. Lower operational speeds are beneficial when high-precision measurements are desired. Furthermore, fixed-wing systems generally fly at higher altitudes than helicopter systems due to their limited maneuverability.

In the mid-2000s ATEM systems were the up-and-coming systems, which showed promising characteristics compared to well-established

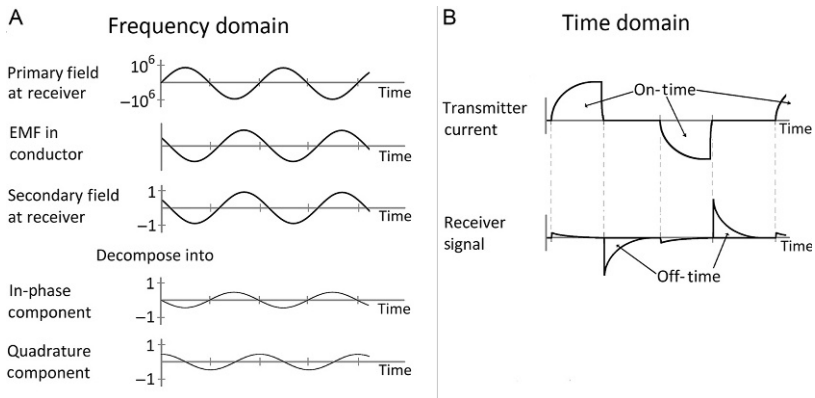

Fig. 2 Schematic representation of FEM and TEM. (A) A frequency-domain system's primary and secondary fields at the receiver. (B) The transmitter current for a time-domain system with square waveform, and the resulting receiver signal.

AFEM systems. However, which system would ultimately prove the de facto standard EM exploration system was yet to be determined. Today, ATEM systems are well established, and most often the method of choice, with powerful system characteristics concerning: DOI, shallow surface resolution, operational speed, and data accuracy.

The ideal AEM system for a given problem depends on the purpose of the survey. Broadly speaking, survey goals can be either detection or mapping. This results in two different types of AEM systems, one system type that focuses on strength/speed and probes the earth as deep/fast as possible, and another system type that focuses on finesse and probes as accurately as possible. However, recent advancements have brought these two separate system types closer together, to the point where there now exist sophisticated systems capable of both deep/fast detection, as well as accurate mapping.

Detection surveys are most commonly used in mineral prospecting. Here AEM has primarily been used as an effective first approach tool for covering large areas. Traditionally, this has been accomplished by using deep probing fixed-wing systems, with the receiver towed behind the aircraft (Smith, 2014). However, since around 2000 the helicopter systems have moved into this area with similar or greater probing capabilities.

Mapping surveys generally require the capability to measure small resistivity contrasts, and hence the focus is less on probing deeply, and more on controlling the system transfer function and the sensor itself. Thus, mapping surveys generally use more sophisticated, but less powerful hardware, which has been employed mostly from helicopter platforms. Typical targets in mapping surveys are low contrast groundwater mapping and geotechnical applications. The helicopter systems for these applications started to appear in the mid-2000s.

The most important factors controlling the shallow resolution of an ATEM system are:

- A rigid or well-determined system, with sufficient magnetic moment to probe the depth of interest.
- A high bandwidth of the system. The bandwidth is set by both the receiver coil and the receiver instrumentation and should be well above 300 kHz.
- The shape of the transmitter waveform, which needs to have a fast turn-off in order to energize the earth with high-frequency energy.
- Unbiased and uncontaminated early- and late-time gates for a good resolution of the shallow geological layers.

2.1 Advancements in the Last Decade

Within the last decade, no AEM system type has seen as much advancement as the helicopter-TEM systems (Legault, 2015), and with these developments the focus has broadened. Systems used to be specialized for a particular field, but today, primarily due to multimoment or multipulse technologies, general systems designed to service as many markets as possible are seen.

2.1.1 Depth of Investigation

DOI is often the main focus in mineral exploration, where the general philosophy is that deeper is better. In groundwater and geotechnical explorations, a large DOI is less important, as long as the signal is strong enough to provide sufficient information at the depth of interest.

DOI depends on many parameters. The most important ones, which can be influenced, are the magnetic moment, the noise level of the receiver system, and the flight altitude.

The magnetic moment is the strength of the signal emitted from the system, and thus in order to achieve deeper DOIs, there has been focus on increasing the moment. Allard (2007) showed how the moment of AEM systems steadily grew from less than 100,000 Am^2 to an excess of 500,000 Am^2, in the period 2000–2007. Within the last decade, the moment has continued to grow, and today the major companies now all present at least one system with a dipole moment in excess of 1000,000 Am^2, and in the case of HELIGEOTEM and MEGATEM the dipole moment has been pushed in excess of 2000,000,000 Am^2 (both of these systems are designed for mineral exploration).

In order to achieve a large DOI, the noise level of the receiver system is also important, even though very little has been published about it. Receiver noise originates from the electronics of the receiver system and from the motion of the receiver coil in the earth's magnetic field. Assuming the electronic noise is at a fixed level, the only way to lift the signal above this noise is by increasing the area of the receiver loop, either by making the area of the loop large, or by adding more turns to the loop. However, the area of the receiver loop usually has to remain rigid and hence small in order to avoid primary field contamination, and thus the choice is often to increase the number of turns in the loop. The drawback of this solution is that increasing the number of turns in the receiver loop decreases the bandwidth of the coil, which results in a poorer shallow layer resolution (Effersø, Auken, & Sørensen, 1999). Alternatively, sophisticated coil suspension systems can be employed in order to reduce the electronic noise (Nyboe & Sørensen, 2012).

2.1.2 Surface Resolution

Achieving a good subsurface resolution is a product of many different components and parameters, which must all be precisely balanced.

Instabilities and uncertainties can lead to smeared or unreliable data. A common way to counteract this is through deconvolution techniques to obtain early-time measurements (Legault, Prikhodko, Dodds, Macnae, & Oldenborger, 2012; Sattel & Battig, 2016). Though deconvolution is commonly used to increase the apparent bandwidth of a system and push the early-gate information, Rasmussen, Nyboe, Mai, and Larsen (2017) demonstrate how deconvolution is not always the best approach for handling the waveform.

Christiansen, Auken, and Viezzoli (2011) show the resulting modeling errors, which would result from various inaccurate system descriptions. The paper highlights the importance of: using low-pass filters, accurately modeling the system geometry, and to include altitude as an inversion parameter. Similar work was performed on frequency-domain systems in Minsley, Kass, Hodges, and Smith (2014) using Monte Carlo methods.

Early-time gates provide the clearest information about the upper layers of the earth. Because of this, the ability to measure as close to the ramp-off as possible is important for groundwater and geotechnical AEM systems.

ATEM receivers are generally not able to measure the earth response before the primary field is completely shut off, since the primary field is many orders of magnitude larger than the secondary earth response. However, the primary signal takes longer to turn-off for large currents, as shown in Fig. 3. Thus, a system can either run with a low current and get a low DOI and early-time gate information, or run with a large current, but then lose the early-time information. This changed when SkyTEM introduced a dual moment system, which allowed both a high DOI, from a high-moment transmitter pulse, and good shallow surface resolution, from a low-moment, fast turn-off transmitter pulse (Sørensen & Auken, 2004). Since then other approaches to achieving similar results have been developed. Prikhodko et al. (2013) use a full-waveform approach in order to retain the high-frequency component of the signal, and Chen, Hodges, and Miles (2014) employ a multipulse approach.

In order to get as early-gate information as possible, the receiver is usually placed in a zero-field position such that the remnant of the primary field has the least influence on the receiver. Broadly speaking, there are three transmitter/receiver configurations employed in HTEM. The first one is to have the receiver placed in the center of the transmitter coil, shielded by a bucking coil. Conceptually, this method provides a desirable symmetry to the system, but in practice this method has some problems since the receiver is placed

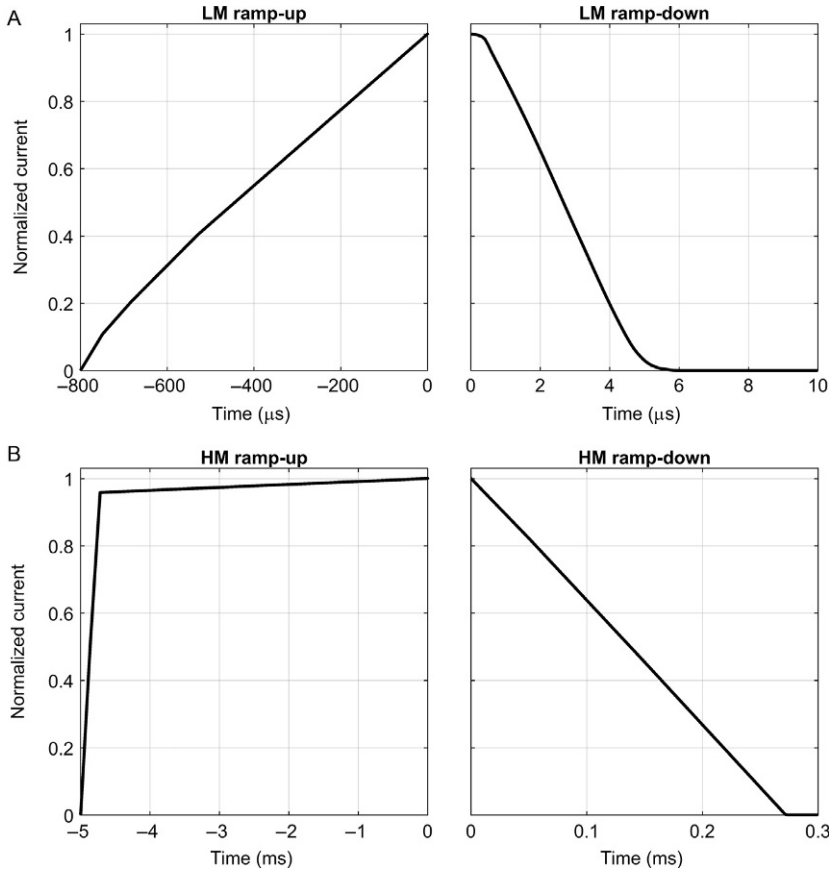

Fig. 3 Turn-on and Turn-off ramps for the new SkyTEM306HP system, presented in Gisselø and Nyboe (2017). (A) The low-moment ramps. (B) The high-moment ramps. Note the difference in timescale between high moment and low moment. *Courtesy of SkyTEM Surveys.*

where the primary field is strongest—neglecting the bucking coil. Due to small movements of the systems as well as geometric inaccuracies, the shielding from the bucking coil is hard to get perfect. This can lead to primary field contamination. The second approach is to place the receiver in a natural off-center zero position. The benefit of this approach is that even if the receiver moves slightly or is placed slightly off the zero position, the field is naturally zero in this position (Auken et al., 2015), and hence small perturbations will give significantly less primary field contamination than in a center loop configuration. The third approach is to place the receiver far offset from the transmitter (Hunkeler et al., 2015). However, this approach

makes accurate system geometry modeling particularly troublesome, since transmitter and receiver are no longer rigidly fixed. The TEMPEST survey system is one system that uses this method (Lane et al., 2000).

Around 2007, the earliest time gates ATEM systems could measure were ~20 μs after beginning of turn-off, which roughly corresponded to the turn-off time of the primary signal. Since then significant improvements have been made to measure earlier times.

As an example of the developments, early SkyTEM systems removed the early-time gates. Instead, in order to push toward earlier times, SkyTEM Surveys developed field compensation schemes. These were built around coil response compensation, where the primary field was measured at a high altitude in order to get free-space primary field response and compensate for that by entering it as a factor in the inversion (Schamper, Auken, & Sørensen, 2014). The second iteration, dubbed primary field compensation, employs the same high-altitude measurement method, but in conjunction with a measurement of the coupling between the transmitter and the receiver. The latest iteration of this measures the full impulse response of the system and employs this directly on the hardware side. This allows data to be measured during the turn-off, and hence gates can start measuring from 0 μs (Andersen, Nyboe, Kirkegaard, Auken, & Christiansen, 2015).

2.2 Current State of AEM Systems

2.2.1 Frequency-Domain Systems

Development of airborne frequency-domain EM (AFEM) systems has been limited within the last 10 years. This is reflected in several ways:

- Legault (2015) reports that of the 70 papers presented at the South African AEM conference in 2013, only two of these papers dealt with frequency-domain systems. A similar count of the 2017 EAGE Near Surface AEM conference revealed 21 abstracts concerning time domain and 6 concerning frequency domain.
- The only notable development that has been made in AFEM systems within the last decade was made by Smiarowski and Macnae (2013), but despite successfully making a new AFEM design, which promised deeper DOI, the system never made it past prototype.

Today, the following general purpose AFEM systems are in operation: RESOLVE, DIGHEM, IMPULSE, and GEM-2A are all HTEM systems, while Sander and GeoTechnologies operate a fixed-wing FEM system, and GeoTechnologies operates the EM-4H system, which can be flown by both helicopter and plane. In addition, the Norwegian Geotechnical Institute

(NGI) has developed a HFEM system specially designed for mapping of sea ice, called MAiSIE. A comparison of all these systems can be found in Table 1.

2.2.2 Time-Domain Systems

There is a vast number of companies maintaining and developing airborne systems, but the three most significant players in the field at the moment are: Geotech, CGG, and SkyTEM Surveys. Geotech's and CGG's initial focus was mineral exploration systems, while SkyTEM's initial focus was groundwater exploration. All the systems have come a long way since then, and all three now have systems capable of both mapping and deep detection, but their initial focus is still apparent in their modern systems. A comparison of their current mapping systems can be seen in Table 2.

According to their webpage, Geotech currently offers three different version of the VTEM system: VTEM, VTEM+, and VTEM^{MAX}. All the systems have an operational speed of 90 km/h, and have the receiver in the center of the transmitter loop. Their smallest system (VTEM) only has a vertical receiver, while the others offer horizontal configurations as well. Traditionally the VTEM systems have been designed with focus on high moment and late time-gate quality for deep mineral exploration. Their VTEM^{MAX} was the first AEM system to detect the Caber North deposit, which is a well-known and notoriously difficult site to detect, since it is buried at a depth of more than 300 m and below a conductive overburden (Killeen, 2013). The VTEM systems are single moment systems, which gives them limited resolution in the upper layers, though the resolution has been significantly improved by including more early-time information (Prikhodko et al., 2013). While the AeroTEM system (Balch, Boyko, & Paterson, 2003) is not listed on Geotech's website, many surveys have been flown using the system in the last decade. The latest development from Geotech was presented at EAGE 2017, where Eadie, Legault, Plastow, Prikhodko, and Tishin (2017) presented the VTEM early time (ET); which focuses on further improving VTEM's early-time capabilities. VTEM ET enables 500 μs ramp-off times, which is roughly three times faster than traditional VTEM systems. Furthermore, the new design increases the receiver bandwidth to allow more early-time information.

Historically, CGG has offered a variety of fixed-wing and helicopter-ATEM systems with a focus on mineral exploration, such as their well-known MEGATEM II, and HELITEM systems. In order to map the shallow near-surface they use a multipulse approach (Chen et al., 2014). CGG

Table 1 A Comparison of the Frequency-Domain Systems Currently Commercially Employed

Frequency-Domain Systems

System name	IMPULSE	DIGHEM V	RESOLVE	GEM-2A	SGFEM	EM-4H	MAiSIE
Company	Geotech	CGG	CGG	Geophex	Sander & Geotechnologies	Geo Technologies	NGI
Method	HEM	HEM	HEM	HEM	Fixed wing	Both	HEM
Frequencies (#)	6	5	6	3	4	4	Broadband
Frequency range (kHz)	0.87–23.0	0.9–56.0	0.4–127.0	0.3–10	0.9–24.5	0.13–8.3	0.5–8
Configuration (Hor/Ver)	3H/3V	3H/2V	1H–5V	3H	4V	4V	H
Coil spacing (m)	6.5	6.3–7.9	7.9–9.0	5.1	21.3	6.5	2.7

Data are extracted from Kirsch, R., Rabbel, W., Ernstson, K., Börner, F., Siemon, B., Christiansen, A. V., et al. (2009). *Groundwater geophysics—A tool for hydrogeology*. Springer; Pfaffhuber, A. A., Hendricks, S., Hunkeler, P., & Kvistedal, Y. (2012). Introducing a new generation multi-sensor airborne system for mapping sea ice cover of polar oceans. *First Break*, *30*; and company websites.

Table 2 A Comparison of Geotech's, CGG's, and SkyTEM's ATEM Systems
Time-Domain Systems, With Accurate Mapping Capabilities From the Three Major Companies

Name	TEMPEST	AeroTEM	VTEM	VTEM+	VTEM^{MAX}	SkyTEM301	SkyTEM304	SkyTEM312Fast	SkyTEM516
Company	CGG	Geotech	Geotech	Geotech	Geotech	SkyTEM	SkyTEM	SkyTEM	SkyTEM
Method	Fixed wing	HEM	HEM	HEM	HEM	HEM	HEM	HEM	HEM
Base freq (Hz)	25	90	30	30	30	325/75	270/22.5	270/30	275/25
Tx area pr turn (m^2)	244	110	240	540	960	341	341	341	536
Tx turns (#)	1	5	4	4	4	1	1/4	2/12	2/16
Waveform	Square	Triangular	Polygonal	Polygonal	Polygonal	Square	Square	Square	Square
Peak current (A)	300	410	250	310	335	6/95	9/110	5/120	3.5/120
Peak moment (kAm^2)	73.2	220	240	625	1300	2/320	2.7/150	3/490	4/1000
Transmitter altitude (m)	120	30	30	30	30	30	30	35	30
Speed (m/s)	65	21	25	25	25	33	33	42	33
Off-time channels (#)	15	17	32	32	32	19/20	22/23	18/20	15/19
Earliest channel (μs)	13	87	21	21	21	4.2	5	9.2	10.2
Receiver component	XYZ	XZ	Z	XYZ	XYZ	XYZ	XYZ	XYZ	XYZ

Information for the TEMPEST system is from Mulè, Miller, Carey, and Lockwood (2012), while information on VTEM and SkyTEM systems are from their respective webpages. SkyTEM's dual moment systems are presented as the values for the low-moment/high-moment system.

also operates the TEMPEST fixed-wing system, which carries a towed receiver bird. The system is described in great detail in Lane et al. (2000). Christiansen, Auken, Ley-Cooper, and Andersen (2016) show that it is possible to get accurate modeling with the TEMPEST system. Their new GRYPHON system combines TDEM, magnetics, gravity gradiometry, laser scanning, and radiometrics into one system (Killeen, 2014).

SkyTEM's original system was designed for groundwater mapping, but has since been upgraded in several ways and is now used in a wide variety of geophysical cases. SkyTEM systems place their receiver in a zero position slightly above and behind the transmitter. Furthermore, SkyTEM introduced the multimoment feature. This allows systems to have both a large DOI and shallow surface resolution. According to SkyTEM's webpage they currently offer services with five different system types: SkyTEM301, SkyTEM304, SkyTEM312, SkyTEM312Fast, and SkyTEM516. The first four systems use the same size frame, while the latter, SkyTEM516, uses a significantly larger frame, which allows it to reach a dipole moment in excess of 1M NIA. This gives them a DOI deep enough to detect and resolve the Caber north deposit. The SkyTEM301, SkyTEM304, and SkyTEM312 are modified versions of essentially the same system, with a slightly different DOI and resolution. SkyTEM312Fast is operated at up to 150 km/h, but is otherwise similar to SkyTEM312. The latest development from SkyTEM was presented at EAGE 2017, where Nyboe and Mai (2017) showed how the receiver bandwidth was considerably increased, and Gisselø and Nyboe (2017) presented the new SkyTEM high-power variants, which are similar to the traditional systems, but have an increased dipole moment, lower weight, and faster ramp-off times.

While these are the leading companies in the field, there exists a variety of other companies with ATEM systems, though the vast majority is focused on mineral exploration. In our opinion the only other system designed for geotechnical and groundwater exploration surveys is the Xcite system, by New Resolution Geophysics of Cape Town, South Africa. This is a rigid inflatable HTEM system (Combrinck & Wright, 2016).

2.3 System Comparison Studies

Over the years there have been a number of tests and comparisons of different AEM systems.

Steuer, Siemon, and Auken (2009) compare a SkyTEM system with a German frequency-domain system (based on the RESOLVE system) on a

survey in Germany, where the geology targets are buried valleys. They conclude that the two systems provide comparable results, though the SkyTEM system of that time is not able to resolve the shallow area, but does provide a deeper DOI.

Abraham et al. (2012) tested the AFEM system RESOLVE and concluded that the system showed excellent stability and great agreement with ground truth. They furthermore concluded that their confidence in HEM systems greatly improved during the course of their study.

A more recent comparison was carried out by Bedrosian, Schamper, and Auken (2016), who compare three different AEM systems over two different test areas in Nebraska, USA. The three systems are SkyTEM304, RESOLVE, and AeroTEM IV. The two test sites are characterized by shallow and deep alluvial aquifer systems. In the comparison they note that the RESOLVE and AeroTEM systems both display some level of coupling bias in the data near power lines; despite processing attempts to remove it, they conclude that the bias is apparent because data stacking is done before processing removes the coupled data. Despite this, they further conclude that all three systems are capable of detecting and discriminating the large-scale aquifer base, though the RESOLVE system is unable to constrain the base of the aquifer below a depth of 60 m due to its shallow DOI. Furthermore, they conclude that AeroTEM IV results show discrepancies at the shallow surface due to their lack of early-time gates. They finally estimate that this is also the reason why the AeroTEM IV system is overestimating the thickness of aquifer. Overall, the SkyTEM304 system corresponds well with the ground truth, but has trouble resolving the top 10 m of the subsurface.

3. SOFTWARE

EM modeling is done in a variety of ways, but most approaches fall within one of four different categories: integral equation or differential equation, in either time domain or frequency domain. Generally, each of the different approaches has strengths and weaknesses.

3.1 Modeling

The following provides an overview of various significant advancements within AEM modeling within the last decade. For additional information on recent advancements in AEM modeling, the reader is referred to the reviews by Börner (2010) and Everett (2012).

3.1.1 1D Modeling

The governing equations resulting from the 1D approximation were developed in the 1980s and are built on the integral formulation of Maxwell's equations (Ward & Hohmann, 1988). 1D modeling is the de facto workhorse when it comes to AEM, and will remain so for a while. The reason for this is that 1D modeling is several orders of magnitude faster than either 2D or 3D modeling, and thus making it an invaluable first approach tool. Advancements made to 1D AEM modeling today are mostly about increasing the computational speed, and system modeling. Kirkegaard, Andersen, Christiansen, Auken, and Boesen (2015) explain how 1D calculations can be vectorized and parallelized. By deviating from the intuitive recursive way of calculating the 1D kernel, it is possible to make an algorithm that is both parallelizable and vectorizable.

Christensen, Reid, and Halkjær (2009) developed a fast 1D approximate method, which uses an iterative process to calculate an apparent earth conductivity. Christensen (2016a) refines this method by choosing an optimal starting guess for the apparent conductivity, which significantly speeds up the approximation as well as making it more accurate. The refined method claims an impressive speedup of 50 times compared to the normal 1D approximation, while keeping the additional modeling error below 1%.

3.1.2 2D Modeling

The 2D approximation used in AEM assumes a 2D earth and a 3D source, and is commonly referred to as the 2.5D formulation (Stoyer & Greenfield, 1976). The 2.5D approximation resembles situations encountered in AEM, but is less commonly used because of its considerable computational burden due to the expensive inverse Fourier transformation.

The most common method is to split the total field into a primary and secondary field. The reason for doing this is that the discretization will inevitably introduce a small error, so rather than introducing this error on the total field, which is several orders of magnitude larger than the secondary field of interest, the primary field is calculated analytically, and the error is only introduced on the secondary field. Li et al. (2016) use this approach in conjunction with a finite element mesh and operate in the frequency domain. Their code uses a damped least square inversion algorithm based on the single value decomposition principle. Yu and Haber (2012) use a finite volume approach in frequency domain, with a limited-BFGS inversion algorithm. Vöge et al. (2015) use 2D modeling to model sea-ice thickness with a finite element code operating in frequency domain.

Their code was extended in Boesen et al. (2017) to include local meshing, and optimized in several ways, to enable accurate modeling of much larger surveys.

3.1.3 3D Modeling

With the increase in computer power, 3D modeling and inversion have become feasible, and several research groups are now actively developing various kinds of 3D codes. The group at University of British Columbia has two separate code repositories, capable of doing full 3D modeling and inversion. Their newest code is built in the new high-performance scientific programming language Julia (Bezanson, Karpinski, Shah, & Edelman, 2012). The code is open source and is built on a general partial differential equation solving framework called jInv (Ruthotto, Treister, & Haber, 2016). jInv currently supports both finite difference and finite volume meshing, as well as adaptive octree meshing. The 3D EM modules built upon this framework can handle 3D simulations using both the frequency- and time-domain approach and are described in Haber and Schwarzbach (2014). The other 3D open-source code is built in python and is called SimPEG (Cockett, Kang, Heagy, Pidlisecky, & Oldenburg, 2015). SimPEG is a general purpose inversion framework, capable, among other things, of doing 3D EM simulations, as demonstrated in Heagy, Cockett, Kang, Rosenkjaer, and Oldenburg (2016). SimPEG is not designed for large surveys, but rather for academic studies as well as educational purposes.

Börner, Ernst, and Spitzer (2008) have built a 3D forward modeling code with a finite element mesh. The code operates in the frequency domain by projecting the Helmholtz equation onto a Krylov subspace using the Arnoldi process. The transformation back to time domain is handled through a Hankel transform. The code was later expanded to include time-domain propagation as detailed in Börner, Ernst, and Güttel (2015), which they argue is generally computationally superior.

Mulder (2008) has built a 3D frequency domain forward modeling code using the multigrid method with a generalized finite volume mesh. He concludes that multigrid methods perform excellently when used with a constant grid spacing, but have a less than satisfactory performance when used on stretched cells.

Cox, Wilson, and Zhdanov (2010) introduced the moving footprint approach, which allowed them to handle much larger surveys than would otherwise be possible. They used it in conjunction with a 3D integral

equation scheme, which allowed them to present a full 3D modeling and inversion code, capable of handling large surveys. The code was originally only able to handle frequency-domain systems, but was later upgraded to also handle time domain, as detailed in Cox, Wilson, and Zhdanov (2012). While integral equation approaches generally have trouble with large conductivity contrasts, their code showed some promising results on field data as seen in Wilson, Cox, Čuma, and Zhdanov (2012), though data misfits were not shown.

Yin, Qi, and Liu (2016) have created a 3D code that uses the finite element approach and allows electrical anisotropy to be included in their modeling. This opens the possibility for more accurate modeling of distinct dipping stratifications, which are commonly found in mineral explorations or faults. They model their system in the time domain.

Ansari, Farquharson, and MacLachlan (2017) demonstrate a 3D modeling code, using a gauged finite element potential. The code simulates both the inductive and galvanic part of the EM field using edge-based finite elements. Because of the edge-based finite elements, the code is subject to numerical leakage, which does contaminate the models. Despite this, they showed that the code is capable of modeling the Ovoid ore deposit at Voisey's Bay, Canada.

Cai et al. (2017) demonstrate a 3D modeling code, using edge-based finite elements, and a hybrid boundary condition. Their approach uses implicit time propagation and is demonstrated on synthetic data.

3.1.4 Induced Polarization and Superparamagnetic Effects

Converting resistivity to geology can be difficult, since it is well known that different materials can exhibit similar resistivities. Induced polarization (IP) can help alleviate this problem by introducing more parameters to distinguish subsurface materials. Not only can IP modeling help distinguish subsurface materials, but IP effects can also be a major issue if not included in areas with strong IP effects, since these can disturb the other modeling parameters. IP occurs when a material is capable of retaining a charge for a significant amount of time after being subjected to an electromagnetic field. The two main mechanisms that cause IP effects are membrane and electrode polarization (Kratzer, 2013). IP has been studied for decades, using grounded electrodes, despite these having been observed frequently in airborne surveys (Kang & Oldenburg, 2015; Smith & Klein, 1996; Weidelt, 1982).

Superparamagnetic effects are similar to those of IP in many ways. They are both late time effects that significantly disturb the data and the resulting model if not properly accounted for, but the driving mechanism for superparamagnetic effects is completely different from that of IP. Superparamagnetic effects are caused by small para- or ferromagnetic particles, which because of their small size have the freedom to flip their magnetic field randomly. Given enough superparamagnetic material, this flipping gives rise to a significant magnetic signal which appears similar to the discharge of a large buried conductor (Kratzer, 2013).

Several cases of superparamagnetic effects have been studied recently. Kratzer, Macnae, and Mutton (2013) studied the effect of SPM and conclude that by using a uniform SPM time constant distribution of t^{-1}, they are able to model the SPM effects in the field examples shown. Sattel and Mutton (2014) modeled SPM effects using a Chikazumi susceptibility model (Chikazumi & Graham, 2009), and they furthermore suggest several ways to reduce SPM effects. Macnae (2016b) develops a model for fitting both IP and SPM effects simultaneously, using a Cole–Cole model for the IP effect. Note that the IP and SPM effect produce similar signals, but with opposite signs, and can thus be distinguished. The effectiveness of this method is demonstrated in both Macnae (2016a) and Hine and Macnae (2016).

The latest significant development on SPM is from Bournas et al. (2017), where an innovative dual receiver EM system is used for attenuating SPM effects (see Fig. 4). Furthermore, SPM effects are predicted using a pattern recognition effect based on supervised classification.

Marchant, Haber, and Oldenburg (2012) use a 3D method, with an approximate IP current, and showed that it was possible to measure pure IP signals in airborne systems by combining data collected at two frequencies. Furthermore, it was shown that the IP signal could be inverted, and the 3D subsurface chargeability recovered. Marchant, Haber, and Oldenburg (2014) extended the method into time domain. In Marchant (2015) the work is finalized, and it is concluded that while it is possible to do inductive source IP, there is still significant work left before this approach can be used in practice. Following this, Kang and Oldenburg (2016) built on the experiences gathered in Marchant (2015), and made a new three-step method for approximating the IP effect.

The latest development in airborne IP comes with the two papers by Viezzoli, Kaminskiy, and Fiandaca (2017) and Kaminski and Viezzoli (2017), in which airborne IP effects are included in 1D modeling. This method, unlike the previous one, does not try to decouple the IP signal from

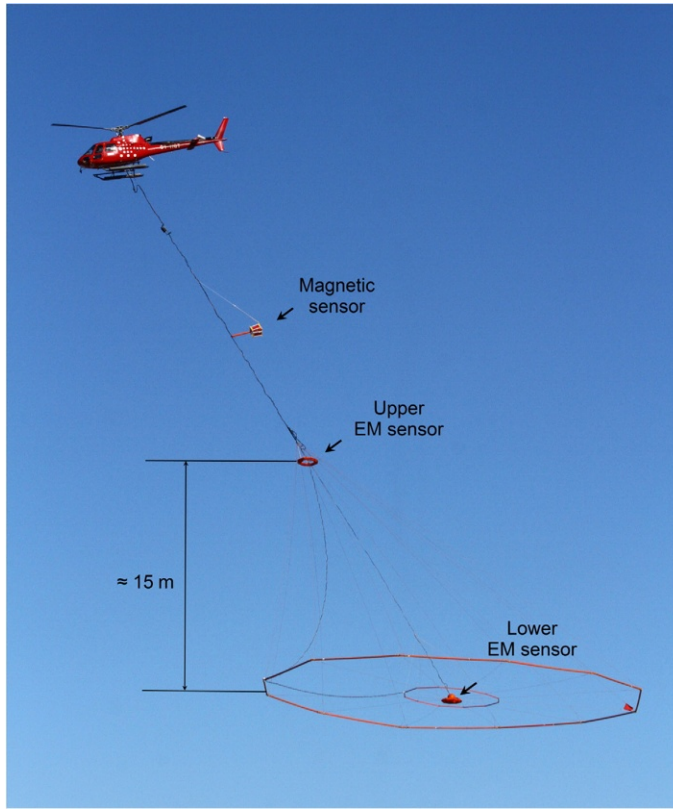

Fig. 4 A dual-receiver EM system, with a lower and upper EM receiver. *From Bournas, N., Taylor, S., Prikhodko, A., Plastow, G., Kwan, K., Legault, J., et al. (2017). Superparamagnetic effects discrimination in VTEM data of Greenland using multiple criteria and predictive approaches.* Journal of Applied Geophysics, 145, *59–73 (courtesy of Elsevier).*

the EM signal, but rather treats everything together. While it is theoretically possible to extend their method to the full 3D modeling case, it is not a trivial extension. The method is successfully tested on field data with convincing results.

3.2 Inversion

In the following section, the various inversion techniques commonly used today will be presented. We have tried to summarize and modularize what is needed, in order to do an inversion, as well as provide the latest advancements within each area. For additional information about recent development in inversion, Chang-Chun et al. (2015) have written a review of airborne inversion.

Apart from imaging techniques, which strictly speaking do not perform an inversion, most other inversion techniques are done by defining an objective function, and thus turning the inversion problem into a minimization problem. In general a minimization needs: an objective function to minimize, a minimization scheme, and a forward modeling method.

3.2.1 Objective Functions

Objective functions quantify the goal of an inversion. In the literature, people use various objective functions, but most of the objective functions can be written in the following general form:

$$q = q_{obs} + q_r, \tag{1}$$

where q_{obs} gives the misfit between model data and observed data, and q_r gives the regularization misfit, which contains any prior information, as well as roughness constraints. In matrix form the misfits can generally be written as (Oldenburg & Li, 2005):

$$q_{obs} = N_d^{-1} \delta \boldsymbol{d}^T \boldsymbol{W}_{obs}^T \boldsymbol{C}_{obs}^{-1} \boldsymbol{W}_{obs} \delta \boldsymbol{d}, \tag{2}$$

$$q_r = N_r^{-1} \delta \boldsymbol{m}^T \boldsymbol{R}^T \boldsymbol{W}_r^T \boldsymbol{C}_r^{-1} \boldsymbol{W}_r \boldsymbol{R} \delta \boldsymbol{m}, \tag{3}$$

where N_d is a normalization to the number of data points, while N_r is a normalization to the number of regularizations used, $\delta \boldsymbol{d}$ is the misfit of the forward response, $\delta \boldsymbol{m}$ is the variation in the model vector, $\boldsymbol{W}_i$ is a weight matrix, $\boldsymbol{C}_i$ is a covariance matrix, and $\boldsymbol{R}_i$ is a roughness matrix, detailing which model parameters are bound together. The weight matrix determines the normalization scheme and is commonly chosen as: a minimization of the squared differences between observed and forward data, L_2 (Constable, Parker, & Constable, 1987); absolute differences, L_1 (Farquharson & Oldenburg, 1998); or schemes favoring more blocky models like sharp SCI (Vignoli, Fiandaca, Christiansen, Kirkegaard, & Auken, 2015).

While most objective functions can be described using Eqs. (1)–(3), there are exceptions. Abubakar, Habashy, Druskin, Knizhnerman, and Alumbaugh (2008) use a multiplicative objective function, with L_2 norm. One advantage of using a multiplicative objective function is that they avoid the ad hoc specification of balance between the different misfit terms. Their regularization term can be chosen to either favor smooth or blocky conductivity models.

3.2.2 Minimization Schemes

In the following we go through different minimization schemes. The most common one for 1D modeling are quasi-Gauss–Newton schemes, while for 2D/3D modeling the most common are BFGS schemes. For the sake of brevity, the schemes are presented without regularization constraints.

3.2.2.1 Gradient Descent

The simplest scheme is the gradient descent scheme, where the model update, $\boldsymbol{m}_{n+1}$, is given as (Saad, 2003):

$$\boldsymbol{m}_{n+1} = \boldsymbol{m}_n + \gamma_n \nabla(\delta \boldsymbol{d}_n), \tag{4}$$

with γ being a line search length.

Conceptually, the method follows the gradient toward a local minima. While convergence to a local minima is assured, the convergence rate is usually low near the local minima, and as such other methods are generally considered superior (Press, Teukolsky, Vetterling, & Flannery, 1992).

3.2.2.2 Quasi-Gauss–Newton

Tikhonov regularization methods are the most commonly used in geophysical EM and are often combined with a Gauss–Newton minimization (Oldenburg & Li, 2005):

$$\boldsymbol{m}_{n+1} = \boldsymbol{m}_n + \left(\boldsymbol{G}_n^T \boldsymbol{C}_n \boldsymbol{G}_n + \boldsymbol{\Gamma}^T \boldsymbol{\Gamma}\right)^{-1} \boldsymbol{G}_n^T \boldsymbol{C}_n^{-1} \delta \boldsymbol{d}_n, \tag{5}$$

where $\boldsymbol{G}$ is the Jacobian and $\boldsymbol{\Gamma}$ is known as the Tikhonov matrix.

A particular interesting special case comes from setting the Tikhonov matrix to a scaled identity matrix. In that case the Levenberg–Marquardt method arises, which combines gradient descent with the Gauss–Newton method, in an effort to get the best convergence rate from both methods. The Levenberg–Marquardt model update is given as (Menke, 1989):

$$\boldsymbol{m}_{n+1} = \boldsymbol{m}_n + \left(\boldsymbol{G}_n^T \boldsymbol{C}_n \boldsymbol{G}_n + \lambda_n \boldsymbol{I}\right)^{-1} \boldsymbol{G}_n^T \boldsymbol{C}_n^{-1} \delta \boldsymbol{d}_n, \tag{6}$$

where λ is a tuning parameter, which determines the amount of influence the gradient descent and the Gauss–Newton method have on the current step. Levenberg–Marquadt or other similar methods give reasonable convergence and are often used, though the cost of computing the Jacobian can be very high and make other methods more attractive.

3.2.2.3 Nonlinear Conjugate Gradient

The nonlinear conjugate gradient method (Hestenes & Stiefel, 1952), and a nonlinear biconjugate gradient method for complex matrices (Van der Vorst, 1992) are popular minimization methods, which perform a Gram–Smith-like orthonormalization search toward a local minima. Nonlinear conjugate gradient methods are typically combined with a preconditioner in order to speed up the process of convergence.

3.2.2.4 BFGS/Limited-BFGS

BFGS and especially limited-BFGS methods are among the most successful, when it comes to quasi-Newton methods—that is, methods that use an approximation to compute either the Jacobian or the Hessian. Quasi-Newton methods are especially relevant for full 3D inversions, where calculating the Jacobian is often extremely expensive. The usability of the BFGS methods stands or falls with its convergence rate. Convergence rates of iterative methods appear to be highly problem dependent and difficult to pin down. Lewis and Overton (2013) offer a nice overview of the potential of BFGS methods and believe it should be possible to determine a class of problems for which the BFGS methods will have a good convergence rate, but so far no such classification has been successfully made. Nash and Nocedal (1991) give a convergence comparison between nonlinear conjugate gradient methods, Gauss–Newton methods, and BFGS methods. They conclude that the convergence rate of BFGS methods is comparable or slightly better than the others. On the other hand Haber (2004) reports unsatisfactory convergence rates using pure limited-BFGS methods on EM problems, and instead suggests using BFGS methods as a preconditioner for other inversion schemes as detailed in Haber, Oldenburg, and Shekhtman (2007).

3.2.2.5 Monte Carlo

Finally, there are various Monte Carlo (MC) methods, which rely on an element of randomness to perform an inversion. The strength of MC methods is that they enable the code to find the global minimum, whereas all the other methods only lead to a local minimum, and thus MC methods are less dependent on the starting model. Furthermore, MC methods provide full parameter estimation information, as exemplified in Fig. 5. Finally, it is possible to create MC methods that do not require calculations of the Jacobian or Hessian, though such methods are rarely favorable. The downside to all this is that MC-based inversions typically require 1000–1000,000s of

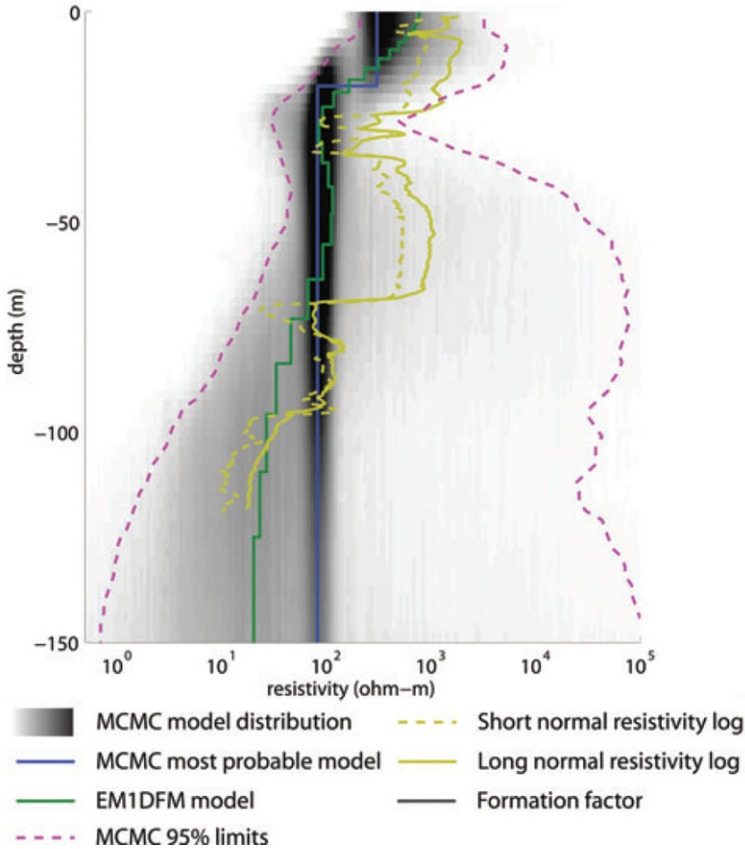

Fig. 5 Distribution of MCMC models. *Modified from Minsley, B. J. (2011). A trans-dimensional Bayesian Markov chain Monte Carlo algorithm for model assessment using frequency-domain electromagnetic data.* Geophysical Journal International*, 187, 252–272 (courtesy of Oxford University Press).*

forward computations. Thus, the total cost of performing an MC inversion is inevitably high, and as such they are often only used as a benchmark tool. While many approaches to MC inversion exist, the dominating algorithm in AEM seems to be the Metropolis–Hastings Monte Carlo (MHMC) algorithm, which is a special case of Markov chain Monte Carlo simulations.

Minsley (2011) presented a MHMC inversion method for airborne frequency-domain data, which is used successfully to model permafrost thaw in Minsley, Wellman, Walvoord, and Revil (2015).

Brodie and Sambridge (2012) and Brodie and Richardson (2013) have also presented a MHMC inversion code, which was originally designed for seismic tomography, but has been redesigned for AEM use. They

primarily use the code for testing parameter resolvability, but note that the method can be used to invert full flight lines at a reasonable cost.

Another MC approach is referred to as simulated annealing, which is an adaptation of the MHMC method, with roots in thermodynamic modeling, and based on the Boltzmann cooling principle. Yin and Hodges (2007) demonstrate the use of simulated annealing on synthetic data, see Fig. 6, and with a field example. They use an objective function with no traditional regularization, and instead rely on the Boltzmann cooling to handle the regularization. Their approach is demonstrated successfully on inversions of two- and three-layer models.

3.2.3 Regularizations

In 1D inversions, regularizations are crucial, since they are the only thing connecting the various soundings internally and externally, and thus the only thing imposing any semblance of continuity into the inversion model. In higher dimensional modeling, regularizations are less critical since inversions generally contain intersounding information through the Jacobian. Even then, regularizations are generally used for all inversions, due to their stabilizing effect on what is otherwise an ill-conditioned problem, as clearly demonstrated by Ley-Cooper et al. (2014), in which the following inversion codes are compared on the same survey: EMFlow (Macnae, King, Stolz, Osmakoff, & Blaha, 1998), GA-LEI (Brodie, 2012), AarhusInv (Auken et al., 2014), a 2D code from Guillemoteau, Sailhac, and Béhaegel (2011), and Cox et al. (2010) 3D inversion code.

Auken and Christiansen (2004) introduced laterally constrained inversion (LCI), which is used with 1D modeling codes, to create a quasi-2D inversion, by including lateral regularization. The usabilities and limitations of this method were later examined using synthetic studies in Auken, Christiansen, Jacobsen, and Sørensen (2008), and on field data in Ley-Cooper, Macnae, and Viezzoli (2010) and Siemon, Auken, and Christiansen (2009), and it was found that the LCI method introduced a significant advancement compared to single-site or stitched-together inversions on both field data and in synthetic studies. Another similar approach dubbed lateral parameter correlation (LPC) was developed by Christensen and Tølbøll (2009). In this approach the models are first inverted individually without any constraints. Next, a laterally smooth version of the models is found by solving a linear equation. Finally, a covariance analysis of the constrained and unconstrained model parameters is performed and is the basis for a third and final inversion. LPC

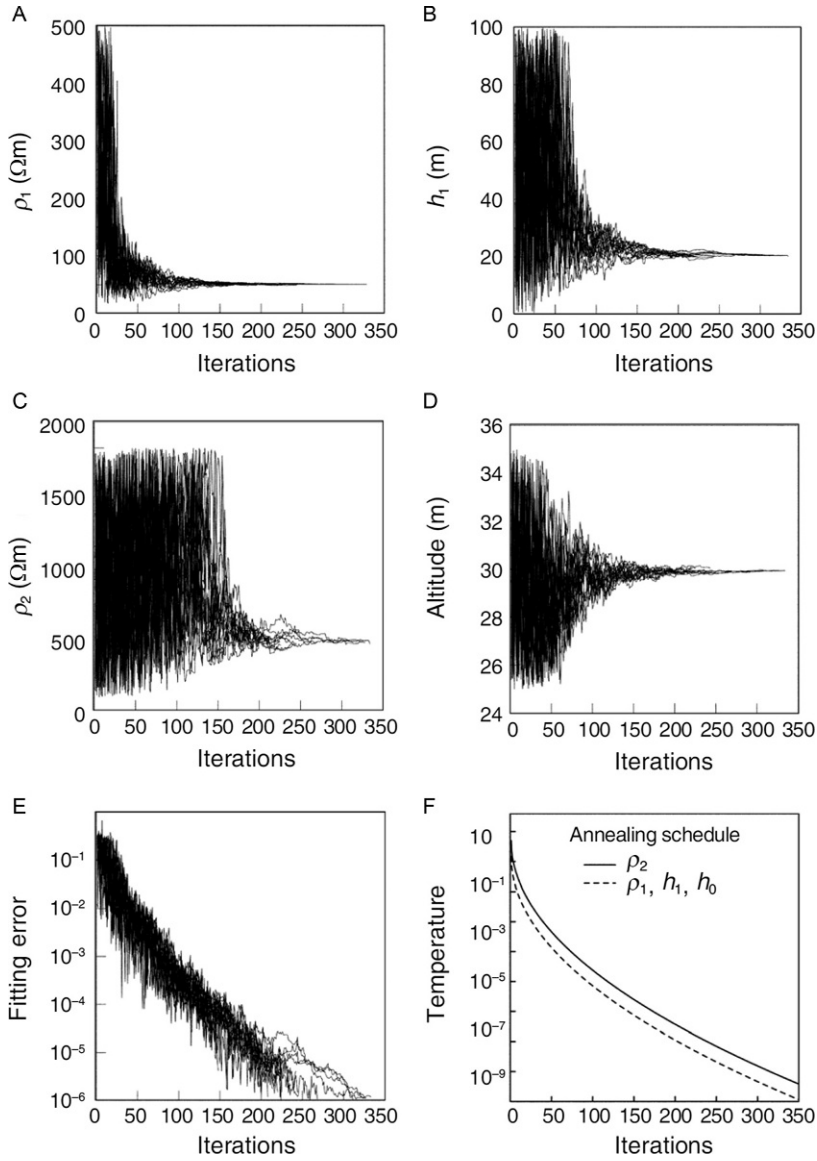

Fig. 6 Simulated annealing for a two-layer model. (A–D) The resistivities, thickness, and altitude as a function of iterations. (E) The resulting data residual, while (F) the exponential cooling scheme employed to slowly freeze the variables to a minima (h_0 is the altitude). *From Yin, C., & Hodges, G. (2007). Simulated annealing for airborne EM inversion.* Geophysics*, 72, F189–F195. https://doi.org/10.1190/1.2736195.*

had some initial trouble with topography, which introduced artifacts; however, these artifacts are removed in the extension presented in Christensen (2016b).

Viezzoli, Christiansen, Auken, and Sørensen (2008) introduce spatially constrained inversion (SCI), which extends the LCI regularization to a quasi-3D inversion, by finding the nearest neighbors—not just along flight lines, but also across. This is done by using a Delaunay triangulation on the soundings of the whole survey. In order to be able to handle large surveys, while preserving continuity, the SCI method initially required two inversions to be run. However, this was changed in Kirkegaard and Auken (2015), where various optimization techniques for the SCI methods are explained. After implementing the optimizations, they demonstrate that SCI inversion scales linearly, in both memory and time consumption with survey size.

While regularization schemes like LCI and SCI help bring a sense of continuity to an inversion, such a trait is not always desirable. In mineral deposits, for instance, the conductivity structure will often have sharp discontinuities. In order to correctly model such structures, Vignoli et al. (2015) introduce sharp inversions, which still retain the regularization, but have a max cost to conductivity contrasts, which means that small conductivity contrasts will still be constrained much like in the LCI and SCI case, while large conductivity contrasts will no longer incur a huge regularization cost. Thus continuity is still enforced for small conductivity contrasts, while at the same time enabling the freedom to have large conductivity contrasts.

The holistic approach is designed to wrap processing, and inversion, into one automatic process, and thus avoid multistage error propagation through the standard sequential processing approach. Brodie and Sambridge (2009b), which is an extension of the well-known holistic code presented in Brodie and Sambridge (2006), use an objective function similar to Eq. 1, with the regularization containing a channel bias roughness term, which is included in an attempt to shift some of the work normally done in processing, to inversion. The code operates in the frequency domain and uses 1D forward responses. In Brodie and Sambridge (2009b) a large survey example, with $\sim$8 million data points and a corresponding $\sim$3.4 million model parameters, is successfully inverted. Brodie and Sambridge (2009a) extend the method to transient systems.

Christensen, Ferre, Fiandaca, and Christensen (2017) presented a Voxel inversion, which decouples the inversion model parameters from the soundings. This enables multiple datasets to be combined in a true joint inversion with constraints. In their example, they combine a geophysical inversion of

AEM data with a hydrological inversion of hydraulic conductivity fields, where the link between hydrological parameters and resistivity parameters is given through a spatially varying petrophysical relationship.

Finally, Lelièvre, Oldenburg, and Williams (2009) should be mentioned, since they integrate geological and geophysical data through advanced constrained inversions. While we believe a more likely approach to combining geological and geophysical data is through machine learning after the inversion, this is certainly an interesting approach, which warrants further investigation.

3.2.4 Local Mesh

In AEM, surveys commonly reach sizes too large for an all-at-once modeling and inversion (in 2D and 3D), as proposed in Haber, Ascher, and Oldenburg (2004). In order to counteract this, local meshing was created. Local meshing relies on the assumption that any sounding has a finite sensitivity range. Thus anything further away from the sounding than this range can reasonably be assumed to be negligible. For additional information on sensitivity functions, Christensen et al. (2017) have investigated sensitivity functions in 1D, 2D, and 3D and show how they deviate from each other.

Cox et al. (2010) introduced the concept of moving footprints, which utilize the finite sensitivity range of any EM system to reduce the number of interactions that need to be computed significantly. This enabled them to perform 3D modeling and inversion of surveys larger than anything previously done, though the quality of their inversion results was disputed by Viezzoli, Munday, Auken, and Christiansen (2010).

Another local meshing approach is developed in Yang and Oldenburg (2012a) and Yang, Oldenburg, and Haber (2014), and expanded to octree meshes in Haber and Schwarzbach (2014). Their implementation involves a global mesh, and a local mesh for each sounding (see Fig. 7). While the forward problem is handled on the local meshes, the inversion is made by randomly subsampling the global mesh; this way they make the inversion more

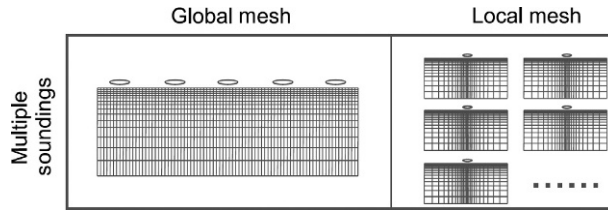

Fig. 7 Local meshing, as implemented in Yang et al. (2014). *Courtesy of Oxford University Press.*

manageable, while remedying overfitting, which can often be a problem in inversions.

Boesen et al. (2017) introduced a local mesh for 2D modeling, which groups soundings in optimized bundles, where the size of a group depends on whether forward or derivative calculations are performed. Each group has an overlap with its neighboring group in order to preserve inline information.

Caudillo-Mata, Haber, Heagy, and Schwarzbach (2016) have provided a general mathematical framework for upscaling, and while the primary ramifications of this work are related to multigrid methods, it is also significant for local meshing, since the method introduces an optimal framework for interpolation between the local and global meshes.

3.2.5 Hybrid Schemes

Conceptually, a hybrid inversion is a multistage process, in which the early stages rely on some inexpensive approximate calculations, which are then, either gradually or abruptly, shifted toward more accurate and computationally expensive calculations at a later stage. By employing this method, less iterations of the more accurate and computationally expensive calculations are needed, at the cost of more iterations of lower accuracy calculations, with the overall effect of lowering the total computational time.

Yang and Oldenburg (2012b) presented a 3D multimesh approach, where they start off by using a coarse mesh, and as the inversion gets closer to convergence the mesh is refined to allow more accurate calculations.

Christiansen, Auken, Kirkegaard, Schamper, and Vignoli (2016) have presented a hybrid scheme, where an approximation is introduced in the early iterations during the calculations of the 1D derivatives. This makes the 1D derivatives less accurate; however, as they note in the paper this has minimal effect on the actual inversion as long as the forward modeling is done accurately. Nearing the end of the inversion, the code switches back to accurate derivatives in order to reach comparable levels of misfit as in the traditional approach. The result of this hybrid approach is a speedup factor $\sim 3-7x$.

Boesen et al. (2017) have created a hybrid 1D/2D scheme with three stages. In the first stage, 1D forward and derivatives are employed. In the second stage, 2D forward and 1D derivatives are employed. In the third and final stage, 2D forward and derivative calculations are used. This approach gives models, which are comparable to a full 2D inversion, but computed $\sim$2–6x faster.

3.3 Other Advances

3.3.1 Automated Processes

Geophysical EM methods are generally quite involved, meaning that once data have been recorded, they need to be processed, a modeling and inversion scheme needs to be chosen, and finally the resulting model needs to be geologically interpreted. Each step requires time and introduces subjectivity into the data. In an ideal world all these choices and processes would be automated, thus saving time and removing subjectivity from the data analysis. This section looks at various advancements toward this goal.

The dual papers by Ullmann et al. (2016) and Scheunert et al. (2016) introduce the cut-and-paste approach. This seeks to automate the process of running 1D inversions on a large survey, and then if necessary selecting parts of this survey for more advanced 3D inversions. Their approach employs image processing algorithms to identify regions which need higher dimensional inversion. After the 3D inversions are performed the 3D models are recast and reintegrated into the 1D models. In the papers both a successful synthetic study and a field example are shown. Their current implementation works on frequency-domain data.

Reninger, Martelet, Deparis, Perrin, and Chen (2011) use singular value decomposition in order to perform a user-assisted denoising of airborne TEM data and reduce processing time and subjectivity. Andersen, Kirkegaard, Foged, Christiansen, and Auken (2016) use a neural network to automate the processing task, and they conclude that while the method is able to reduce the processing time by more than 50%, the neural network is locally dependent and thus needs to be trained on a subset of each individual survey before being useful. Friedel, Esfahani, and Iwashita (2016) use another machine learning technique called self-organizing map, which is an unsupervised machine learning technique. They use this method to automate the geological interpretation of inversion models in near real time. To train their algorithm they use airborne frequency-domain EM data, along with inverted resistivity profiles, geophysical borehole data, and hydrogeological data.

3.3.2 Optimizations

AEM surveys can reach huge sizes with millions of datasets and millions of model parameters, where modeling and inversion on such surveys can be a very computationally demanding task—even in 1D, but especially for 2D or 3D. As such, it is paramount that the codes used are as fast and efficient as

possible. Toward this end there have been several significant advances in the last decade.

3.3.2.1 Parallelism

Since the advancement of computer clock frequency stalled with the introduction of the multicore CPU in 2005, the theoretical performance of processors has continued to follow Moore's law and increase with the same exponential rate as before, but in a fundamentally different way. Performance advancements in modern hardware no longer automatically translate into a performance increase for software. In order to utilize the increase in computational power within the last decade, software has to be specifically written to account for it. The modern scientist has to design his code carefully to not only make use of multiple cores but also to extract additional parallelism in the form of vectorization. Kirkegaard and Auken (2015) describe in great detail how they parallelized a 1D code, while Kirkegaard et al. (2015) show how vectorization and parallelization can be employed in 1D modeling to achieve a speedup of more than an order of magnitude using modern hardware. Another paper that goes into great details in designing EM codes optimized for parallelization is Haber and Schwarzbach (2014), where the focus is on cluster parallelization of the 3D EM problem.

3.3.2.2 Sparse Linear Solvers

Solving sparse linear systems efficiently is, for most modeling and inversion schemes, of vital importance. The linear systems in AEM can reach millions of equations and unknowns, which makes solving them efficiently a nontrivial issue. The methods for solving sparse linear systems are generally split in two categories: direct solvers and iterative solvers. While favor seems to have shifted toward direct solvers within the last decade, both methods have their strengths and weaknesses.

Direct solvers do a full factorization of the system matrix, which can take quite a while and use a lot of memory. However, once such a factorization is done, the system can efficiently be solved for any number of right-hand sides. For direct solvers a number of readymade libraries exist. This makes using direct solvers relatively straightforward. Amestoy, Duff, L'Excellent, and Koster (2001) introduced the direct solver named MUMPS, which is fully parallelized using the MPI interface, which makes it capable of operating in parallel on a cluster. Schenk, Gärtner, and Fichtner (2000) introduced the direct solver used in the Pardiso library, which is parallelized

using the OpenMP interface, and thus making it capable of running in parallel on a single computer. MUMPS and Pardiso are currently the two state-of-the-art direct solvers, and which one you should employ depends on the level of parallelization you wish. A slightly outdated comparison of direct solvers can be found in Gould, Scott, and Hu (2007), while a more modern comparison can be found in Puzyrev, Koric, and Wilkin (2016). Their main conclusion is that the applicability and scalability of direct solvers have risen significantly and are nearing the theoretical limits. That being said, the biggest problem with direct solvers is still the fact that they are not efficient at handling very large linear systems. This is because even though the system matrix might be extremely sparse, there is no guarantee that the factorization matrix will remain sparse.

Iterative solvers, on the other hand, use either no factorization, or at most a partial factorization, followed by multiple forward and backward substitutions, in order to iteratively find a solution to the linear system. Unlike direct solvers, there exists no efficient and ready to use library for iterative solvers. The main reason for this is probably the existence of many different algorithms, and which one is superior is heavily system dependent. Saad (2003) contains all the most common algorithms used for iteratively solving sparse linear systems. Oldenburg, Haber, and Shekhtman (2012) compare the use of direct and iterative solvers for the case of 3D modeling and conclude that direct solvers are favorable for these kinds of problems. While this might indeed be the case, our personal experience with iterative solvers suggests that the computational times shown in Oldenburg et al. (2012) for iterative solvers can be improved significantly by applying more optimal preconditioners, and thus the question of which method is superior remains.

Kirkegaard and Auken (2015) describe the iterative linear solver they use for 1D problems in great detail. Their solver consists of applying the reverse Cuthill–Mckee reordering algorithm (Cuthill & McKee, 1969), followed by a biconjugate gradient-stabilized algorithm, used in conjunction with an incomplete Cholesky factorization as preconditioner.

3.3.2.3 Multigrid Methods

The idea behind multigrid methods stems from the fact that convergence on fine grids tends to stall after a few iterations. In fact, for many iterative methods, the number of iterations needed to reach convergence is proportional to the number of nodes in a direction. A simple way of making sense of this is that during a convergence process, each iteration only allows

information to travel from nodes to their neighbors. This, combined with the fact that reaching convergence generally requires information to be passed from one end of the grid to the other several times, explains the slow convergence. In an attempt to rectify this issue, multigrid methods use coarse meshes in conjunction with the normal mesh (see Fig. 8). These coarse meshes allow information to be passed much further, and thus convergence can be reached much faster.

While multigrid methods have great potential for providing speedups, they also bring several issues that need to be addressed. First the nontrivial nullspace of the curl–curl operator needs to be dealt with in order for multigrid methods to be used in EM. Another issue is that multigrid methods are dauntingly difficult to implement and require interpolation schemes to downsample and upscale between the different meshes. Not only are such interpolations expensive, but until recently no optimal general mathematical framework for doing them existed. Caudillo-Mata et al. (2016) have provided a general mathematical framework for upscaling, which shows impressive improvements compared to traditional upscaling methods. Their approach recognizes the nonuniqueness of the upscaling problem, and rather than employing an analytical expression, they turn the problem into a parameter estimation problem, which can be solved using an optimization technique. This approach allows user input and takes surrounding conductivities into consideration when making upscalings. In their paper the

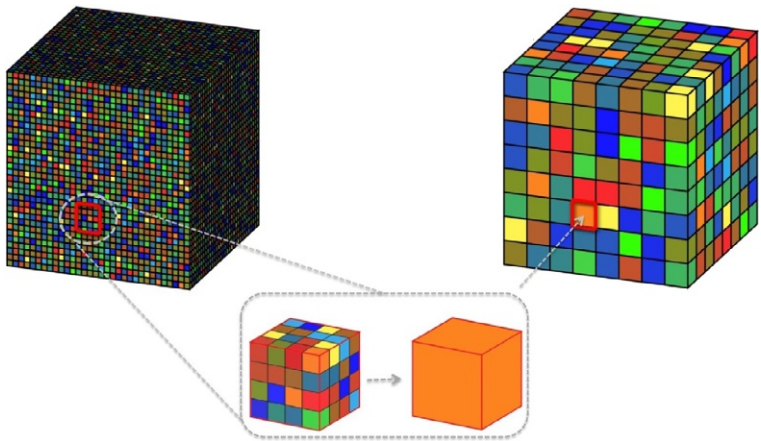

Fig. 8 Upscaling process. *Modified from Caudillo-Mata, L. A., Haber, E., Heagy, L. J., & Schwarzbach, C. (2016). A framework for the upscaling of the electrical conductivity in the quasi-static Maxwell's equations.* Journal of Computational and Applied Mathematics, 317, *388–402 (courtesy of Elsevier).*

method is demonstrated on both 1D and 3D examples. In order to handle the nullspace, one of three different approaches is commonly employed. Haber and Heldmann (2007) use a Helmholtz decomposition of the discrete fields in order avoid the nullspace and stabilize the fields. The second approach explicitly compensates for it using a divergence correction (Hiptmair, 1998). The third approach is to implicitly compensate for it by solving small local systems as done in Mulder (2008).

3.3.3 Depth of Investigation

DOI usually refers to the maximum depth at which data are sufficiently sensitive to the earth properties to affect the data above the noise level. Thus roughly speaking, DOI is an estimate for how deep a model can be trusted.

Several different approaches to estimating DOI exist. Early work on DOI estimation focused on a skin depth approach and effective model resistivities (Spies, 1989). Another approach was suggested by Oldenburg and Li (1999), which involves starting two inversions from different halfspace resistivities. As noted in Christiansen and Auken (2012) both of these approaches have limitations, which make them undesirable. Instead, they suggest a global 1D DOI, based on cumulative sensitivity from the Jacobian. This approach gives a reasonable trade-off between accuracy and time consumption. Fiandaca, Christiansen, and Auken (2015) extend the global 1D DOI approach to multivariate models, in which cross correlation between parameters is considered. This is particularly relevant for induced polarization or higher dimension modeling.

If Monte Carlo methods are employed, then parameter estimation as well as DOI information is usually inherently available, as seen in Fig. 5.

Finally, a paper by Bin, Li-Feng, and Guang-Ding (2014) presents an approach to DOI, which is based on following the position of the maximum electric field value, through a halfspace model. The DOI is then defined as the depth at which this maximum reaches the noise floor. In the paper, the method is not compared to any other DOI method, and the effectiveness of this approach seems questionable.

4. CASE EXAMPLES

We conclude this paper by showing a number of case studies exemplifying the wide area of applicability AEM methods have today.

4.1 Finding Quick Clay

In several parts of the world, quick clay is a serious geohazard. Quick clay is characterized by its very small remolded shear strength (Rankka et al., 2004). Due to this small shear strength, it is prone to cause retrogressive landslides, which have previously caused massive damage. Pfaffhuber, Persson, et al. (2017) showed how AEM can be used to delineate potential quick clay almost as well as ground-based electrical resistivity tomography.

4.2 Delineating Hazardous Material

In Norway black shale causes a serious risk to human health because of its geochemical composition, which includes significant amounts of sulfides and uranium. Furthermore, if exposed to air, the sulfides oxidize, which produce sulfuric acid that poses a hazard to both concrete and metal constructions as well as the environment. In Pfaffhuber, Lysdahl, et al. (2017) AEM resistivity data are linked with geochemical compositions, allowing the black shale to be mapped using AEM.

4.3 Mapping the Fresh–Saltwater Interface

In Holland saltwater intrusion into the coastal aquifers, which supply water to a large percentage of the population, is a crucial issue. Pedersen et al. (2017) demonstrate how AEM mapping can provide unique insight into the water quality of the aquifers. During the survey they were able to distinguish the delicate balance between saltwater and freshwater and track the saltwater intrusion several kilometers into the inland region, as seen in Fig. 9.

4.4 Deep Groundwater Mapping in Antarctica

One clear advantage of AEM methods over any alternative method is their ability to operate in remote, uninhabitable areas. Mikucki et al. (2015) demonstrate how AEM methods have been used to map groundwater and tunnels beneath glaciers in Antarctica as seen in Fig. 10. This mapping suggested a flow between Lake Hare and Lake Fryxell, lakes which were previously thought to be isolated. The ramifications of this are profound for the understanding of the geochemistry of the lakes. In a similar vein, there are several permafrost papers from Alaska (Minsley et al., 2012, 2015; Pastick et al., 2013), which further demonstrate the robustness of the equipment and the applicability of AEM methods for cryospheric mapping.

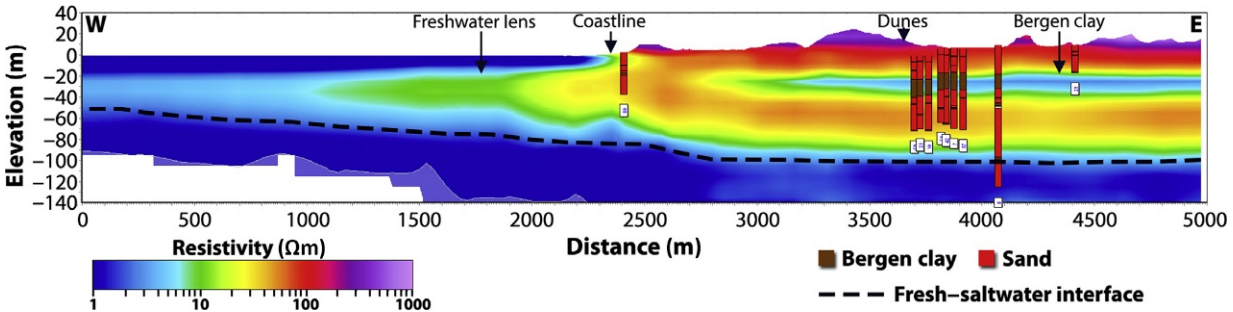

Fig. 9 Salt water intrusion into the mainland, as well as the freshwater lens into the sea. The data show excellent agreement with the drillings in the area. *From Pedersen, J. B., Schaars, F. W., Christiansen, A. V., Foged, N., Schamper, C., Rolf, H., et al. (2017). Mapping the fresh-saltwater interface in the coastal zone using high-resolution airborne electromagnetics.* First Break*, 35, 57–61 (courtesy of* First Break*).*

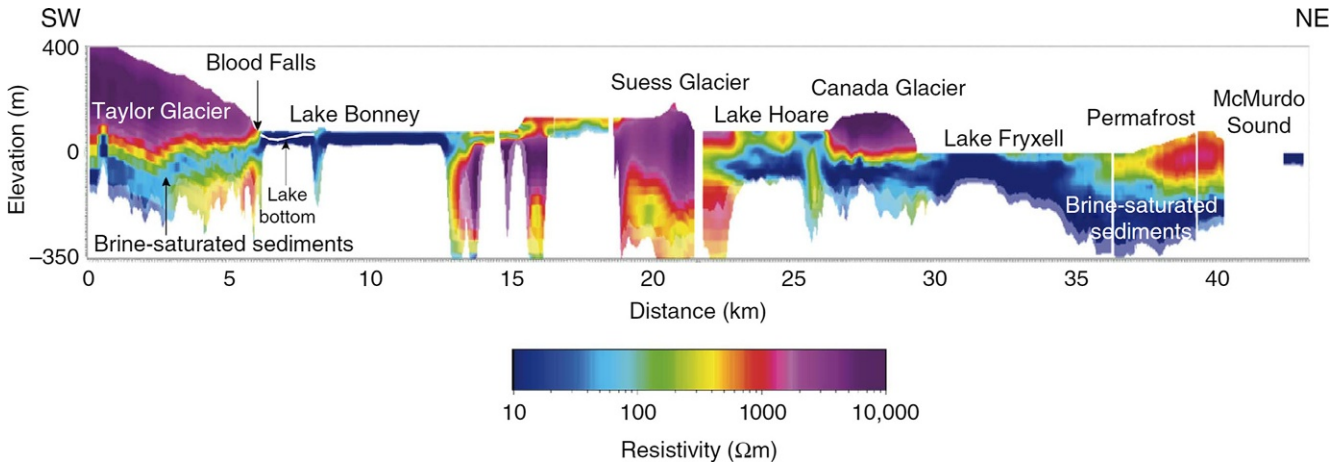

Fig. 10 Resistivity profile along the length of the Taylor Valley. Low resistivities near McMurdo Sound to Lake Hoare is interpreted as hydrological connectivity of brine in sediments extending from the coastal margin inland and beneath the Canada Glacier. *Taken from Mikucki, J. A., Auken, E., Tulaczyk, S., Virginia, R. A., Schamper, C., Sørensen, K. I., et al. (2015). Deep groundwater and potential subsurface habitats beneath an Antarctic dry valley*. Nature Communications, 6 *(licensed under Creative commons).*

4.5 3D Geological Modeling of Complex Buried Valleys

While it is no surprise that AEM can be used in remote, uninhabitable areas, it can also be used successfully in areas with significant infrastructure like Denmark. Høyer, Jørgensen, Sandersen, Viezzoli, and Møller (2015) demonstrate how AEM data can be used to generate 3D models of complex buried valley structures as seen in Fig. 11, when the data are properly processed and the survey system properly accounted for.

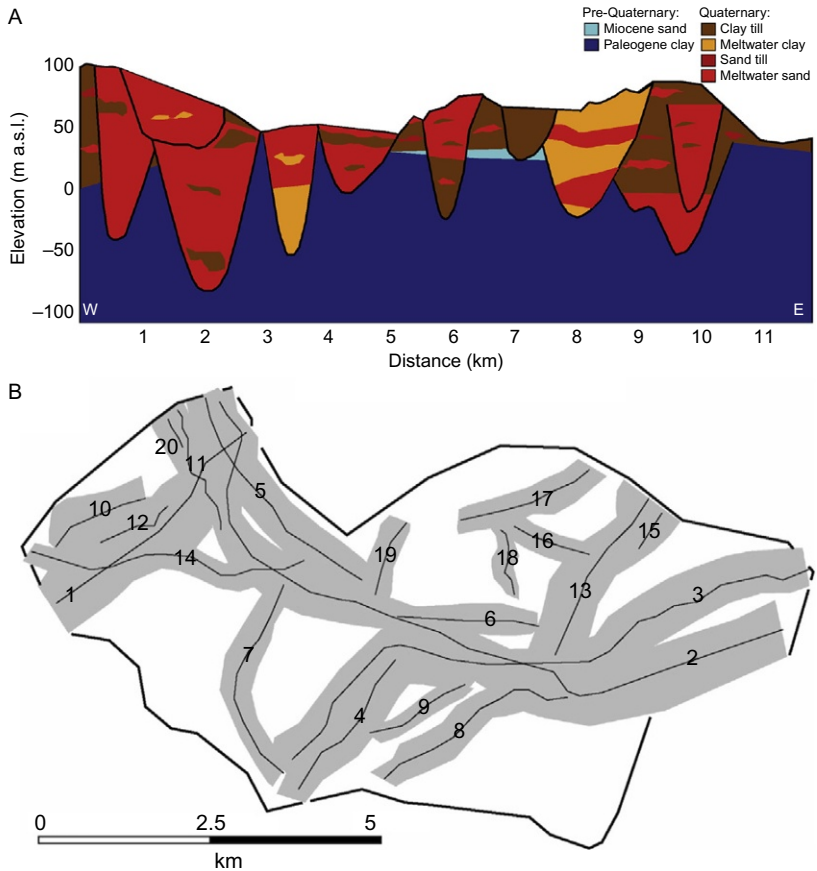

Fig. 11 3D geological mapping of buried valleys. (A) A profile sketch illustrating the conceptual model of the study area. (B) Map of the interpreted buried valleys. The *gray shadings* show the extent of the valleys, whereas the *lines* mark the thalwegs for the individual valleys. Valley numbers are written on the figure. *From Høyer, A. -S., Jørgensen, F., Sandersen, P., Viezzoli, A., & Møller, I. (2015). 3D geological modelling of a complex buried-valley network delineated from borehole and AEM data.* Journal of Applied Geophysics, 122, *94–102 (licensed under Creative commons).*

4.6 Environmental Assessments and Hydrologic Mapping in Africa

A problem with some of the more powerful AEM systems has been that they do not properly remove or compensate for the primary field. While there have been significant improvements during the last decade, Podgorski et al. (2013) demonstrate on a survey from Botswana how even old surveys, with proper and careful processing, can be used for hydrologic mapping. In the paper, they demonstrate how a recalibrated signal goes from a root-mean-square error of 14.67% to 0.51%, as seen in Fig. 12.

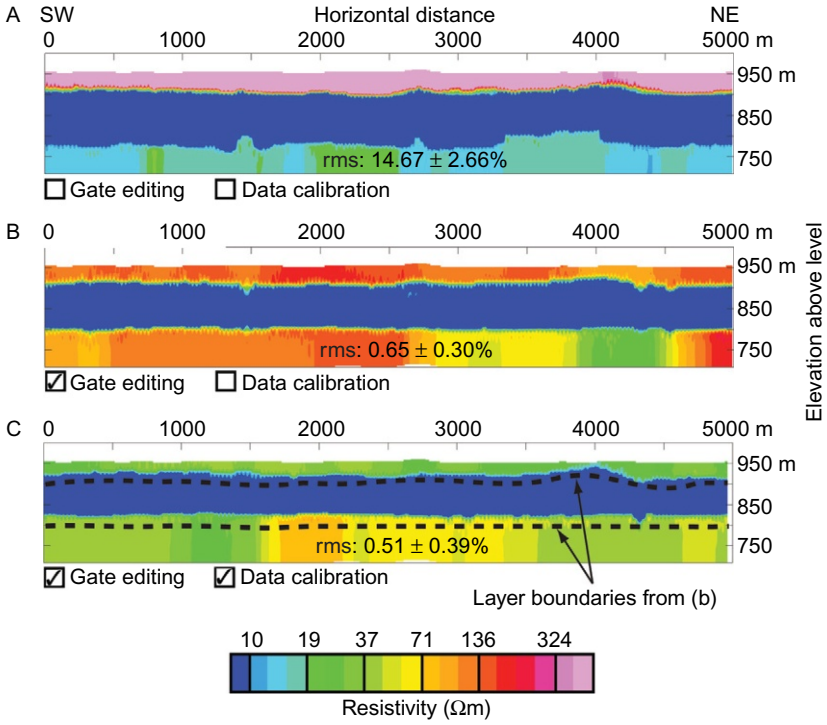

Fig. 12 Inverted resistivity profile models. "Gate editing" refers to the removal of early gates affected by residual transmitter current and the elimination of noisy late gates. "Data calibration" refers to the incorporation of a 30-μs time shift and a 1.44 multiplicative amplitude factor. (A) The resulting model without Gate editing or Data calibration. (B) The resulting model with Gate editing. (C) The resulting model with Gate editing and Data calibration. *From Podgorski, J. E., Auken, E., Schamper, C., Christiansen, A. V., Kalscheuer, T., & Green, A. G. (2013). Processing and inversion of commercial helicopter time-domain electromagnetic data for environmental assessments and geologic and hydrologic mapping.* Geophysics, 78. *https://doi.org/10.1190/geo2012-0452.1*.

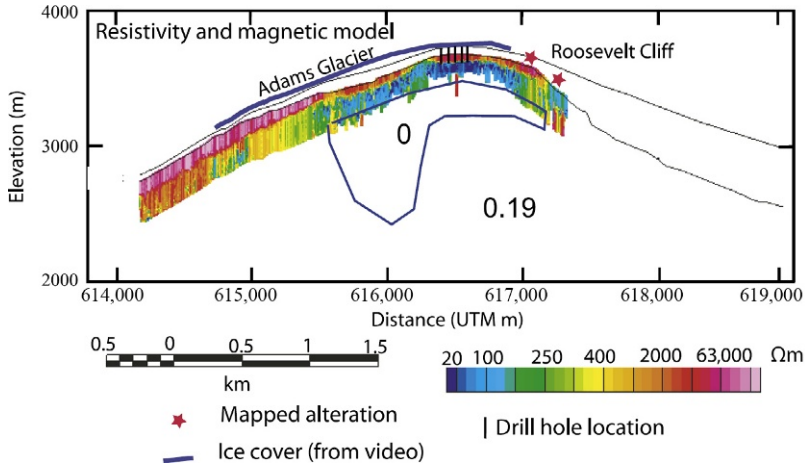

Fig. 13 Resistivity and magnetic models. *Thick blue lines* indicate the extent of glacial ice. The *blue area* indicates a nonmagnetic region ("0" and "0.19" indicate the magnetic susceptibilities in these areas). *Red stars* indicate regions of mapped alteration, *vertical black lines* indicate the location of drill holes, and the *blue outline* (*bottom*) shows distribution of thick (>350 m) nonmagnetic material. *From Finn, C. A., Deszcz-Pan, M., Anderson, E. D., & John, D. A. (2007). Three-dimensional geophysical mapping of rock alteration and water content at Mount Adams, Washington: Implications for lahar hazards.* Journal of Geophysical Research: Solid Earth, 112*, 1–21 (courtesy of Wiley).*

4.7 Measurements of a Collapse-Prone Volcano

The danger from volcanoes is commonly associated with eruptions. However, another less known risk is catastrophic collapses that can lead to massive destructive debris flow. Finn, Deszcz-Pan, Anderson, and John (2007) describe how hydrothermally altered rocks can lead to collapses, especially if they are water saturated. In the paper, they have conducted an AEM survey on Mount Adams, near Salt Creek Lahar, USA. Through the use of both EM data and magnetic data, they are able to find and map the regions that have hydrothermally been altered, as seen in Fig. 13. From this, they predict the most likely places for a future collapse, as well as the scope of a collapse.

5. CONCLUSION AND OUTLOOK

AEM has developed rapidly within the last decade; both survey systems, but also their corresponding interpretive software. As the method develops, more and more applications become viable, as is apparent by the case examples given in this review. These applications require finesse

in order to discriminate some of the low-conductivity contrasts presented, as well as a robust system capable of operating in some of the most hostile climates we have on this planet.

In the last decade HTEM systems have firmly established themselves as the system of choice for most applications. Looking at the latest developments presented by the various companies it is clear that they are becoming increasingly aware of the importance of early-time information and are all investing considerable research in pushing for the earlier time-gate measurements.

Another exciting prospect is that currently advanced 3D EM modeling tools are available and actively developed using online distributed repositories. This enables various academic groups to work on the same software, instead of each group having to develop their own. Furthermore, it makes the software more persistent to the flux of people entering and leaving academia.

The vision in AEM modeling is a code that can directly take the survey data, automatically and objectively process the data, perform an appropriate inversion of the data, and automatically transform the resistivity maps to a geological map. While no code capable of this yet exists, we are starting to see the various building blocks toward reaching that goal. Andersen et al. (2016) demonstrated how neural networks can be used to partly automate the processing, while Friedel et al. (2016) have shown how real-time geological interpretation can be accomplished using machine learning. Ullmann et al. (2016) and Scheunert et al. (2016) have demonstrated a method that automatically selects an appropriate modeling scheme. Thus the building blocks are there, though they will likely need further refinement and then finally to be combined before the vision comes alive. So while there is still a long way to go, it does not seem impossible that such codes could emerge in the coming decade.

REFERENCES

Abraham, J. D., Cannia, J. C., Bedrosian, P. A., Johnson, M. R., Ball, L. B., & Sibray, S. S. (2012). *Airborne electromagnetic mapping of the base of aquifer in areas of western Nebraska*. US Geological Survey.

Abubakar, A., Habashy, T. M., Druskin, V. L., Knizhnerman, L., & Alumbaugh, D. (2008). 2.5 D forward and inverse modeling for interpreting low-frequency electromagnetic measurements. *Geophysics*, *73*, F165–F177.

Allard, M. (2007). On the origin of the HTEM species. *Advances in Airborne Geophysics*, 7, 355–374.

Amestoy, P. R., Duff, I. S., L'Excellent, J.-Y., & Koster, J. (2001). A fully asynchronous multifrontal solver using distributed dynamic scheduling. *SIAM Journal on Matrix Analysis and Applications*, *23*, 15–41.

Andersen, K. K., Kirkegaard, C., Foged, N., Christiansen, A. V., & Auken, E. (2016). Artificial neural networks for removal of couplings in airborne transient electromagnetic data. *Geophysical Prospecting*, *64*, 741–752.

Andersen, K. K., Nyboe, N. S., Kirkegaard, C., Auken, E., & Christiansen, A. V. (2015). In *A system response convolution routine for improved near surface sensitivity in SkyTEM data. First European airborne electromagnetics conference*.

Ansari, S., Farquharson, C., & MacLachlan, S. (2017). A gauged finite-element potential formulation for accurate inductive and galvanic modelling of 3-D electromagnetic problems. *Geophysical Journal International*, *210*, 105–129.

Auken, E., & Christiansen, A. V. (2004). Layered and laterally constrained 2D inversion of resistivity data. *Geophysics*, *69*, 752–761.

Auken, E., Christiansen, A. V., Jacobsen, L. H., & Sørensen, K. I. (2008). A resolution study of buried valleys using laterally constrained inversion of TEM data. *Journal of Applied Geophysics*, *65*, 10–20.

Auken, E., Christiansen, A. V., Kirkegaard, C., Andersen, K., Finadaca, G., Sørensen, K., et al. (2015). In *An overview of the newest SkyTEM and inversion technologies with focus on resolution of shallow geological layers. EAGE/DGG workshop on airborne geophysics 2015*.

Auken, E., Christiansen, A. V., Kirkegaard, C., Fiandaca, G., Schamper, C., Behroozmand, A. A., et al. (2014). An overview of a highly versatile forward and stable inverse algorithm for airborne, ground-based and borehole electromagnetic and electric data. *Exploration Geophysics*, *46*, 223–235.

Balch, S., Boyko, W., & Paterson, N. (2003). The AeroTEM airborne electromagnetic system. *The Leading Edge*, *22*, 562–566.

Bedrosian, P. A., Schamper, C., & Auken, E. (2016). A comparison of helicopter-borne electromagnetic systems for hydrogeologic studies. *Geophysical Prospecting*, *64*, 192–215.

Bezanson, J., Karpinski, S., Shah, V. B., & Edelman, A. (2012). *Julia: A fast dynamic language for technical computing*. arXiv preprint arXiv:1209.5145.

Bin, C., Li-Feng, M., & Guang-Ding, L. (2014). Estimating penetration depth of the CHTEM-I system by the diffusive electric field method. *Chinese Journal of Geophysics*, *57*, 112–119.

Boesen, T., Auken, E., Christiansen, A. V., Fiandaca, G., Kirkegaard, C., Pfaffhuber, A., et al. (2017). An efficient 2D inversion scheme for airborne frequency domain data. *Geophysics*.

Börner, R.-U. (2010). Numerical modelling in geo-electromagnetics: Advances and challenges. *Surveys in Geophysics*, *31*, 225–245.

Börner, R.-U., Ernst, O. G., & Güttel, S. (2015). Three-dimensional transient electromagnetic modelling using Rational Krylov methods. *Geophysical Journal International*, *202*, 2025–2043.

Börner, R.-U., Ernst, O. G., & Spitzer, K. (2008). Fast 3-D simulation of transient electromagnetic fields by model reduction in the frequency domain using Krylov subspace projection. *Geophysical Journal International*, *173*, 766–780.

Bournas, N., Taylor, S., Prikhodko, A., Plastow, G., Kwan, K., Legault, J., et al. (2017). Superparamagnetic effects discrimination in VTEM data of Greenland using multiple criteria and predictive approaches. *Journal of Applied Geophysics*, *145*, 59–73.

Brodie, R. (2012). Appendix 3: GA-LEI inversion of TEMPEST data. In I. C. Roach (Ed.), *The Frome airborne electromagnetic survey, South Australia: Implications for energy, minerals and regional geology: Geoscience Australia Record* (pp. 278–287). Geoscience Australia.

Brodie, R. C., & Richardson, M. (2013). AEM system target resolvability analysis using a Monte Carlo inversion algorithm. In *ASEG extended abstracts 2013* (pp. 1–4). Australian Society of Exploration Geophysicists (ASEG).

Brodie, R., & Sambridge, M. (2006). A holistic approach to inversion of frequency-domain airborne EM data. *Geophysics*, *71*, G301–G312.

Brodie, R., & Sambridge, M. (2009a). An example of holistic inversion of time domain AEM data. In *ASEG extended abstracts 2009* (pp. 1–9).
Brodie, R., & Sambridge, M. (2009b). Holistic inversion of frequency-domain airborne electromagnetic data with minimal prior information. *Exploration Geophysics*, *40*, 8–16.
Brodie, R. C., & Sambridge, M. (2012). Transdimensional Monte Carlo inversion of AEM data. In *ASEG extended abstracts 2012* (pp. 1–4).
Cai, H., Hu, X., Xiong, B., Auken, E., Han, M., & Li, J. (2017). Finite element time domain modeling of controlled-source electromagnetic data with a hybrid boundary condition. *Journal of Applied Geophysics*, *145*, 133–143.
Caudillo-Mata, L. A., Haber, E., Heagy, L. J., & Schwarzbach, C. (2016). A framework for the upscaling of the electrical conductivity in the quasi-static Maxwell's equations. *Journal of Computational and Applied Mathematics*, *317*, 388–402.
Chang-Chun, Y., Xiu-Yan, R., Yun-He, L., Yan-Fu, Q., Chang-Kai, Q., & Jing, C. (2015). Review on airborne electromagnetic inverse theory and applications. *Geophysics*, *80*, W17–W31.
Chen, T., Hodges, G., & Miles, P. (2014). MULTIPULSE—High resolution and high power in one TDEM system. *Exploration Geophysics*, *46*, 49–57.
Chikazumi, S., & Graham, C. D. (2009). *Physics of ferromagnetism 2e*. Oxford University Press on Demand. ISBN: 0199564817.
Christensen, N. B. (2016a). Fast approximate 1D modelling and inversion of transient electromagnetic data. *Geophysical Prospecting*, *64*, 1620–1631.
Christensen, N. B. (2016b). Strictly horizontal lateral parameter correlation for 1D inverse modelling of large datasets. *Near Surface Geophysics*, *14*, 403–411.
Christensen, N. K., Ferre, T. P. A., Fiandaca, G., & Christensen, S. (2017). Voxel inversion of airborne electromagnetic data for improved groundwater model construction and prediction accuracy. *Hydrology and Earth System Sciences*, *21*, 1321.
Christensen, N. B., Reid, J. E., & Halkjær, M. (2009). Fast, laterally smooth inversion of airborne time-domain electromagnetic data. *Near Surface Geophysics*, *7*, 599–612.
Christensen, N. B., & Tølbøll, R. J. (2009). A lateral model parameter correlation procedure for one-dimensional inverse modelling. *Geophysical Prospecting*, *57*, 919–929.
Christiansen, A. V., & Auken, E. (2012). A global measure for depth of investigation. *Geophysics*, *77*, WB171–WB177.
Christiansen, A. V., Auken, E., Kirkegaard, C., Schamper, C., & Vignoli, G. (2016). An efficient hybrid scheme for fast and accurate inversion of airborne transient electromagnetic data. *Exploration Geophysics*, *47*, 323–330.
Christiansen, A. V., Auken, E., Ley-Cooper, A. Y., & Andersen, K. R. (2016). In *Quantifying the effect of primary field modelling on TEMPEST data—The importance of uncertainty ASEG extended abstracts 2016: 25th international geophysical conference and exhibition* (pp. 719–723).
Christiansen, A. V., Auken, E., & Viezzoli, A. (2011). Quantification of modeling errors in airborne TEM caused by inaccurate system description. *Geophysics*, *76*, F43–F52.
Cockett, R., Kang, S., Heagy, L. J., Pidlisecky, A., & Oldenburg, D. W. (2015). SimPEG: An open source framework for simulation and gradient based parameter estimation in geophysical applications. *Computers & Geosciences*, *85*, 142–154.
Combrinck, M., & Wright, R. (2016). *XciteTM: Great results require more than good data*.
Constable, S. C., Parker, R. L., & Constable, C. G. (1987). Occam's inversion: A practical algorithm for generating smooth models from electromagnetic sounding data. *Geophysics*, *52*, 289–300.
Cox, L. H., Wilson, G. A., & Zhdanov, M. S. (2010). 3D inversion of airborne electromagnetic data using a moving footprint. *Exploration Geophysics*, *41*, 250–259.
Cox, L. H., Wilson, G. A., & Zhdanov, M. S. (2012). 3D inversion of airborne electromagnetic data. *Geophysics*, *77*, WB59–WB69.

Cuthill, E., & McKee, J. (1969). In *Reducing the bandwidth of sparse symmetric matrices Proceedings of the 1969 24th national conference* (pp. 157–172).

Eadie, T., Legault, J., Plastow, G., Prikhodko, A., & Tishin, P. (2017). In *An improved helicopter time-domain EM system for near surface applications. Second European airborne electromagnetics conference.*

Effersø, F., Auken, E., & Sørensen, K. I. (1999). Inversion of band-limited TEM responses. *Geophysical Prospecting*, *47*, 551–564.

Everett, M. E. (2012). Theoretical developments in electromagnetic induction geophysics with selected applications in the near surface. *Surveys in Geophysics*, *33*, 29–63.

Farquharson, C. G., & Oldenburg, D. W. (1998). Non-linear inversion using general measures of data misfit and model structure. *Geophysical Journal International*, *134*, 213–227.

Fiandaca, G., Christiansen, A. V., & Auken, E. (2015). In *Depth of investigation for multi-parameters inversions. Near surface geoscience 2015—21st European meeting of environmental and engineering geophysics.*

Finn, C. A., Deszcz-Pan, M., Anderson, E. D., & John, D. A. (2007). Three-dimensional geophysical mapping of rock alteration and water content at Mount Adams, Washington: Implications for lahar hazards. *Journal of Geophysical Research: Solid Earth*, *112*, 1–21.

Friedel, M. J., Esfahani, A., & Iwashita, F. (2016). Toward real-time three-dimensional mapping of surficial aquifers using a hybrid modeling approach. *Hydrogeology Journal*, *24*, 211–229.

Gisselø, P., & Nyboe, N. (2017). In *SkyTEM high power systems—A new generation of airborne TEM transmitters. Second European airborne electromagnetics conference.*

Gould, N. I. M., Scott, J. A., & Hu, Y. (2007). A numerical evaluation of sparse direct solvers for the solution of large sparse symmetric linear systems of equations. *ACM Transactions on Mathematical Software*, *33*, 10.

Guillemoteau, J., Sailhac, P., & Béhaegel, M. (2011). Regularization strategy for the layered inversion of airborne transient electromagnetic data: Application to in-loop data acquired over the basin of Franceville (Gabon). *Geophysical Prospecting*, *59*, 1132–1143.

Haber, E. (2004). Quasi-Newton methods for large-scale electromagnetic inverse problems. *Inverse Problems*, *21*, 305–323.

Haber, E., Ascher, U. M., & Oldenburg, D. W. (2004). Inversion of 3D electromagnetic data in frequency and time domain using an inexact all-at-once approach. *Geophysics*, *69*, 1216–1228.

Haber, E., & Heldmann, S. (2007). An octree multigrid method for quasi-static Maxwell's equations with highly discontinuous coefficients. *Journal of Computational Physics*, *223*, 783–796.

Haber, E., Oldenburg, D. W., & Shekhtman, R. (2007). Inversion of time domain three-dimensional electromagnetic data. *Geophysical Journal International*, *171*, 550–564.

Haber, E., & Schwarzbach, C. (2014). Parallel inversion of large-scale airborne time-domain electromagnetic data with multiple OcTree meshes. *Inverse Problems*, *30*, 1–28.

Heagy, L. J., Cockett, R., Kang, S., Rosenkjaer, G. K., & Oldenburg, D. W. (2016). *A framework for simulation and inversion in electromagnetics*. arXiv preprint arXiv:1610.00804.

Hestenes, M. R., & Stiefel, E. (1952). Methods of conjugate gradients for solving linear systems. *Journal of Research of the National Bureau of Standards*, *49*.

Hine, K., & Macnae, J. (2016). Comparing induced polarization responses from airborne inductive and galvanic ground systems: Lewis Ponds, New South Wales. *Geophysics*, *81*, B179–B188.

Hiptmair, R. (1998). Multigrid method for Maxwell's equations. *SIAM Journal on Numerical Analysis*, *36*, 204–225.

Høyer, A.-S., Jørgensen, F., Sandersen, P., Viezzoli, A., & Møller, I. (2015). 3D geological modelling of a complex buried-valley network delineated from borehole and AEM data. *Journal of Applied Geophysics*, *122*, 94–102.

Hunkeler, P. A., Hendricks, S., Hoppmann, M., Farquharson, C. G., Kalscheuer, T., Grab, M., et al. (2015). Improved 1D inversions for sea ice thickness and conductivity from electromagnetic induction data: Inclusion of nonlinearities caused by passive bucking. *Geophysics*, *81*, WA45–WA58.

Kaminski, V., & Viezzoli, A. (2017). Modeling induced polarization effects in helicopter time-domain electromagnetic data: Field case studies. *Geophysics*, *82*, B49–B61.

Kang, S., & Oldenburg, D. W. (2015). Recovering IP information in airborne-time domain electromagnetic data. In *ASEG extended abstracts 2015* (pp. 1–4).

Kang, S., & Oldenburg, D. W. (2016). On recovering distributed IP information from inductive source time domain electromagnetic data. *Geophysical Journal International*, *207*, 174–196.

Killeen, P. G. (2013). *Exploration trends and developments in 2012*. The Northern Miner.

Killeen, P. G. (2014). *Exploration trends and developments in 2013*. The Northern Miner.

Kirkegaard, C., Andersen, K., Boesen, T., Christiansen, A. V., Auken, E., & Fiandaca, G. (2015). Utilizing massively parallel co-processors in the AarhusInv 1D forward and inverse AEM modelling code. In *ASEG extended abstracts 2015* (pp. 1–3).

Kirkegaard, C., Andersen, K., Christiansen, A. V., Auken, E., & Boesen, T. (2015). In *Rapid inversion of large airborne AEM data datasets utilizing massively parallel co-processors*. *First European airborne electromagnetics conference*.

Kirkegaard, C., & Auken, E. (2015). A parallel, scalable and memory efficient inversion code for very large-scale airborne electromagnetics surveys. *Geophysical Prospecting*, *63*, 495–507.

Kratzer T., Late-time effects in airborne EM: Induced polarisation, superparamagnetism and rotation, PhD thesis, Royal Melbourne Institute of Technology (RMIT) University, 2013.

Kratzer, T., Macnae, J., & Mutton, P. (2013). Detection and correction of SPM effects in airborne EM surveys. *Exploration Geophysics*, *44*, 6–15.

Lane, R., Green, A., Golding, C., Owers, M., Pik, P., Plunkett, C., et al. (2000). An example of 3D conductivity mapping using the TEMPEST airborne electromagnetic system. *Exploration Geophysics*, *31*, 162–172.

Legault, J. M. (2015). Airborne electromagnetic systems—State of the art and future directions. *CSEG Recorder*, *40*, 38–49.

Legault, J. M., Prikhodko, A., Dodds, D., Macnae, J. C., & Oldenborger, G. A. (2012). In *Results of recent VTEM helicopter system development testing over the Spiritwood Valley aquifer, Manitoba 25th symposium on the application of geophysics to engineering & environmental problems*.

Lelièvre, P. G., Oldenburg, D. W., & Williams, N. C. (2009). Integrating geological and geophysical data through advanced constrained inversions. *Exploration Geophysics*, *40*, 334–341.

Lewis, A. S., & Overton, M. L. (2013). Nonsmooth optimization via quasi-Newton methods. *Mathematical Programming*, *141*, 135–163.

Ley-Cooper, A. Y., Macnae, J., & Viezzoli, A. (2010). Breaks in lithology: Interpretation problems when handling 2D structures with a 1D approximation. *Geophysics*, *75*, WA179–WA188.

Ley-Cooper, A. Y., Viezzoli, A., Guillemoteau, J., Vignoli, G., Macnae, J., Cox, L., et al. (2014). Airborne electromagnetic modelling options and their consequences in target definition. *Exploration Geophysics*, *46*, 74–84.

Li, W.-B., Zeng, Z.-F., Li, J., Chen, X., Wang, K., & Xia, Z. (2016). 2.5 D forward modeling and inversion of frequency-domain airborne electromagnetic data. *Applied Geophysics*, *13*, 37–47.

Macnae, J. (2016a). Fitting superparamagnetic and distributed Cole-Cole parameters to airborne electromagnetic data: A case history from Quebec. *Geophysics*, *81*, B211–B220.

Macnae, J. (2016b). Quantitative estimation of intrinsic induced polarization and super-paramagnetic parameters from airborne electromagnetic data. *Geophysics*, *81*, E433–E446.

Macnae, J., King, A., Stolz, N., Osmakoff, A., & Blaha, A. (1998). Fast AEM data processing and inversion. *Exploration Geophysics*, *29*, 163–169.

Marchant, D. (2015). *Induced polarization effects in inductive source electromagnetic data*. University of British Columbia.

Marchant, D., Haber, E., & Oldenburg, D. W. (2012). Inductive source induced polarization. *Geophysical Journal International*, *192*, 602–612.

Marchant, D., Haber, E., & Oldenburg, D. W. (2014). Three-dimensional modeling of IP effects in time-domain electromagnetic data. *Geophysics*, *79*, E303–E314.

Menke, W. (1989). *Geophysical data analysis: Discrete inverse theory*. Academic Press. ISBN: 0124909213 (alk. paper).

Mikucki, J. A., Auken, E., Tulaczyk, S., Virginia, R. A., Schamper, C., Sørensen, K. I., et al. (2015). Deep groundwater and potential subsurface habitats beneath an Antarctic dry valley. *Nature Communications*, *6*, 1–9.

Minsley, B. J. (2011). A trans-dimensional Bayesian Markov chain Monte Carlo algorithm for model assessment using frequency-domain electromagnetic data. *Geophysical Journal International*, *187*, 252–272.

Minsley, B. J., Abraham, J. D., Smith, B. D., Cannia, J. C., Voss, C. I., Jorgenson, M. T., et al. (2012). Airborne electromagnetic imaging of discontinuous permafrost. *Geophysical Research Letters*, *39*, 1–8.

Minsley, B. J., Kass, M. A., Hodges, G., & Smith, B. D. (2014). Multielevation calibration of frequency-domain electromagnetic data. *Geophysics*, *79*, E201–E216. https://doi.org/10.1190/geo2013-0320.1.

Minsley, B. J., Wellman, T. P., Walvoord, M. A., & Revil, A. (2015). Sensitivity of airborne geophysical data to sublacustrine and near-surface permafrost thaw. *The Cryosphere*, *9*, 781–794.

Mulder, W. A. (2008). Geophysical modelling of 3D electromagnetic diffusion with multigrid. *Computing and Visualization in Science*, *11*, 129–138.

Mulè, S., Miller, R., Carey, H., & Lockwood, R. (2012). Review of three airborne EM systems. In *ASEG extended abstracts 2012* (pp. 1–5).

Nash, S. G., & Nocedal, J. (1991). A numerical study of the limited memory BFGS method and the truncated-Newton method for large scale optimization. *SIAM Journal on Optimization*, *1*, 358–372.

Nyboe, N., & Mai, S. (2017). In *Recent advances in SkyTEM receiver system technologies Second European airborne electromagnetics conference*.

Nyboe, N. S., & Sørensen, K. (2012). Noise reduction in TEM: Presenting a bandwidth-and sensitivity-optimized parallel recording setup and methods for adaptive synchronous detection. *Geophysics*, *77*, E203–E212.

Oldenburg, D. W., Haber, E., & Shekhtman, R. (2012). Three dimensional inversion of multisource time domain electromagnetic data. *Geophysics*, *78*, E47–E57.

Oldenburg, D. W., & Li, Y. (1999). Estimating depth of investigation in DC resistivity and IP surveys. *Geophysics*, *64*, 403–416.

Oldenburg, D. W., & Li, Y. (2005). Inversion for applied geophysics: A tutorial. Near-surface geophysics: SEG, pp. 89–150.

Pastick, N. J., Jorgenson, M. T., Wylie, B. K., Minsley, B. J., Ji, L., Walvoord, M. A., et al. (2013). Extending airborne electromagnetic surveys for regional active layer and permafrost mapping with remote sensing and ancillary data, Yukon Flats Ecoregion, Central Alaska. *Permafrost and Periglacial Processes*, *24*, 184–199.

Pedersen, J. B., Schaars, F. W., Christiansen, A. V., Foged, N., Schamper, C., Rolf, H., et al. (2017). Mapping the fresh-saltwater interface in the coastal zone using high-resolution airborne electromagnetics. *First Break*, *35*, 57–61.

Pfaffhuber, A. A., Lysdahl, A. O., Sørmo, E., Skurdal, G. H., Thomassen, T., Anschütz, H., et al. (2017). Delineating hazardous material without touching—AEM mapping of Norwegian alum shale. *First Break*, *35*, 35–39.

Pfaffhuber, A. A., Persson, L., Lysdahl, A. O., Kåsin, K., Anschütz, H., Bastani, M., et al. (2017). Integrated scanning for quick clay with AEM and ground-based investigations. *First Break*, *35*, 73–79.

Podgorski, J. E., Auken, E., Schamper, C., Christiansen, A. V., Kalscheuer, T., & Green, A. G. (2013). Processing and inversion of commercial helicopter time-domain electromagnetic data for environmental assessments and geologic and hydrologic mapping. *Geophysics*, *78*, E149–E159. https://doi.org/10.1190/geo2012-0452.1.

Press, W. H., Teukolsky, S. A., Vetterling, W. T., & Flannery, B. P. (1992). *Numerical recipes in Fortran 77: The art of scientific computing*. Cambridge University Press.

Prikhodko, A., Legault, J. M., Kwan, K., Eadie, T., Oldenborger, G. A., Sapia, V., et al. (2013). In *Recent AEM case study examples using a full waveform time-domain system for near-surface applications* (pp. 377–386). *Symposium on the application of geophysics to engineering and environmental problems 2013*.

Puzyrev, V., Koric, S., & Wilkin, S. (2016). Evaluation of parallel direct sparse linear solvers in electromagnetic geophysical problems. *Computers & Geosciences*, *89*, 79–87.

Rankka, K., Andersson-Sköld, Y., Hultén, C., Larsson, R., Leroux, V., & Dahlin, T. (2004). *Quick clay in Sweden*. Swedish Geotechnical Institute report 65 (p. 145).

Rasmussen, S., Nyboe, N. S., Mai, S., & Larsen, J. J. (2017). Noise properties of Fourier deconvolution for time-domain EM soundings. *Geophysics*, *82*, 1–39.

Reninger, P.-A., Martelet, G., Deparis, J., Perrin, J., & Chen, Y. (2011). Singular value decomposition as a denoising tool for airborne time domain electromagnetic data. *Journal of Applied Geophysics*, *75*, 264–276.

Ruthotto, L., Treister, E., & Haber, E. (2016). *jInv—A flexible Julia package for PDE parameter estimation*. arXiv preprint arXiv:1606.07399.

Saad, Y. (2003). *Iterative methods for sparse linear systems*. Siam. ISBN: 0898715342.

Sattel, D., & Battig, E. (2016). Reprocessing streaming MEGATEM data for square-wave EM, VLF, and AFMAG responses. In *SEG technical program expanded abstracts 2016* (pp. 2144–2148). Society of Exploration Geophysicists. ISBN 1949-4645.

Sattel, D., & Mutton, P. (2014). Modelling the superparamagnetic response of AEM data. *Exploration Geophysics*, *46*, 118–129.

Schamper, C., Auken, E., & Sørensen, K. (2014). Coil response inversion for very early time modelling of helicopter-borne time-domain electromagnetic data and mapping of near-surface geological layers. *Geophysical Prospecting*, *62*, 658–674.

Schenk, O., Gärtner, K., & Fichtner, W. (2000). Efficient sparse LU factorization with left-right looking strategy on shared memory multiprocessors. *BIT Numerical Mathematics*, *40*, 158–176.

Scheunert, M., Ullmann, A., Afanasjew, M., Börner, R.-U., Siemon, B., & Spitzer, K. (2016). A cut-&-paste strategy for the 3-D inversion of helicopter-borne electromagnetic data-I. 3-D inversion using the explicit Jacobian and a tensor-based formulation. *Journal of Applied Geophysics*, *129*, 209–221.

Siemon, B., Auken, E., & Christiansen, A. V. (2009). Laterally constrained inversion of helicopter-borne frequency-domain electromagnetic data. *Journal of Applied Geophysics*, *67*, 259–268.

Smiarowski, A., & Macnae, J. (2013). Detection of a perfect conductor with an airborne electromagnetic system: The Gemini Field Test. *Geophysics*, *78*, E249–E259.

Smith, R. (2014). Electromagnetic induction methods in mining geophysics from 2008 to 2012. *Surveys in Geophysics*, *35*, 123–156.

Smith, R. S., & Klein, J. (1996). A special circumstance of airborne induced-polarization measurements. *Geophysics*, *61*, 66–73.

Sørensen, K. I., & Auken, E. (2004). SkyTEM—A new high-resolution helicopter transient electromagnetic system. *Exploration Geophysics*, *35*, 194–202.

Spies, B. R. (1989). Depth of investigation in electromagnetic sounding methods. *Geophysics*, *54*, 872–888.

Steuer, A., Siemon, B., & Auken, E. (2009). A comparison of helicopter-borne electromagnetics in frequency-and time-domain at the Cuxhaven valley in Northern Germany. *Journal of Applied Geophysics*, *67*, 194–205.

Stoyer, C. H., & Greenfield, R. J. (1976). Numerical solutions of the response of a two-dimensional earth to an oscillating magnetic dipole source. *Geophysics*, *41*, 519–530.

Ullmann, A., Scheunert, M., Afanasjew, M., Börner, R.-U., Siemon, B., & Spitzer, K. (2016). A cut-&-paste strategy for the 3-D inversion of helicopter-borne electromagnetic data-II. Combining regional 1-D and local 3-D inversion. *Journal of Applied Geophysics*, *130*, 131–144.

Van der Vorst, H. A. (1992). Bi-CGSTAB: A fast and smoothly converging variant of Bi-CG for the solution of nonsymmetric linear systems. *SIAM Journal on Scientific and Statistical Computing*, *13*, 631–644.

Viezzoli, A., Christiansen, A. V., Auken, E., & Sørensen, K. (2008). Quasi-3D modeling of airborne TEM data by spatially constrained inversion. *Geophysics*, *73*, F105–F113. https://doi.org/10.1190/1.2895521.

Viezzoli, A., Kaminskiy, V., & Fiandaca, G. (2017). Modeling induced polarization effects in helicopter time domain electromagnetic data: Synthetic case studies. *Geophysics*, *82*, E31–E50.

Viezzoli, A., Munday, T., Auken, E., & Christiansen, A. V. (2010). Accurate quasi 3D versus practical full 3D inversion of AEM data—The Bookpurnong case study. *Preview*, *149*, 23–31.

Vignoli, G., Fiandaca, G., Christiansen, A. V., Kirkegaard, C., & Auken, E. (2015). Sharp spatially constrained inversion with applications to transient electromagnetic data. *Geophysical Prospecting*, *63*, 243–255.

Vöge, M., Pfaffhuber, A., Auken, E., Kirkegaard, C., Boesen, T., Hendricks, S., et al. (2015). In *2.5 D inversion of sea ice thickness from helicopter EM data First European airborne electromagnetics conference*.

Ward, S. H., & Hohmann, G. W. (1988). Electromagnetic theory for geophysical applications. *Electromagnetic Methods in Applied Geophysics*, *1*, 131–311.

Weidelt, P. (1982). Response characteristics of coincident loop transient electromagnetic systems. *Geophysics*, *47*, 1325–1330.

Wilson, G. A., Cox, L. H., Čuma, M., & Zhdanov, M. S. (2012). Inverting airborne geophysical data for mega-cell and giga-cell 3D Earth models. *The Leading Edge*, *31*, 316–321.

Yang, D., & Oldenburg, D. W. (2012a). Practical 3D inversion of large airborne time domain electromagnetic data sets. In *ASEG extended abstracts 2012* (pp. 1–4). .

Yang, D., & Oldenburg, D. W. (2012b). Three-dimensional inversion of airborne time-domain electromagnetic data with applications to a porphyry deposit. *Geophysics*, *77*, B23–B34.

Yang, D., Oldenburg, D. W., & Haber, E. (2014). 3-D inversion of airborne electromagnetic data parallelized and accelerated by local mesh and adaptive soundings. *Geophysical Journal International*, *196*, 1492–1507.

Yin, C., & Hodges, G. (2007). Simulated annealing for airborne EM inversion. *Geophysics*, *72*, F189–F195. https://doi.org/10.1190/1.2736195.

Yin, C., Qi, Y., & Liu, Y. (2016). 3D time-domain airborne EM modeling for an arbitrarily anisotropic earth. *Journal of Applied Geophysics*, *131*, 163–178.

Yu, W. W., & Haber, E. (2012). A 2.5 D inversion of airborne electromagnetic data. In *SEG technical program expanded abstracts 2012* (pp. 1–5): Society of Exploration Geophysicists.

This page intentionally left blank

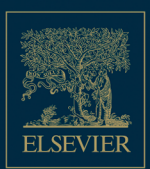

ACADEMIC PRESS

An imprint of Elsevier
elsevier.com/books-and-journals